

©2019

MENGJUN LI

ALL RIGHTS RESERVED

NOVEL MATERIALS AND METHODS FOR NANOLITHOGRAPHY: EXTENDING

MOORE'S LAW

By

MENGJUN LI

A dissertation submitted to the

School of Graduate Studies

Rutgers, The State University of New Jersey

In partial fulfillment of the requirements

For the degree of

Doctor of Philosophy

Graduate Program in Chemistry

Written under the direction of

Eric L. Garfunkel

And approved by

New Brunswick, New Jersey

OCTOBER, 2019

ABSTRACT OF THE DISSERTATION

NOVEL MATERIALS AND METHODS FOR NANOLITHOGRAPHY: EXTENDING

MOORE'S LAW

by MENGJUN LI

Dissertation Director

Prof. Eric L. Garfunkel

We are at a stage in the development of the semiconductor electronics industry that a technical and material renovation must occur if we wish to continue our steady exponential improvement in computational power (in a sense keeping up with Moore's law). Lithography is the key methods that allows us to continuously scale the physical dimensions of electrical devices. For high volume manufacturing, the lithographically printed feature is limited by incident photon wavelength. The key tool to obtain small features than can be obtained by optical (UV) lithography is call multiple patterning. However, to achieve sub-10 nm features, the high cost and high failure rate of multiple patterning (using 193 nm photons) is driving the industry to switch to extreme ultraviolet (EUV) photons with 13.5 nm (92eV).

EUV lithography requires the development of appropriate photoresists. Although they are well developed over the past several decades, organic resists have several limitations, and inorganic resists are outperforming them in many development labs. Inorganic metal-containing resists demonstrate high resolution and sensitivity in EUV lithography.

In this thesis, we first review basic concepts in EUV lithography and our work which focuses on inorganic resist development and the radiation chemistry associated with the lithographic process. We next (chapter 2) review the experimental methods used to prepare and characterize resists and simple device structures. In chapter 3 we discuss three tin-based EUV resist candidates. By exploring the film uniformity and composition, we chose a model resist that can provide an appropriate thin film with low contamination. The radiation chemistry was then investigated through various *in-situ* characterization methods. Instead of using a \$100M commercial EUV lithography tool (ASML), we used an assortment of photon, electron and ion proxies (substitutes) to mimic the initial excitation of the resist. High energy x-ray (1486.6 eV) exposure, was used to initiate and then characterize the chemical composition changes, while low energy ultraviolet exposure (21.2, 40.8 eV photons) was also used as an EUV substitute and give additional information about resist changes that occur during and after exposure. Ambient pressure synchrotron x-ray exposure (SSRL) helped further understand the chemically active species that might exist under the irradiation. Eventually two possible reaction pathways were proposed to explain the chemical behavior of this class of novel resists under photon exposure.

We took advantage of the atomically focused helium ion beam in our helium ion microscope (less than 0.5 nm spot size) to investigate the patterning performance and properties of our model resist. The ion exposure shares some key aspects in radiation chemistry with photon exposure as we believe that the key chemistry involves secondary electrons (generated from any number of primary excitation sources) to trigger the chemical reaction inside photoresist films. The three main patterning performance metrics, sensitivity, resolution and LER (line edge roughness), as well as the etching selectivity, were examined which demonstrated that our model resist to be a good candidate for EUVL. We further modified the interface bonding and changed substrates to understand the effects of interface and substrate on lithographic processing behavior and ultimate resolution. Weaker interface bonding (between resist and substrate) resulted in improvements in the development step, and substrates that would generate a higher secondary electron yield upon exposure can provide additional “back exposure” to improve the effective sensitivity of the resist.

The physical scaling of current devices will soon reach their atomic scale limits. Novel device materials and structures will replace the current MOSFET structure (which dominates most modern computer processors and memory) and new computing paradigms such as neuromorphic or quantum computing will be required to move beyond ultimately scaled CMOS devices. Device technology breakthroughs using charge, spin or in the longer-term alternative state/hybrid state variables in superconducting qubits, are becoming popular topics that need much more research and development (> 10 years) effort before they can

replace current highly scaled CMOS. For some specific applications such as voltage standards and SQUID devices, Josephson junction tunneling devices are already being employed. Focused helium ion beams can directly write nanometer scale structures without chemically reacting with the targets themselves. Instead of using a “conventional” three-layer Josephson junction structure, we fabricated planar Josephson junctions using a focused helium ion beam. The resulting structure successfully demonstrated effective operation with high critical temperature superconducting materials. Ion damage events were simulated to understand the relation between the junction creation and helium ion doses. Large array junctions with good uniformity were also fabricated for the first time and showed good consistency between the normal resistance of the array scaled and the number of junctions in the array. The results were significantly better than those produced by other nanofabrication techniques.

In summary, we demonstrated the use of a systematic set of EUV resist exposure and characterization tools to prescreen EUV resist candidates. We believe that our model of study, and our results, increase our understanding of the radiation chemistry and patterning performance of resists, and can help in the development of better resists going forward. We proved that using a focused helium ion beam as a direct writing is an appropriate alternative method for research-level studies of resist materials as well as a novel nanofabrication technique for Josephson junction devices.

ACKNOWLEDGEMENTS

Everything was new to me when I first landed on New Jersey. Still I never expected to learn such amount of broad knowledge as a fresh graduate student. It was my advisor Prof. Eric L. Garfunkel who brought me the opportunity to grow. He is my role model for critical thinking, keeping an open mind, encouraging strong collaboration and developing my interpersonal skills. Instead of only focusing on individual steps, he emphasized the importance of knowing the big picture and strategy of a problem. Understanding the goal can help direct how best to draw research plans and clear roadblocks. With his help, I worked with an interdisciplinary team as well as obtained access to a large set of advanced technology instruments.

Although not official, Profs. Leonard C. Feldman and Torgny Gustafsson acted as co-advisors offering tremendous help and guidance for my research, especially when I started to work on the Helium Ion Microscope (see below). As physicists their thought processes were very helpful in explaining many of my research observations theoretically. I really appreciated learning from them, true scientists. Working with them was at times challenging because I always felt somewhat ignorant, especially on complex physics concepts needed to explain parts of my work. But my time with them was also very enjoyable because I started to gain the capability of judging my own results and ideas in front of excellent physicists.

Special thanks to Dr. Xiuyan Li (now also a professor at Shanghai Jiaotong University), Dr. Feixiang Luo, and Dr. Viacheslav Manichev. I worked closely with them for a couple years and without them I would have had a much harder time both starting and finishing my projects. They were always supportive and shared their knowledge with me without reservation.

I also want to thank Dr. Sylvie Rangan, Dr. Ryan Thorpe and Prof. Robert A. Bartynski for teaching and discussing about XPS, UPS and RBS. Dr. Alexei Ermakov showed me how to design and trouble-shooting an instrument with his magic hands (and mind). Dr. Spencer Porter showed me how to be a well-organized researcher. Dr. Hussein Hijazi showed me how to make full use of time. Fellow students Shinjae Hwang and Fangzhou Yu gave me advice on various aspects of my research and helped with collaboration. I'd like to extend my thanks to the other members of the group: Dr. Aleksandra B. Biedron, Dr. Malathi Kalyanikar, Dr. Anders Laursen, Hongbin Yang, Hengfei Gu, Mohamed Zeineldin, Ryan Crichton and Yifei Li.

During most of my time at Rutgers I was a member of the Center for Sustainable Materials Chemistry (CSMC – headquartered at Oregon State University) and funded by the U.S. National Science Foundation under Grant CHE-1102637. I'd like to thank my extensive collaborative work many in the CSMC team, including Profs. Douglas A. Keszler, Gregory S. Herman, Yves Chabal, May Nyman, and Drs. David Marsh, Sumit Saha, Jenn M. Amador, Ryan T. Frederick, Aaron Dangerfield, and J. Trey Diulus, Danielle Hutchison and all other CSMC members. Chapter 3 and 4 are composed in part results of this project published

in SPIE proceedings and ACS applied materials & interfaces as well as some work pending for publication (references in both chapters).

I would like to thank Prof. Xiaoxing Xi, Prof. Chen Ke and Dr. Leila Kasaei of Temple University for bringing us into a very exciting project to develop a new class of superconducting junctions structures. In this thesis, chapter 5 is composed in part of the published results in IEEE Transactions on Applied Superconductivity and Superconductor Science and Technology (references in chapter 5).

I would like to thank my committee members Profs. Eric L. Garfunkel, Leonard C. Feldman, Jing Li and Jane Hinch for their guidance, support and constructive suggestions on my thesis writing.

Finally, I want to take this opportunity to thank my family and Ms. Xue Yang for their unconditional love and support.

Table of Contents

ABSTRACT OF THE DISSERTATION.....	ii
ACKNOWLEDGEMENTS.....	vi
Table of Contents.....	ix
List of Figures	xii
List of Tables	xviii
List of Acronyms	xix
Chapter 1: Introduction.....	1
1.1 New challenges for Moore’s Law and nanofabrication	1
1.2 Nanofabrication with EUV lithography	4
1.2.1 Development of EUVL	4
1.2.2 EUVL resist candidates.....	8
1.2.3 Other patterning methods	13
1.3 Nanofabrication of Josephson Junctions	14
1.3.1 Josephson Junction characteristics	14
1.3.2 Fabrications of Josephson Junctions	19
Chapter 2: Technical Background	27
2.1 General Introduction.....	27
2.2 Atomic force microscope	28

2.3	X-ray photoelectron spectroscopy (XPS).....	30
2.3.1	X-ray photoelectron spectroscopy basics	30
2.3.2	Ambient Pressure X-ray photoelectron spectroscopy (APXPS)	32
2.4	Ultraviolet photoelectron spectroscopy (UPS)	34
2.5	Rutherford backscattering Spectrometry (RBS)	35
2.6	Helium ion microscope (HIM)	38
Chapter 3: The development of organotin resists and their radiation chemistry		
	41	
3.1	Introduction.....	41
3.2	Cluster to thin film.....	42
3.2.1	Thin film uniformity	43
3.2.2	As-deposited film chemical component.....	50
3.3	Radiation chemistry	56
3.3.1	X-ray exposure.....	56
3.3.2	UV exposure	59
3.3.3	Ambient pressure XPS (APXPS) ¹⁴	61
3.3.4	Possible radiation reaction pathways.....	74
Chapter 4: Patterning properties of organotin resist.....		80
4.1	Introduction.....	80
4.2	Best patterning performance achieved	83

4.2.1	Sensitivity.....	84
4.2.2	Critical dimension and LER.....	86
4.3	Etching selectivity	91
4.4	Interfacial bonding and substrate effects	93
4.4.1	Implications of interface bonding effects	93
4.4.2	Implications of extra secondary electron emission from substrates	97
Chapter 5:	Josephson Junction.....	105
5.1	Introduction.....	105
5.2	Large area	106
5.3	Array junction	112
Chapter 6:	Conclusion.....	118

List of Figures

Figure 1.1 Energy vs. delay in an arithmetic logic unit (ALU) implemented with beyond-CMOS devices. The sweet spot is marked with the red oval with low energy and short delay. ³	3
Figure 1.2 Atomic absorption cross section at EUV ($\lambda=13.5$ nm). ¹²	8
Figure 1.3 Flowchart of the edge-detection algorithm. ¹⁴	9
Figure 1.4 PSCAR reaction flow. ²⁰	12
Figure 1.5 Comparison of simulated chemical gradients after PEB.....	12
Figure 1.6 Schematic of a Josephson Junction. S_L and S_R are the left and right superconductors with pair wave function φ accordingly. ³¹	16
Figure 1.7 Expected Current-Voltage relation for a Josephson Junction.....	17
Figure 1.8 Contours of integration C_L and C_R used to derive the magnetic field dependence of the phase difference φ . ³¹	18
Figure 1.9 Typical behavior of critical current versus the applied magnetic field in a JJ device. ³²	18
Figure 2.1 Multiple characterization techniques for thin film surface/interface analysis.	27
Figure 2.2 Universal curve plot of electron IMFPs of various elements. ³	31
Figure 2.3 (a) Schematic representation of an elastic collision between an incident beam and the target; (b) Energy loss components for a projectile that scatters from depth t	36

Figure 2.4 Schematic representation of the probability for incident particles being deflected from the target nuclei.	37
Figure 2.5 Schematic of Carl Zeiss ORION HIM system. ⁹	38
Figure 3.1 Three precursors in progress.	41
Figure 3.2 AFM images and measured roughness of tin-based precursor with different solvents and concentrations.	44
Figure 3.3 AFM images of films prepared under different conditions.....	45
Figure 3.4 RBS spectra of a) Keggin film on HF etched silicon substrate and b) Commercial film on native oxide silicon substrate.	46
Figure 3.5 Scattering geometry of RBS with α as the incident angle, β as the exit angle and θ as the scattering angle.....	49
Figure 3.6 Grazing-angle RBS for keggin film on silicon. Black curve is the smoothed RBS data and red curve is simulated data.....	49
Figure 3.7. Sn 3d, Sn MNN, Na 1s, C 1s, O 1s, and Si 2p XPS spectra of commercial, keggin and football Sn precursor films.	51
Figure 3.8 (a) The Sn MNN Auger peaks of SnO, SnO ₂ and the conducting glass are shown. ¹² b. Experimental Sn MNN Auger spectra for Sn, SnO and SnO ₂ , respectively. ¹³	53
Figure 3.9 Atomic percent ratio of oxygen to tin for three precursor films.....	55
Figure 3.10 In situ XPS data comparison before and after exposure	56
Figure 3.11 XPS comparisons for exposed/unexposed areas are measured on the same sample after development. Grey spots on each sample are exposed	

areas and resist films remain on the surface. Blue areas are unexposed which show thick SiO ₂ color of the substrate.	56
Figure 3.12 XPS data comparison before and after development	57
Figure 3.13 Atomic percentage comparison before and after development	58
Figure 3.14 (a) Atomic calculation of photoionization cross-sections. (b) UPS and XPS valence band structure.	60
Figure 3.15 UPS valence band measurement on Keggin film with different exposing time.	61
Figure 3.16 APXPS obtained for β -NaSn ₁₃ in both UHV and P_{O2} = 1 Torr using $h\nu$ = 626 eV. (a) C 1s, (b) O 1s, and (c) Sn 3d core levels.	62
Figure 3.17 APXPS data obtained for different X-ray exposure times for C 1s in (a) UHV and (b) P_{O2} = 1 Torr, and O 1s in (c) UHV and (d) P_{O2} = 1 Torr.	65
Figure 3.18 X-ray induced changes in peak intensity ratios: C-H component of the C 1s spectra obtained in (a) UHV, (b) P_{O2} = 0.01 Torr, (c) P_{O2} = 1 Torr, and (d) Total O 1s spectra at $h\nu$ = 626 eV for indicated oxygen pressures. The indicated curves in the figure (b,c) are fits to equation 1, while the lines in figure (a) are fits to a linear function. In figure (d) the UHV data are fit to equation 1, while the ambient oxygen data are fits to a linear function.	67
Figure 3.19 TEY XAS obtained from a β -NaSn ₁₃ film.	70
Figure 3.20 Atomic percent calculations showing the compositional changes for C 1s, O 1s, and Sn 3d core levels and their respective chemical states after sequential C 1s scans (42 min of exposure) at $h\nu$ = 626 eV.....	73

Figure 3.21 Two possible pathways that the Sn Keggin cluster might experience under exposure, either of which would change the cluster solubility.	75
Figure 3.22 Proposed mechanism showing the conversion from β -NaSn ₁₃ to SnO ₂ . Photons are absorbed leading to photoemission (a), followed by electron scattering and generation of secondary electrons (b and c). The homolytic cleavage of butyl ligands (d) is enhanced in the presence of oxygen and provides a more efficient route to SnO ₂ (e, f, and g).	77
Figure 4.1 Incident particle options for use in micro- or nano-structure fabrication. ⁹	81
Figure 4.2 AFM image of patterned keggins film with dose from 1~16 $\mu\text{C}/\text{cm}^2$	85
Figure 4.3 Contrast curve of β -NaSn ₁₃ resist with 30 keV HIBL,	85
Figure 4.4 AFM line profiles of exposed area with dose at 8.9 and 10.5 $\mu\text{C}/\text{cm}^2$	86
Figure 4.5 Patterned samples: lines (10~50nm Dose: 10 $\mu\text{C}/\text{cm}^2$).....	88
Figure 4.6 Zoom in image of line patterns shows exposed material under wiggling lines.	89
Figure 4.7 Line patterns. (a) Dose scaling of 5, 10, 15 and 20 $\mu\text{C}/\text{cm}^2$ from right to left; (b) 20 nm half pitch dense line patterns.	89
Figure 4.8 (a), (b), (c) and (d) HIM images of line patterns exposed with doses of respectively 10, 15, 20, and 25 $\mu\text{C}/\text{cm}^2$. The scale bar is 200 nm for all images. The nominal line widths are 1, 2, 3, 4, 5, 10, 15, and 20 nm from left to right. A pair of each lines are shown.	90

Figure 4.9 (a) and (b) are SHIM images of line patterns used to calculate CD and LER for 10 nm and 20 nm thick film individually.	91
Figure 4.10 Line profiles after dry etching.	92
Figure 4.11 Square patterns for etching rate control.	92
Figure 4.12 40° tilted angle HIM image of etched dense line patterns.....	93
Figure 4.13 Images of Patterned lines of Keggin on Si-OH.	95
Figure 4.14 Images of Patterned lines of Keggin on Si-H.....	95
Figure 4.15 Images of Patterned lines of Keggin on SAM.	95
Figure 4.16 AFM invert mapping images (a), (b) and (c) of line patterns exposed to 15 $\mu\text{C}/\text{cm}^2$ on Si, SiO ₂ and Au coated glass substrate. The scale bar is 500 nm for all images. The nominal line widths are 1, 2, 3, 4, 5, 10, 15, and 20 nm from left to right. A pair of each lines are shown.	98
Figure 4.17 Monte Carlo simulation of (a) ion trajectories and (b) energy loss due to ionization in three samples with $\beta\text{-NaSn}_{13}$ photoresist (PR) on gold coated glass, silicon and silicon oxide substrates.	100
Figure 4.18 (a) Valence band spectra of $\beta\text{-NaSn}_{13}$ resist on gold substrate with increasing irradiation time. (b) Linear fitting of intensity change at 6.3 eV with $\beta\text{-NaSn}_{13}$ resist on three substrates.....	102
Figure 5.1 (a) TRIM simulation of the range of 30-keV He ⁺ ions in a 7 nm SiO ₂ /50 nm Ba122/LSAT substrate sample. (b) Schematic of the sample with a 4 μm \times 10 μm bridge. The blue area represents the pristine film. Figure 1. The focused He ⁺ ion beam was rastered over the red rectangle. The blowup of the irradiated area shows the raster pattern of the focused He ⁺ ion beam. The white dashed lines	

are guide to eye, showing a pixel size of 1.96 nm × 1.96 nm at the 100 nm FOV	
(c) TRIM simulation of the damage density profile for three adjacent single tracks of He ⁺ in the SiO ₂ /Ba122 sample at 5 × 10 ¹⁴ /cm ²	
(d) TRIM simulation of the damage density profile for three adjacent single tracks of He ⁺ in the MgO/MgB ₂ sample at 8 × 10 ¹⁵ /cm ²	108
Figure 5.2 Complete series of TEM BF micrographs of thin film of (10 nm MgO/25 nm MgB ₂ /on SiC substrate) irradiated by a 30 keV He ⁺ ion beam with increasing doses. The dose values on each micrograph are in ions/cm ²	110
Figure 5.3 High resolution TEM micrographs of the thin film of (10 nm MgO/25 nm MgB ₂ /on SiC substrate) irradiated with a helium ion dose of (a) 6 × 10 ¹⁶ /cm ² , (b) 5 × 10 ¹⁷ /cm ²	111
Figure 5.4 (a) Optical image of the array pattern. Large bonding pads attached to a centered meandering micro-strips. (b) Three branches of the meander are enlarged. Dark color lines are Au covered MgB ₂ . The tapered down bridges are SiO ₂ covered MgB ₂ . (c) Zoomed view of single tracks of He ⁺ irradiation at 100 nm inter-spacing on a 5 × 15 μm ² bridge imaged in HIM.	112
Figure 5.5(a) TRIM simulation of damage density in SiO ₂ /MgB ₂ (4+25nm) film deposited on SiC substrate when irradiated with 2.7 × 10 ¹⁶ /cm ² He ions. (b) Black dashed line represents damage profile at SiO ₂ /MgB ₂ interface with the area under the curve ~ 7.5 × 10 ²² . Blue dotted line represents damage profile at MgB ₂ /SiC interface with the area under the curve ~ 1.2 × 10 ²³	114

List of Tables

Table 3.1 Film thickness of $[(\text{BuSn})_{12}\text{O}_{14}(\text{OH})_6][\text{OH}]_2$ compound, commercial BuSnOOH and kegglin Sn13 compound: Ellipsometry thickness & AFM thickness	45
Table 3.2 Sn Auger parameter calculation for three films prepared from football, commercial, and keggling-based solutions.....	54
Table 3.3 XPS binding energy (eV) comparison among films	54
Table 3.4 Ratio of TEY from $\beta\text{-NaSn}_{13}$ resists normalized to $h\nu = 472$ eV. Ratio of X-ray attenuation for different photon energies and oxygen partial pressures normalized to UHV. Photoabsorption cross section values obtained from Henke, et al.....	70
Table 3.5 Bonding energy comparison within the Keggin cluster structure.	74
Table 4.1 Ion and photon beams both share the potential for high resolution and similar secondary electron generation process while HIM is more accessible than a commercial EUV scanner (because of cost).....	81
Table 4.2 CD and LER for line patterns of kegglin on Si-OH and Si-H and Si-SAM.....	96
Table 5.1 Characteristics of the Co-doped Ba122 and MgB_2 thin films used in this study.....	107

List of Acronyms

Å	Ångström
AFM	Atomic force microscope
APXPS	Ambient Pressure X-ray photoelectron spectroscopy
CAR	Chemically Amplified Resist
CD	Critical dimension
CMOS	Complementary metal–oxide–semiconductor
DSA	Directed self-assembly
EUV	Extreme ultra violet
FET	Field-effect transistor
FWHM	Full width half maximum
HAR	High aspect ratio
He	Helium
HIM	Helium ion microscope
HVM	High volume manufacture
IC	Integrated circuits
IMFP	Inelastic mean free path
IoE	Internet of everything
IoT	Internet of things
IRDS	International Roadmap for Devices and Systems
keV	Kilo electron volts

LER	Line edge roughness
LPP	Laser produced plasma
MeV	Mega electron volts
MOS	Metal–oxide–semiconductor
MOSFET	Metal–oxide–semiconductor field-effect transistor
PMMA	Poly(methyl methacrylate)
PR	Photoresist
PSCAR	Photosensitized Chemically Amplified Resist
RBS	Rutherford backscattering Spectrometry
RSFQ	Rapid single flux quantum
SE	Secondary electrons
SQUID	Superconducting quantum interference device
THF	Tetrahydrofuran
UPS	Ultraviolet photoelectron spectroscopy
XAS	X-ray absorption spectroscopy
XPS	X-ray photoelectron spectroscopy

Chapter 1: Introduction

1.1 New challenges for Moore's Law and nanofabrication

Moore's Law was an observation described firstly by Gordon Moore in 1965 and then developed into a forecast that the transistor density on integrated circuit (IC) chips would be doubling every two years without a significant cost. But nowadays the concept of Moore's Law brings together at least four trends, Koomey's Law, Dennard's Law, Metcalfe's Law and Emergent Behavior.¹ Koomey's Law emphasizes computational power-per-Watt. Dennard's Law notes that the power and performance gain by shrinking the physical dimension of the transistors and the spacing between them, based on specific electrical engineering rules.

Metcalfe's Law addresses the demand side of the value equation by drawing on the network effect of economics for the creation of demand. Emergent behavior is when order emerges from chaos due to a few simple rules based on complexity theory, which is the engine behind many of the prediction rules. The current concepts subsumed under Moore's Law help direct the continuous improvements in the semiconductor industry in terms of economic performance, system performance, device performance, creation of demand and creation of orders/rules for innovation.¹ This mechanism makes electronics more affordable and massive calculations more realizable. The Internet of Things (IoT) and the Internet of Everything (IoE) could never happen without powerful integrated chips on individual devices and efficient telecommunications. They provide the global network of physical objects accessed through the internet and change the methods of communications. The semiconductor industry becomes a key enabler

for a completely new ecosystem that has the capability for big data analytics, machine learning, as well as advancing most other aspects science, technology and health. The customization of consumer devices, sensors, and data centers has opened multiple applications and also provided many challenges for the semiconductor industry. It continues to be a growing and developing field that is far from mature.

The rate of scaling of current devices has slowed down, and eventually, the theoretical 2D topological limits will put a brake on that. As Gordon Moore has said: “No exponential is forever: but ‘Forever’ can be delayed!”² Lithography, metrology and emerging materials are regions of interest for many advanced device researchers. The International Roadmap for Devices and Systems (IRDS) suggests that “3D Power Scaling” will bring us into the third era of scaling.

Stacking multiple layers of transistors already exists at some level, and will eventually become a key short term solution to further increase the number of transistors per unit area. Combined with new materials/structures for low power devices, this should help extend Moore’s Law for at least another 10-15 years.

With more complex circuit structures and shrinking dimensions, lithography occupies about 70% of manufacturing steps for nodes less than 15 nm. It is vital to limit defects in this process and keep the cost reasonable. Currently, TSMC and Samsung are competing for the 7nm node market. This critical dimension employs immersion lithography which needs multiple patterning², increasing the cost as well as edge placement errors (EPE) and electrical defects. Extreme ultraviolet lithography (EUVL) is currently the solution for sub-10 nm node

patterning. However, for this process, there are many issues that affect implementation, including machine uptime and photoresist performance.

In-line monitors of defects and fast failure analysis set different requirements for metrology such as non-destructive analysis and critical dimension measurements to assure on-time delivery of problems and solutions. For example, metrology must provide feedback to enable meaningful process control in the vertical direction for high aspect ratio (HAR) structures used in 3D-NAND memory devices. It increases the difficulty for optical characterization and expands the demand for fast critical dimension electron/ion microscopes.

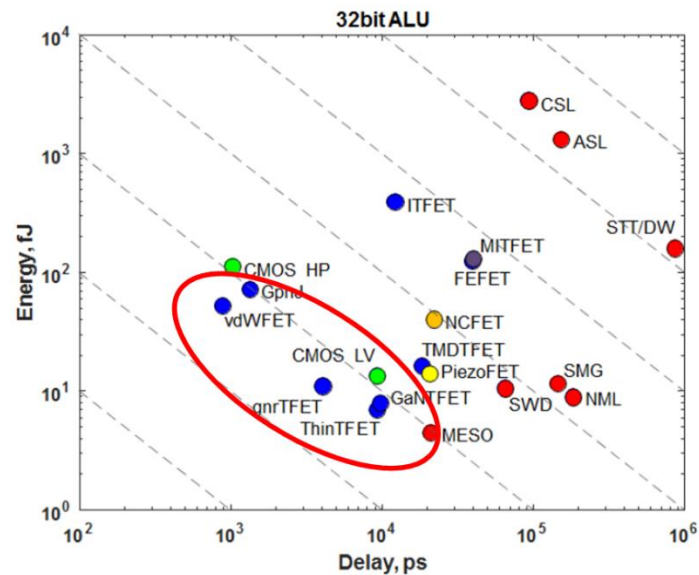


Figure 1.1 Energy vs. delay in an arithmetic logic unit (ALU) implemented with beyond-CMOS devices. The sweet spot is marked with the red oval with low energy and short delay.³

Devices utilized in the IoE environment need to consume the least amount of power and switch fast enough in order to ensure extended operability. This

requires operation at progressively lower supply voltage. It is very challenging to operate CMOS at 0.4-0.5V. This requirement is driving device research towards new configurations such as tunnel transistors (TFET) in Figure 1.1 that are expected to operate at voltages as low as 300mV or even lower. Neuromorphic computing structures also are of current interest because of their non-linear functionality and stronger connectivity which could benefit massive data calculations such as machine learning. And this particular structure could be even more efficient if implanted with quantum materials that might have more than two switching states. The development of new materials will likely be a long-term marathon. We need to fully understand the fundamental principles and relevant materials properties of any new device concept, and enable them to be brought together into realistic structures, to realize practical computing technologies.

1.2 Nanofabrication with EUV lithography

1.2.1 Development of EUVL

The laser wavelength used to power lithographic systems has not scaled as fast as the dimension of circuits due to the cost of developing and switching to completely new mechanisms. Initially, researchers were weighing the advantages between 157 nm and 13.5 nm photon sources (EUV). Unfortunately the 157 nm source does not offer a large enough leap in scaling to compensate for the development costs, while a 13.5 nm source allows the desired jump in feature size, although it has proven much more challenging to attain with a much longer development time (over two decades). The 193 nm photon source has

held the market for a very long time, benefitting from the implementation of immersion techniques (193i) that can give a higher numerical aperture without significant cost. However, when it comes to sub-20 nm feature size, the cost of the 193i lithography increases dramatically because of increased multiple patterning steps.² Thanks to two decades of continuous investment and efforts from both industrial and academic researchers, many challenges were overcome and EUV has finally become able to compete with 193i in terms of both performance and cost.

For EUVL, the source power is a crucial requirement as are other parameters such as dose stability, lifetime, etc. The power specification has evolved over the years and is driven by the need for lithography systems to print at both high resolution and ever-increasing productivity (wafers exposed/unit time). The conversion efficiency of the source and power utility of the whole scanner limits the power scaling. The currently targeted 7-nm node requires a lithography tool throughput with a source power of over 250 W to begin to think of high volume manufacturing (HVM). Laser produced plasma (LPP) is the primary source available in commercial EUV scanners.⁴ The CO₂ laser light is focused onto a tin droplet delivered by the droplet generator. The laser-plasma interaction takes place at the primary focus of the ellipsoidal collector mirror. The laser-droplet alignment is measured and carefully adjusted, providing feedback to maintain synchronization and optimal performance. Eventually collected EUV light gets redirected through the immediate focus aperture into the illumination optics of the

scanner. Hydrogen is used as a buffer gas to cool and clean this region efficiently.⁵

Most materials can heavily absorb EUV light. Carefully choosing EUV masks is another critical issue for the successful implementation of EUVL in the semiconductor fabrication process. The EUV mask structure is entirely different from that of conventional optical lithography. A nano-scale multilayer mirror coating (Mo/Si-based) is applied to reflect and tune the beam instead of using lens elements. Bragg reflection at several interfaces is necessary to minimize the loss of EUV photons and its efficiency is determined by the thickness of each layer and their ratios as well as the optical refractive index. The patterns with high EUV absorbance (Ta₂N₅ based) are deposited on the top of the reflection layers.

Photoresist absorption of EUV light is just as important as in the previous four wavelengths; however, the mechanism is very different from the mechanisms for absorbance of longer wavelengths (157 to 365 nm). At longer wavelengths, the light interacts with the molecules in the resist by exciting an electron (or lone-pair) from a molecular orbital to an empty (often antibonding) orbital. In EUV, however, the 92 eV photons initially remove electrons from deeper lying atomic orbitals in the absorber atoms, creating higher-energy electrons (~80 to 87 eV) and holes. One necessary consequence of these mechanistic differences is that the EUV absorbance is primarily determined by the elemental composition (and their respective absorption cross-sections at the EUV photon energy), and density of the absorbing atoms in the resist. By switching to EUV, all basic

exposure principle and photoresist reactions need to be studied as new.

Historically, researchers were struggling to find transparent resists for straight sidewalls in printed features under long-wavelength exposure. When it comes to EUV, they carried on that idea at the beginning.⁶ The earliest published trial by EUV exposure was done with PMMA, a common resist used in e-beam lithography and long-wavelength photolithography.⁷ Three key papers in 2008 caused the resist community to reconsider their efforts to make more-transparent resists and to make darker resists instead⁸⁻¹⁰. They found that increasing absorbance and photospeed determined by the quantum efficiency of the photoresists can give better line edge roughness and contrast. Until 2012, metal-based resists were first proposed as a solution to obtain enough EUV absorption.¹¹ And metal-based EUV resists have proven to be a promising and active area of research.

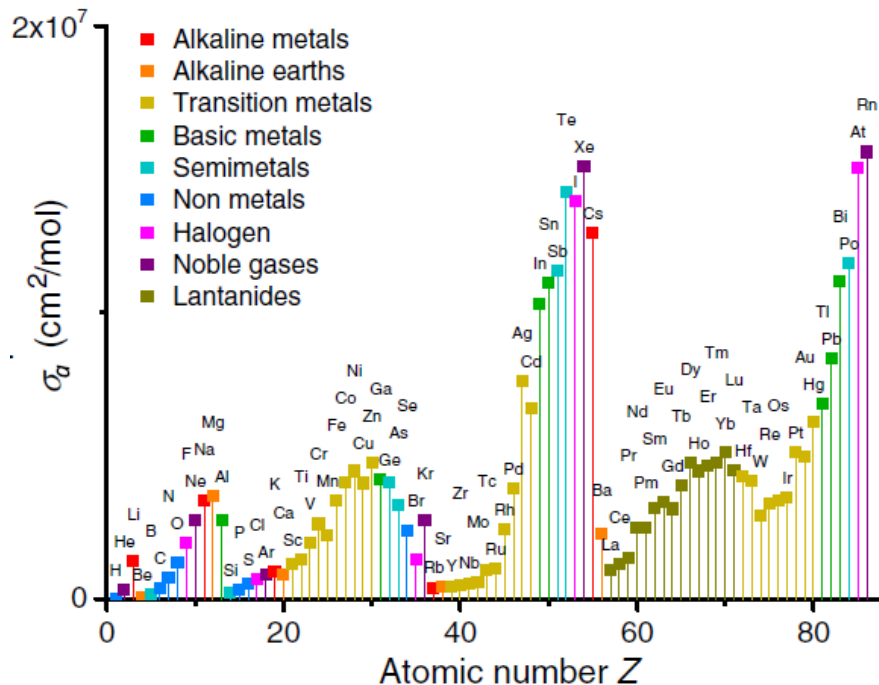


Figure 1.2 Atomic absorption cross section at EUV ($\lambda=13.5$ nm).¹²

1.2.2 EUVL resist candidates

1.2.2.1 Evaluation

For photoresist performance, there is always a trade-off among sensitivity, resolution and line-edge roughness (LER) (RLS trade-off).

LER is calculated as 3σ of the distances between a reference line and the edge

accordingly: $LER = 3\sqrt{\frac{\sum_{m=1}^n [y(x_m) - \bar{y}]^2}{n-1}}$. Linewidth roughness (LWR) is defined as

3σ of the line widths in each measured line. Resolution is usually represented by critical dimension (CD) which is calculated as a difference from distances

between a reference line to the one edge and another: $CD = \frac{1}{n} \sum_{i=1}^n (x_{ir} - x_{il})$.

And n is the number of points along the line edge.¹³

Typically, the top-down SEM images are used for LER measurement. The image selected for analysis is loaded in the software platform and its magnification and the pixel size (in nm) are specified. The analysis to follow is the determination of the edge pixel coordinates, the average edge position, the LER quantification, the maximum peak-to-valley distance, the skewness, and the kurtosis of the distribution of edge-heights.

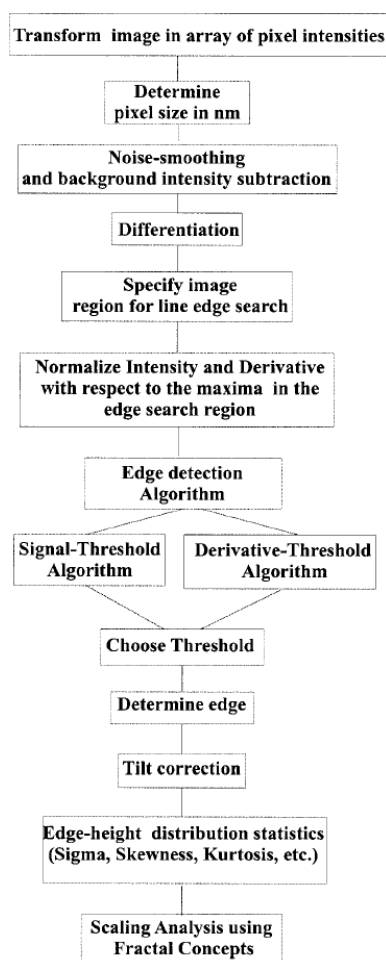


Figure 1.3 Flowchart of the edge-detection algorithm.¹⁴

The critical dose that removes (positive resists) or keeps (negative resists) the film thoroughly is considered as the exposure sensitivity. When the CD of features desired to print becomes smaller, the dose required to print these features tends to increase to achieve enough volume of reactions. With smaller CDs, stochastic effects tend to cause higher LER unless a higher-dose resist is used.

Tuning these three parameters to an optimum is a major goal of developing EUV photoresist materials.

1.2.2.2 Molecular Resist

PMMA is a typical positive tone molecular resist that has been widely used in traditional long-wavelength photolithography. The photochemical decomposition mechanism involves the homolytic cleavage of side-chain bonds firstly and then the formation of methyl formate and methanol. The chain scission reactions responsible for changes in developer solubility occur with only 5% quantum yield. This material has several disadvantages for EUVL: relatively poor sensitivity, significant outgas, quick erosion in SEM and poor etch resistance.

Hydrogen silsesquioxane (HSQ) has been utilized widely as a negative electron-beam resist. It is a cube-shaped molecule with the empirical formula of $\text{Si}_8\text{H}_8\text{O}_{12}$.¹⁵ Each Si atom is bonded to three oxygen and one hydrogen atom. The mechanism involves the cleavage of the Si–H bonds to form silanols (SiOH) in the presence of water which can further form a Si–O–Si bond. Thus the solubility will decrease in an alkaline developer like tetramethylammonium hydroxide (TMAH). Its small molecule size may benefit the ultimate resolution. Although it also has relatively low sensitivity and less stability during storage and processing which limit its industrial uses.¹⁶

Researchers added other functional groups to the HSQ structure to enhance the reaction efficiency or facilitate the removal of non-exposed areas. EUV lithography results showed significantly improved sensitivity with functionalities to increase reactivity (from 63 mJ/cm² to 7.2 mJ/cm²). Better LER/LWR with functionalities to increase solubility is also achieved (from 3.9 nm to 2.8 nm) without sacrificing the sensitivity.¹⁷

1.2.2.3 Chemically Amplified Resist (CAR)

Typical CAR contains a protected polymer structure, photo-acid generators (PAG) and photo-decomposable base (PDB, a quencher). During EUV exposure, photo-acid will be activated and quencher will start to decompose. During post-exposure bake (PEB), acid-quencher neutralization event will remove the protection cap on the polymer and the polymer will become soluble. CAR has demonstrated excellent sensitivity but their low resolution and high LWR may be considered drawbacks. The limitations with respect to LWR are mainly due to the stochastic effect of photo-acids and photon shot noise which is the time-dependent fluctuations due to the particle nature of light.¹⁸ Acid diffusion blur is an unavoidable consequence of acid-catalyzed resist imaging processes for both positive and negative EUV resists. The challenge is to design resists that will minimize resolution damage caused by acid diffusion without decreasing the resist sensitivity.

Photosensitized Chemically Amplified Resist (PSCAR) was first proposed in 2013 as a promising solution to achieve increased resist sensitivity while maintaining other high performance.¹⁹ It has a particular photosensitization system selective to EUV exposed area with a UV flood exposure. After EUV exposure, the acid-quencher neutralization reaction has to compete with the photosensitizer (PS) generation reaction. And PS will be in the exposed area only. Then a UV flood is applied to the whole wafer, more PAG and PDB will be decomposed by UV excited PS in EUV exposed area which adds additional acids and deactivates more quenchers.

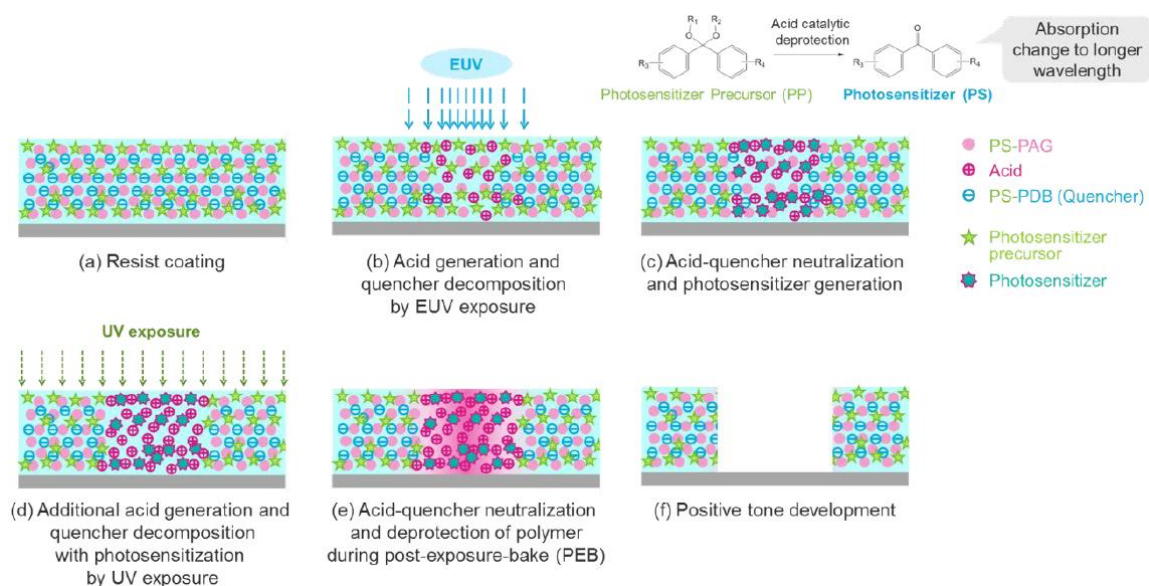


Figure 1.4 PSCAR reaction flow.²⁰

Simulated chemical gradients in Figure 1.5 showed improved FWHM of the resist reactors spread which can reduce the impact of dose stochasticity. As a result, better contrast and suppressed roughness were achieved.²⁰

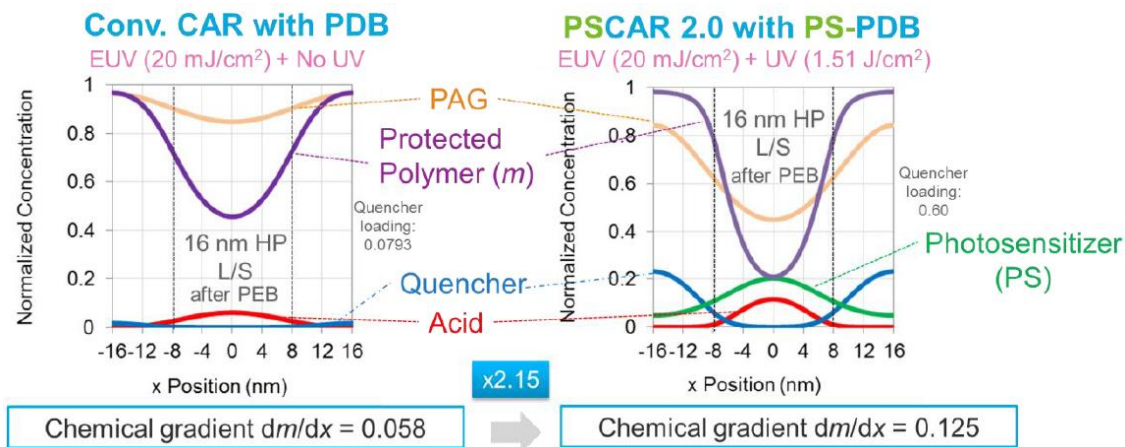


Figure 1.5 Comparison of simulated chemical gradients after PEB between conventional CAR (left) and PSCAR 2.0 (right).²¹

1.2.2.4 Metal-Containing Resist (MCR)

Resists with dark elements were first reported in 2008. The same year, metal oxide sulfates were first reported by Keszler's group to have competing resolution and sensitivity with e-beam lithography.²² Since then they announced first commercial MCR product with Inpria and made MCR a popular candidate for EUVL. Because of the high photoabsorption cross section of metal content in the film, it can give much better photon shot noise by absorbing a lot more photons into a smaller volume. It also has much higher etching selectivity to lots of different materials.²³

Various types of structures were developed recently like metal oxide resists with inorganic core and organic shell by Ober's group as well as molecular organometallic resist by Brainard's group.^{24, 25} Their proposed mechanisms share the similar idea which is making use of the metal as a photo absorber and transfer energy to a connected organic group. Cleavage will occur at the metal organic bonding. Then the unbonded site will either connect with another cluster or lose another organic group to form a smaller decomposed molecule. The solubility will be switched afterwards.

While metal-containing resists have several advantages, some concerns may arise from impurities and metallic contamination of critical layers.

1.2.3 Other patterning methods

Despite many challenges, optical lithography continues to enable an exponential decrease in the dimensions of circuit patterns that are printed in high volume in

advanced microelectronics. Researchers are also seeking other methodologies for different applications.

Nanoimprint lithography has made significant progress in the last two years.

Defect levels and throughput have both been improved. Since the feature sizes on the template are the same size as the printed features, the templates are difficult to make for leading-edge feature sizes. But 3D flash memory has much larger feature sizes and could be a proper application of nanoimprint considering the feasibility and cost.

DSA has very different stochastics than traditional resist. As feature sizes shrink, stochastic issues will become more critical, and this may be an opportunity for DSA compared to traditional resist.

For research materials or mask patterns that require extremely accurate CD and pattern transfer, maskless lithography like the focused electron/ion beam would give more flexibility and control.

1.3 Nanofabrication of Josephson Junctions

1.3.1 Josephson Junction characteristics

A Josephson junction (JJ) is a quantum mechanical device, which is made of two superconducting electrodes separated by a barrier which could be any non-superconducting material like insulating barrier, metal, semiconductor, and ferromagnet. A supercurrent will flow indefinitely long without any voltage applied. This phenomenon is called the Josephson Effect named after the British physicist Brian David Josephson who predicted this mathematical relationship in 1962.²⁶

Philip Anderson and John Rowell first reported the experimental observation showing the Josephson Effect in 1963.²⁷ JJs have essential applications in quantum-mechanical circuits, such as superconducting quantum interference devices (SQUIDs), superconducting qubits, Rapid single flux quantum (RSFQ) digital electronics, and thermometry/voltage standards. A conventional Josephson Voltage Standard (JVS) has been a better alternative to a Weston cell with improved accuracy of dc voltage measurement. The primary reason is that the Josephson voltage depends only on the frequency which can be obtained from an atomic clock (known with better than 1.7×10^{-16} uncertainty)²⁸. Currently, the programmable Josephson voltage standard (PJVS) is widely used for dc and ac voltage calibration²⁹. The pulse-driven ac Josephson voltage standard (ACJVS) is used for audio-frequency applications and low voltage applications as quantum voltage noise source (QVNS) for noise thermometry³⁰.

There are different approaches to confirm the Josephson effects of a device.³¹

The first is based on the Josephson equation that shows a typical voltage-current behavior. Considering the tunneling structure superconductor-barrier-superconductor and $\varphi_R(\varphi_L)$ is the pair wave function for the right (left) superconductor. Each superconducting electrode can be represented by a single quantum state, so $|\varphi|^2$ is the actual Cooper pair density. If the weak coupling exists between two superconductors, the transition between the two states (right and left) can occur. This coupling is related to the finite overlap of the two pair wave. The time evolution can be solved by the Schrödinger equation which gives

$$\frac{\partial \varphi}{\partial t} = \frac{2eV}{\hbar}.$$

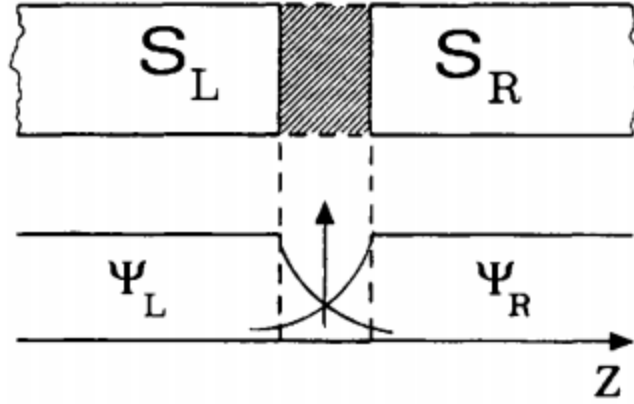


Figure 1.6 Schematic of a Josephson Junction. S_L and S_R are the left and right superconductors with pair wave function φ accordingly.³¹

Assuming the current density of each superconductor are the same constant ρ_1 , then the pair current density $J = J_1 \sin \varphi$, where $J_1 = 2K/\hbar\rho_1$. K is the coupling amplitude of the two-state system measuring the coupling interaction between two superconductors. The junction structure like geometry and barrier type will affect the coupling interaction and further change the K .

Based on these two relations, when V equals zero, the phase difference φ can be a constant (not zero) and a finite current density with a maximum value J_1 can flow through the barrier with zero voltage drop across the junction as shown in Figure 1.7. Once the critical voltage is applied, a finite resistance will exist.

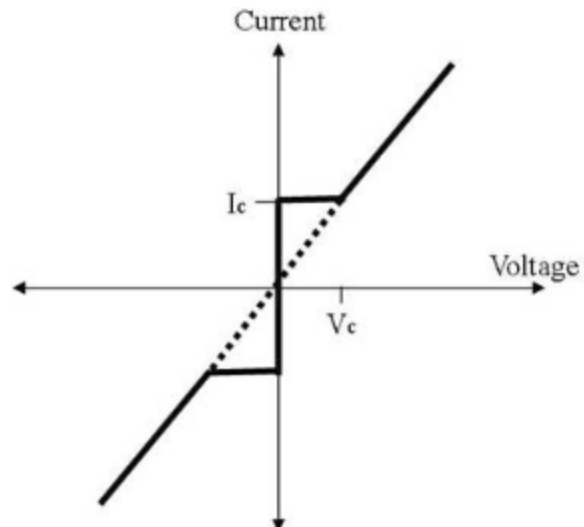


Figure 1.7 Expected Current-Voltage relation for a Josephson Junction.

Examine magnetic field effect is another way to verify characteristic of JJ devices. With a magnetic field H applied to the junction along the y axis, the gauge invariant phase difference between two points (x and $x+dx$) of the barrier in each superconductor can be expressed as $\nabla\varphi_{L,R} = \frac{2e}{\hbar c} \left(\frac{mc}{2e^2\rho} \mathbf{J}_s + \mathbf{A} \right)$, where \mathbf{J} is the electric current density, \mathbf{A} is the vector potential.

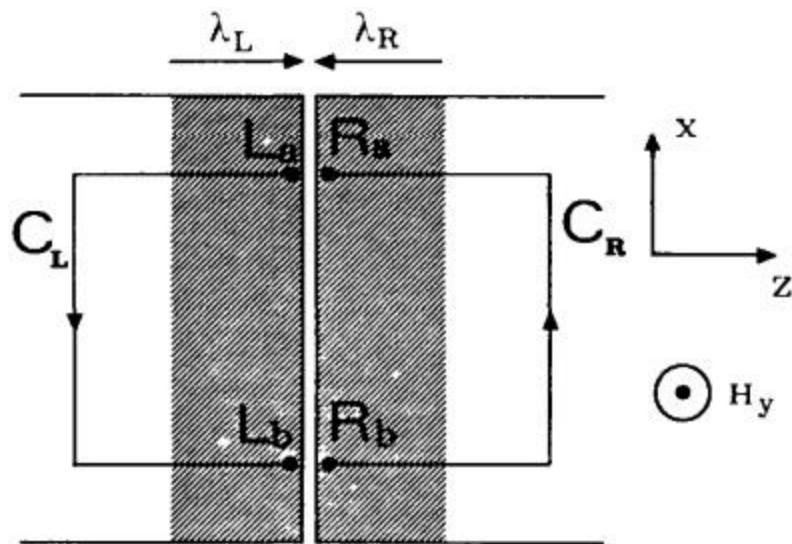


Figure 1.8 Contours of integration C_L and C_R used to derive the magnetic field dependence of the phase difference φ .³¹

The London depths should be much smaller than the thickness of the superconducting films so we can neglect the barrier thickness. By integration along the contours C_L and C_R (Figure 1.8), we can get $\frac{d\varphi}{dx} = \frac{2e}{\hbar c}(\lambda_L + \lambda_R + t)H_y$, where λ_L and λ_R are the London depths in the left and right superconductors, t is the dielectric barrier thickness. After integration, the phase difference $\varphi = \frac{2e}{\hbar c}dH_yx + \varphi_0$, where the magnetic penetration $d = \lambda_L + \lambda_R + t$. So $J = J_1 \sin(\frac{2e}{\hbar c}dH_yx + \varphi_0)$ which tells that the tunneling supercurrent can be manipulated by the magnetic field. It results in an interference pattern which in analogy to single slit experiment called Fraunhofer pattern and shown in Figure 1.9.

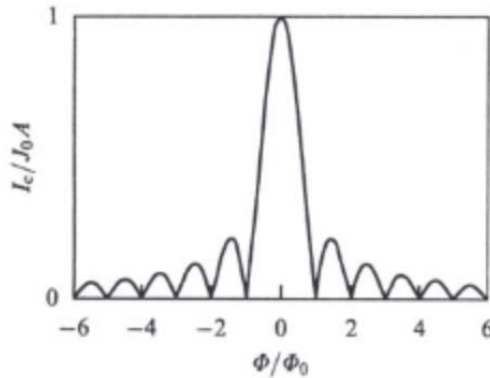


Figure 1.9 Typical behavior of critical current versus the applied magnetic field in a JJ device.³²

1.3.2 Fabrications of Josephson Junctions

A thin-film based three-layer sandwich structure is commonly used. High quality interface is assured either by an extra chemical or ion milling etching with “ex-situ” fabrication process or by “in-situ” deposition of all layers without any exposure to the atmosphere. In addition, the coherence length of superconducting materials limits the dimension of the barriers into the nanometer scale. Thanks to today’s advanced manufacturing process, a reliable single junction with sub-10nm thick barrier can be obtained. Magnetron sputtering for noble metal (like Nb) based JJ³³ or molecular beam epitaxy (MBE) growth for oxide heterostructures (like YBa₂Cu₃O_{7- δ}) based JJ³⁴ have demonstrated successful circuits functionalities. When scaling up superconducting circuits, some of the qubits and their coupling resonators are required to have precisely the same energy-level spacing in order to achieve high fidelity multi-qubit gates. However, due to limitations in fabrication techniques, it is almost impossible to make perfectly identical Josephson junctions based on conventional sandwich structures.

Intrinsic stacked junctions take advantage of their unique naturally exist quantum phase transition properties which can provide reliable consistency. Josephson coupling between CuO₂ double layers has successfully been proved in Bi₂Sr₂CaCu₂O₈³⁵ and Tl₂Ba₂Ca₂Cu₃O₁₀ single crystals and thin films³⁶ with effective barriers of the order of the separation of the CuO₂ double layers (1.5 nm). Limited material choices, complicated process and intrinsic heating effects become the roadblocks for its practical applications.

An alternative approach to fabricate Josephson junctions is using focused ion beam direct writing. Here, the focused ion beam locally weakens or destroys the superconducting properties of the film to create a junction barrier. The effects of ion irradiation on the properties of various superconductors have been well documented, for example, in high-temperature superconductors³⁷, iron-based pnictide superconductors³⁸, and MgB_2 ³⁹. In a Josephson junction, the two superconductor films must be separated by only about a coherence length apart in order to achieve the interference of the superconducting order parameters in the two superconductors. Heavy ions like gallium, with a focused ion beam spot size of 5 nm, cannot be used to define such a narrow junction barrier for superconductors with short coherence lengths. In contrast, the Helium Ion Microscope (HIM) creates a beam of light He^+ ions and can deliver a focused beam with a diameter of less than 0.5 nm, comparable to the short coherence lengths in high-temperature cuprate superconductors and iron-based pnictides. Cybart *et al.* have successfully demonstrated nano Josephson tunnel junctions in $\text{YBa}_2\text{Cu}_3\text{O}_{7-\delta}$ by using the focused helium ion beam⁴⁰. The short coherence length of ~ 2.5 nm of $\text{BaFe}_{1.84}\text{Co}_{0.16}\text{As}_2$ (Co-doped Ba122)⁴¹ also demands a narrow barrier region to permit Josephson coupling, making the direct writing with focused He^+ ion beam a promising path for fabricating pnictide Josephson junctions.

It is also beneficial to develop lumped element arrays instead of distributed arrays. In a lumped-element array, all of the junctions are placed in less than one-quarter of the wavelength of the RF drive frequency so that the phase of the

junctions is synchronized by the applied RF signal leading to a higher voltage for a given microwave. This sets a stringent limit for the spacing between adjacent junctions in the array. For instance, a drive frequency of 16 GHz and 13500 series junctions requires a 120 nm spacing ⁴². Moreover, the heat generated in the stacked-junction array is difficult to be dissipated compared to a planar configuration, which⁴³ allows the heat to be readily transferred to the substrate ⁴³. The quality of the Nb-based JJ array is excellent, fabrication of 1000 Nb/Al-AIO_x/Nb JJs for very large scale integration (VLSI) has been reported with the I_c spread from 0.8% to 8% for JJs with sizes from 1500 nm down to 200 nm ⁴⁴. In addition, the I_c spread of less than 1.6% was obtained for a series array of 200 NbTiN/Al-AIN_x/NbTiN Josephson tunnel junctions ⁴⁵. However, the transition temperature of Nb at 9.25 K or NbTiN at 14.2 K requires the device to operate at 4.2 K or < 10 K.

In the following chapters, I'll first briefly introduce the main techniques used in the thesis in Chapter 2. In Chapter 3, the development for precursor clusters to thin film of the tin-based photoresist candidates will be discussed. Meanwhile we proposed possible radiation chemistry of the chosen model resist. In Chapter 4, we used focused helium ion beam to evaluate the patterning performance of the model resist. Interface and underlayer effects were explored with ion radiation, photon radiation and analyzed by simulation methods and FT-IR results. Chapter 5 covers the successful nanofabrication of planar structure Josephson Junctions using focused helium ion beam. TRIM simulation was used to estimate the damage events.

Reference

1. Hutcheson, G. D., *Moore's law, lithography, and how optics drive the semiconductor industry*. SPIE: 2018; Vol. 10583.
2. Bakshi, V., *EUV lithography*. Spie Press: 2009; Vol. 178.
3. Pan, C.; Naeemi, A., An expanded benchmarking of beyond-CMOS devices based on Boolean and neuromorphic representative circuits. *IEEE Journal on Exploratory Solid-State Computational Devices and Circuits* **2017**, 3, 101-110.
4. Fomenkov, I. V.; Cymer, L.; Schafgans, A. A.; Cymer, L.; Brandt, D. C.; Cymer, L.; Ershov, A.; Tao, Y.; Vaschenko, G. O.; Cymer, L., EUV sources for high-volume manufacturing. **2018**.
5. Fomenkov, I. V.; Brandt, D. C.; Bykanov, A. N.; Ershov, A. I.; Partlo, W. N.; Myers, D. W.; Böwering, N. R.; Vaschenko, G. O.; Khodykin, V.; Hoffman, J. R. In *Laser-produced plasma source system development*, Emerging Lithographic Technologies XI, International Society for Optics and Photonics: 2007; p 65173J.
6. Dai, J.; Ober, C. K. In *Novel resists with nontraditional compositions for EUV lithography*, Advances in Resist Technology and Processing XXI, International Society for Optics and Photonics: 2004; pp 508-517.
7. Namioka, T., Current research activities in the field of multilayers for soft X-rays in Japan. *Revue de physique appliquée* **1988**, 23 (10), 1711-1726.
8. Kozawa, T.; Tagawa, S.; Santillan, J. J.; Toriumi, M.; Itani, T., Feasibility study of chemically amplified extreme ultraviolet resists for 22 nm fabrication. *Japanese Journal of Applied Physics* **2008**, 47 (6R), 4465.
9. Sasaki, T.; Yokokoji, O.; Watanabe, T.; Kinoshita, H. In *Development of partially fluorinated EUV-resist polymers for LER and sensitivity improvement*, Advances in Resist Materials and Processing Technology XXV, International Society for Optics and Photonics: 2008; p 692347.
10. Gronheid, R.; Van Roey, F.; Van Steenwinckel, D., Using KLUP for understanding Trends in EUV resist performance. *Journal of Photopolymer Science and Technology* **2008**, 21 (3), 429-434.
11. Mark, N.; Cho, K.; Petrillo, K., The physics of EUV photoresist and how it drives strategies for improvement. *Journal of Photopolymer Science and Technology* **2012**, 25 (1), 87-94.
12. Fallica, R.; Stowers, J. K.; Grenville, A.; Frommhold, A.; Robinson, A. P.; Ekin, Y. J. J. o. M. N., MEMS, MOEMS, Dynamic absorption coefficients of chemically amplified resists and nonchemically amplified resists at extreme ultraviolet. **2016**, 15 (3), 033506.
13. Levinson, H. J., *Principles of lithography*. SPIE press: 2005; Vol. 146.
14. Patsis, G.; Constantoudis, V.; Tserepi, A.; Gogolides, E.; Grozev, G., Quantification of line-edge roughness of photoresists. I. A comparison between off-line and on-line analysis of top-down scanning electron microscopy images. *Journal of Vacuum Science Technology B: Microelectronics Nanometer Structures Processing, Measurement, Phenomena* **2003**, 21 (3), 1008-1018.
15. Lampert, C. M. J. S. E. M., Coatings for enhanced photothermal energy collection I. Selective absorbers. **1979**, 1 (5-6), 319-341.

16. Yang, J. K.; Cord, B.; Duan, H.; Berggren, K. K.; Klingfus, J.; Nam, S.-W.; Kim, K.-B.; Rooks, M. J., Understanding of hydrogen silsesquioxane electron resist for sub-5-nm-half-pitch lithography. *Journal of Vacuum Science & Technology B: Microelectronics and Nanometer Structures Processing, Measurement, and Phenomena* **2009**, 27 (6), 2622-2627.
17. Gädda, T.; Luong, N. D.; Laukkanen, M.; Karaste, K.; Kähkönen, O.; Kauppi, E.; Kazazis, D.; Ekinici, Y.; Rantala, J. In *Advanced EUV negative tone resist and underlayer approaches exhibiting sub-20nm half-pitch resolution*, Advances in Patterning Materials and Processes XXXVI, International Society for Optics and Photonics: 2019; p 109600B.
18. Naulleau, P.; Anderson, C.; George, S., EUV Resists: Illuminating the challenges. *Journal of Photopolymer Science and Technology* **2011**, 24 (6), 637-642.
19. Tagawa, S.; Enomoto, S.; Oshima, A., Super high sensitivity enhancement by photo-sensitized chemically amplified resist (PS-CAR) process. *Journal of Photopolymer Science and Technology* **2013**, 26 (6), 825-830.
20. Nagahara, S.; Carcasi, M.; Shiraishi, G.; Kamei, Y.; Nafus, K.; Minekawa, Y.; Ide, H.; Kondo, Y.; Shiozawa, T.; Yoshida, K. In *EUV resist sensitization and roughness improvement by PSCAR with in-line UV flood exposure system*, Advances in Patterning Materials and Processes XXXV, International Society for Optics and Photonics: 2018; p 1058606.
21. Nagahara, S.; Carcasi, M.; Shiraishi, G.; Nakagawa, H.; Dei, S.; Shiozawa, T.; Nafus, K.; De Simone, D.; Vandenberghe, G.; Stock, H.-J. In *Photosensitized Chemically Amplified Resist (PSCAR) 2.0 for high-throughput and high-resolution EUV lithography: dual photosensitization of acid generation and quencher decomposition by flood exposure*, Advances in Patterning Materials and Processes XXXIV, International Society for Optics and Photonics: 2017; p 101460G.
22. Stowers, J.; Keszler, D. A., High resolution, high sensitivity inorganic resists. *Microelectronic Engineering* **2009**, 86 (4-6), 730-733.
23. De Simone, D.; Pollentier, I.; Vandenberghe, G. J. J. o. P. S.; Technology, Metal-containing materials as turning point of EUV lithography. **2015**, 28 (4), 507-514.
24. Sitterly, J.; Murphy, M.; Grzeskowiak, S.; Denbeaux, G.; Brainard, R. L., *Molecular organometallic resists for EUV (MORE): Reactivity as a function of metal center (Bi, Sb, Te and Sn)*. SPIE: 2018; Vol. 10586.
25. Sakai, K.; Jung, S.-H.; Pan, W.; Giannelis, E. P.; Ober, C. K., *Metal organic cluster photoresists: new metal oxide systems*. SPIE: 2019; Vol. 10963.
26. Josephson, B. D., Possible new effects in superconductive tunnelling. *Physics letters* **1962**, 1 (7), 251-253.
27. Anderson, P. W.; Rowell, J. M., Probable observation of the Josephson superconducting tunneling effect. *Physical Review Letters* **1963**, 10 (6), 230.
28. Benz, S. P.; Dresselhaus, P. D.; Chong, Y.; Burroughs, C. J., Stacked nanoscale Josephson junction arrays for high-performance voltage standards. **2002**.

29. Schulze, H.; Behr, R.; Kohlmann, J.; Müller, F.; Niemeyer, J., Design and fabrication of 10 V SINIS Josephson arrays for programmable voltage standards. *Superconductor Science and Technology* **2000**, 13 (9), 1293.
30. Benz, S. P.; Hamilton, C. A., Application of the Josephson effect to voltage metrology. *Proceedings of the IEEE* **2004**, 92 (10), 1617-1629.
31. Barone, A.; Paterno, G., *Physics and applications of the Josephson effect*. Wiley: 1982.
32. Van Harlingen, D. J., Phase-sensitive tests of the symmetry of the pairing state in the high-temperature superconductors—evidence for $d_{x^2-y^2}$ symmetry. *Reviews of Modern Physics* **1995**, 67 (2), 515.
33. Tolpygo, S. K.; Bolkhovskiy, V.; Weir, T. J.; Johnson, L. M.; Gouker, M. A.; Oliver, W. D., Fabrication Process and Properties of Fully-Planarized Deep-Submicron Nb/Al- AlO_x /Nb Josephson Junctions for VLSI Circuits. *IEEE transactions on Applied Superconductivity* **2014**, 25 (3), 1-12.
34. Biswas, A.; Talha, M.; Kashir, A.; Jeong, Y. H., A thin film perspective on quantum functional oxides. *Current Applied Physics* **2019**, 19 (3), 207-214.
35. Kleiner, R.; Steinmeyer, F.; Kunkel, G.; Müller, P., Intrinsic Josephson effects in $\text{Bi}_2\text{Sr}_2\text{CaCu}_2\text{O}_{8-x}$ single crystals. *Physical review letters* **1992**, 68 (15), 2394.
36. Yurgens, A., Intrinsic Josephson junctions: recent developments. *Superconductor Science and Technology* **2000**, 13 (8), R85.
37. Lang, W.; Pedarnig, J. D., Ion irradiation of high-temperature superconductors and its application for nanopatterning. In *Nanoscience and Engineering in Superconductivity*, Springer: 2010; pp 81-104.
38. Eisterer, M., Radiation effects on iron-based superconductors. *Superconductor Science and Technology* **2017**, 31 (1), 013001.
39. Putti, M.; Vaglio, R.; Rowell, J., Radiation effects on MgB_2 : a review and a comparison with A15 superconductors. *Superconductor Science and Technology* **2008**, 21 (4), 043001.
40. Cybart, S. A.; Cho, E.; Wong, T.; Wehlin, B. H.; Ma, M. K.; Huynh, C.; Dynes, R., Nano Josephson superconducting tunnel junctions in $\text{YBa}_2\text{Cu}_3\text{O}_{7-\delta}$ directly patterned with a focused helium ion beam. *Nature nanotechnology* **2015**, 10 (7), 598.
41. Kano, M.; Kohama, Y.; Graf, D.; Balakirev, F.; S. Sefat, A.; A. Mcguire, M.; C. Sales, B.; Mandrus, D.; W. Tozer, S., Anisotropy of the upper critical field in a Co-doped BaFe_2As_2 single crystal. *Journal of the Physical Society of Japan* **2009**, 78 (8), 084719.
42. Benz, S. P.; Dresselhaus, P. D.; Burroughs, C. J., Nanotechnology for next generation Josephson voltage standards. *IEEE Transactions on Instrumentation and Measurement* **2001**, 50 (6), 1513-1518.
43. Chong, Y.; Dresselhaus, P. D.; Benz, S. P., Thermal transport in stacked superconductor–normal metal–superconductor Josephson junctions. *Applied physics letters* **2003**, 83 (9), 1794-1796.
44. Tolpygo, S. K.; Bolkhovskiy, V.; Weir, T. J.; Johnson, L. M.; Gouker, M. A.; Oliver, W. D., Fabrication process and properties of fully-planarized deep-

submicron Nb/Al-AlO_x/Nb Josephson junctions for VLSI circuits. *IEEE Trans. Appl. Supercond* **2015**, 25 (3), 1101312.

45. Akaike, H.; Sakamoto, S.; Munemoto, K.; Fujimaki, A., Fabrication of NbTiN/Al/AlN_x/NbTiN Josephson junctions for superconducting circuits operating around 10 K. *IEEE Trans. Appl. Supercond* **2016**, 26, 1100805.

Chapter 2: Technical Background

2.1 General Introduction

In this thesis, we focus on new resist materials, their modification under exposure and their patterning properties as well as novel direct writing method for planar structure Josephson Junctions. To understand these behaviors, we make use of multiple thin film analytical techniques described in this chapter. In general, the characterization techniques used in this study can be simply defined as shown in Figure 2.1. We are probing the surface/interface with scanning tips, ion source, electron source, x-ray source and UV source. We employ the emitted ions and electrons with various energy to get the information of the thin films.

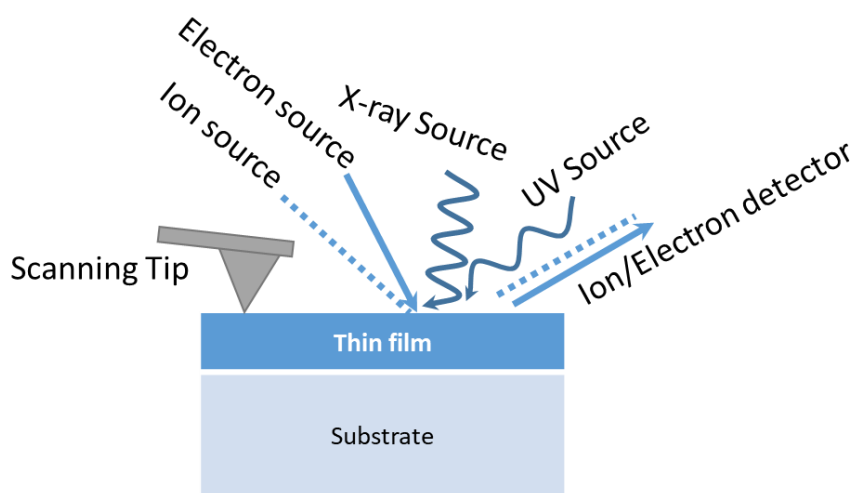


Figure 2.1 Multiple characterization techniques for thin film surface/interface analysis.

With scanning tips that are sensitive to different physical/chemical properties of the surface, we can get topography, adhesiveness, surface charging and so on.

By collecting backscattered ions, we can calculate the ion energy loss during the collision events in samples and then further calculate thin film components. With position sensitive detectors, we can also produce images by emitted ions or electrons.

In all electron spectroscopies, energy analysis of electrons emitted from the solid surface is used to gain information on the electronic energy levels in the surface region. These energy levels can be roughly divided into two groups: core levels and valence levels. So we can determine atomic species and local chemical environment at surface of the films.

2.2 Atomic force microscope

Atomic force microscopy (AFM) belongs to the family of microscopes with scanning probes (SPM - Scanning Probe Microscopy). Due to the flexibility of probing various surface properties by changing probes, AFM becomes one of the most common instruments for solid state material research. It makes use of either attractive force (non-contact mode) or repulsive force (contact mode) between the very sharp probe and the sample surface at a small distance. When the probe is scanning the surface, the force will drive the probe to move accordingly with the piezoelectric actuators. A laser beam will be sent to the back side of the probe holder (cantilever), with the probe movement, the deflected laser will show position shifts on the position sensitive photo detector (PSPD). PSPD and probe piezoelectric actuators will form a feedback loop to control the distance between the probe and the surface during scanning. By applying a nanometer scale tip and high resolution movement control, AFM is able to

achieve sub-nanometer resolution on the z axis. The stiffness of the cantilever should be small enough to deform based to the sample topography which translates to 10 to 130 N/m in our experiments. The tip radius of curvature was guaranteed to be less than 10 nm.

The force between the tip and the sample surface is dependent of tip-surface distance. At larger distances, electrostatic or van der Waals forces originally from the polarization interaction between atoms will be the dominant and the attractive force will be used for measurements. At smaller distances (a few Ångströms), due to electronic orbitals overlap at atomic distances, a very strong repulsive force appears between the tip and sample atoms repulsive forces.

At measurement, when cantilever deformation is kept at a constant value and the tip-surface force is repulsive, this type is referred to the contact mode. When the tip is oscillating in z-axis at its resonant frequency, the tip-surface attractive force will result in shifts of the resonant frequency. The feedback loop will keep the tip at such distance where the frequency shift or change of amplitude is constant. This type is referred to the non-contact mode. Contact mode imaging can damage samples and distort image data by frictional and adhesive forces. We choose non-contact mode for our photoresist samples.

The resonance frequency of the straight shape cantilever

$$f_0 = \frac{1}{2\pi} \left(\frac{k}{m_0} \right)^{0.5} \quad k = \frac{Ewt^3}{4l^3}$$

k: the spring constant, E: Young module; t: thickness; l: length; w: width, m_0 : the effective mass of the lever.

During the measurement, the tip is rastering the surface and provides information about the local height of the surface. Acquired data is further processed and analyzed to draw line scan profile and calculate the surface roughness by using free software Gwyddion.¹

2.3 X-ray photoelectron spectroscopy (XPS)

2.3.1 X-ray photoelectron spectroscopy basics

A photon of energy $h\nu$ penetrates the surface, and is absorbed by an electron with a binding energy E_b , which then escapes from the surface with a kinetic energy ($E'_k = h\nu - E_b$) determined by an electron energy analyzer from the relation: $E_k = E'_k - (\phi_{spec} - \phi_s)$, where ϕ_{spec} and ϕ_s are work functions of the spectrometer and the sample. So $h\nu = E_b + E_k + \phi_{spec}$.²

The escaped electron has to have enough kinetic energy to reach the detector. Figure 2.2 gives the inelastic mean free path (IMFP) of electrons with various kinetic energy. A broad range of small IMFP at 4~10Å represents electrons with energy between 10 and 500 eV which sets the limitation of how deep XPS can probe. In general, XPS can acquire electrons from depths less than or equal to three times of the IMFP. So it is a surface sensitive technique and not proper for studying bulk material.

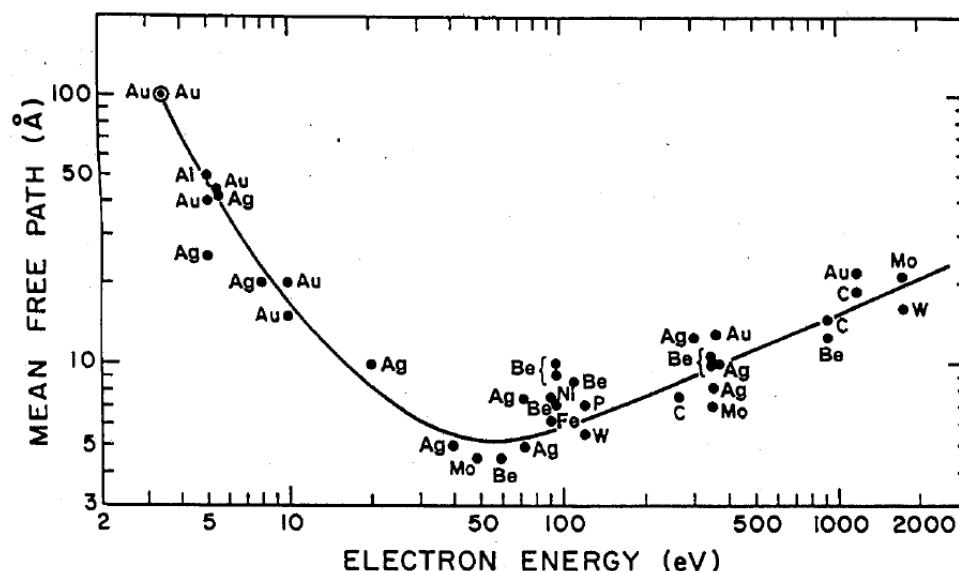


Figure 2.2 Universal curve plot of electron IMFPs of various elements.³

The photon source should be as nearly monochromatic as possible for good energy analysis. Also considerable power will be applied and it is usually necessary to cool the target so a good conductor of heat is preferred. Because of these reasons, The Al and Mg K α X-ray emissions at 1486.6 eV and 1253.6 eV are favored. By using fixed photon energy, the photoionization cross sections would be different for different core levels which need to be taken into consideration when calculating the atomic density of the material.

A hemispherical analyzer is commonly used in XPS. Electrons of different energies are measured by setting voltages for the lens system and retarded to chosen pass energy. Afterwards they can arrive at the detector slits and eventually the detector itself.

The spread of energies in the photon source, the diameter of the analyzer and the pass energy play a major role in determining the resolution of XPS.

From the binding energy and intensity of a photoelectron peak, the elemental identity, chemical state, and quantity of a detected element can be determined. Variations in the number of valence electrons and types of bonds they form will shift the binding energy accordingly. When oxidation state increases, binding energy increases due to greater attraction of the nucleus to a core electron and vice versa. The intensity of the peak can be represented as: $I = n \cdot f \cdot \sigma \cdot \theta \cdot \gamma \cdot \lambda \cdot A \cdot T$, where n is the number of atoms per cm^3 of analyzed region, f is the X-ray flux ($\text{photon}/\text{cm}^2 \cdot \text{sec}$), σ is the cross section in cm^2 , θ is the angular efficiency factor for the instrument, γ is the probability, λ is the IMFP, A is the area in cm^2 , and T is the detection frequency.

We used the Thermofisher K-Alpha system which uses X-ray source from monochromated Al K- α as anode and generates 1486.7 eV photon. System Base Pressure $<5 \times 10^{-9}$ mbar. It has the capability for analysis of electrically insulating samples, depth profile analysis of samples and angle-resolved XPS. The instrument resolution for a given pass energy is determined by the width of the Ag 3d5/2 peak on a clean Ag surface. The ultimate energy resolution is about 0.5 eV. The binding energy of the Ag 3d5/2 core level is characteristic of the energy calibration of the system.

2.3.2 Ambient Pressure X-ray photoelectron spectroscopy (APXPS)

The investigation of surfaces using XPS at or near relevant pressures is challenging due to insufficient electron IMFP by scattering with gas molecules. The development of ambient-pressure XPS (APXPS) addressed the issue. The attenuation of the photoelectron signal in a gas environment is proportional to

$\exp(-z\sigma p/kT)$, where σ is the electron scattering cross section, z is the distance that electrons can

travel through at the pressure p . To get enough electron signals arriving the detector, the path length of the electrons through a gas can be minimized by introducing the differential pump systems.⁴ The sample surface is placed close to a sequence of apertures (usually two to three apertures) that are differentially-pumped. Behind each aperture, the pressure drops by several orders of magnitude before reaching the analyzer while the ambient pressure maintains at the sample surface. The x-ray source is usually separated from the ambient pressure region by the x-ray transparent windows like the 100 nm thick silicon nitride membranes that are used in our experiment.

APXPS and XAS in this study were performed using beamline 13-2 at the Stanford Synchrotron Radiation Lightsource (SSRL). The end station features a vacuum chamber with a differentially pumped electron spectrometer (VG-Scienta, SES-100) connected to an ambient-pressure gas cell, which allows APXPS to be performed for pressures up to approximately 10 Torr.⁵ Samples are loaded into the ambient-pressure gas cell which was then pumped for ~8 hrs to UHV. The ambient-pressure gas cell was connected to a gas manifold containing an ultra-high purity O₂ lecture bottle (99.999% Purity Research Grade, Airgas). A variable leak valve (Vacuum Generators), was used to introduce and control the O₂ pressure in the ambient-pressure gas cell. A residual gas analyzer (RGA200, Stanford Research Systems) was used to collect a background mass scan in order to ensure the O₂ purity for experiments. The distance between the sample

and the beamline window was 10 mm. The beamline has an energy range of $h\nu = 180\text{-}1450$ eV with a resolving energy of $E/\Delta E > 5000$.⁶ The beamline uses a spherical grating monochromator along with Kirkpatrick-Baez focusing mirrors to obtain a spot size of 0.01×0.075 mm² and a flux between $10^{11}\text{-}10^{12}$ photons/second.⁶ For APXPS and XAS experiments, we used $h\nu = 472\text{-}640$ eV and a 600 l/mm Ni coated grating.

2.4 Ultraviolet photoelectron spectroscopy (UPS)

The first range is provided by light from gas discharge sources and particularly the intense line emission from helium (He) and other inert gases: for He, the two main lines have photon energies of 21.2 and 40.8 eV. At these low energies, only valence band electrons from molecular orbitals can be detected.

The spectra usually plot the initial state energy, $E - h\nu + \phi$, where E is the measured photoelectron kinetic energy and ϕ the work function. The maximum energies all line up at the Fermi energy, while the main elastic emission is confined to a small energy spread below this energy. Many of the molecular orbitals from which valence band photoelectron signal originates possess a high degree of hybridization, therefore the shifts in peak binding energy are far more varied and subtle than those observed for core level photoemission peaks. For this reason, valence band spectra are predominantly used for material characterization through spectral fingerprinting,

2.5 Rutherford backscattering Spectrometry (RBS)

Rutherford backscattering can be generally described as an elastic, hard-sphere collision between a high kinetic energy particle from a collimated beam incident beam (the projectile) and a stationary particle located in the sample (the target). The ratio of particle energy before and after the elastic collision with the target can be represented by the equation below:

$$K = \frac{E_1}{E_0} = \left[\frac{(M_2^2 - M_1^2 \sin^2 \theta)^{1/2} + M_1 \cos \theta}{M_2 + M_1} \right]^2$$

Where M_1 and M_2 are mass of the projectile and the target, θ is the backscattering angle from the original trajectory. For He ions penetrating the targets, the energy loss is primarily from excitation and ionization events in inelastic collisions with atomic electrons. The average energy loss during penetration can be estimated by target stopping power (dE/dx). So the energy loss on inward path $\Delta E_{in} \cong \left. \frac{dE}{dx} \right|_{E_0} \cdot t$; the energy loss in the elastic scattering process $\Delta E_s = (1 - K)(E_0 - \Delta E_{in})$; the energy loss on the outward path $\Delta E_{out} \cong \left. \frac{dE}{dx} \right|_{E_1} \cdot \frac{t}{\cos \theta}$. Then $E_1 = E_0 - \Delta E_{in} - \Delta E_s - \Delta E_{out}$.

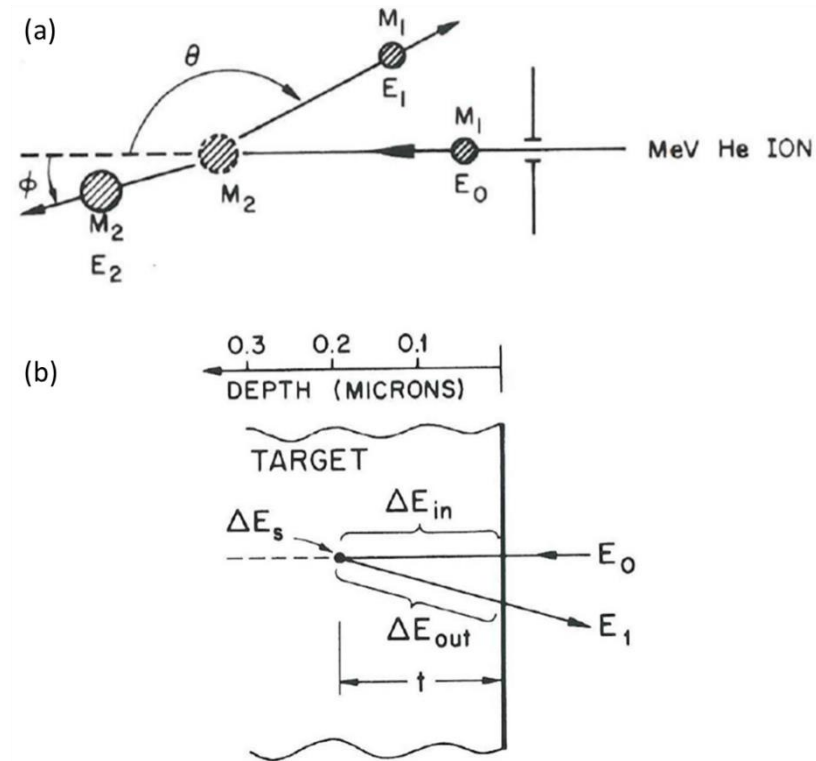


Figure 2.3 (a) Schematic representation of an elastic collision between an incident beam and the target; (b) Energy loss components for a projectile that scatters from depth t .

During the measurement, the detection yield $Y = \sigma(\theta) \cdot \Omega \cdot Q \cdot N\Delta t$, where $\sigma(\theta)$ is the cross section at backscattering angle θ , Ω is the detector solid angle, Q is the measured number of incident particles and $N\Delta t$ is the number of target atoms/cm² in the layer.

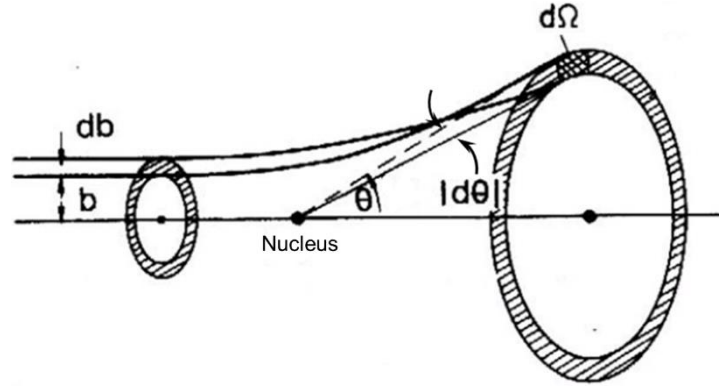


Figure 2.4 Schematic representation of the probability for incident particles being deflected from the target nuclei.

By definition, the cross section is the probability of the particle to be deflected from the target nuclei. So $2\pi b db = -\sigma(\theta) \cdot 2\pi \sin\theta d\theta$, where b is the perpendicular distance between the incident particle path and the parallel line through the target nucleus. The impact parameter b can be calculated from the force during the collision which in most cases is the unscreened Coulomb repulsion of two positively charged nuclei and the equation is as below:

$$b = \frac{Z_1 Z_2 e^2}{2E} \cot \frac{\theta}{2}$$

So the cross section can be expressed as:

$$\sigma(\theta) = \left(\frac{Z_1 Z_2 e^2}{4E} \right)^2 \frac{1}{\sin^4 \theta / 2}$$

The software SIMNRA implements the physical concepts mentioned above. It can be used to simulate the RBS spectra and get the thin film structure quantitatively.

2.6 Helium ion microscope (HIM)

The exceptional spatial resolution of the helium ion microscope (HIM), as commercialized by Carl Zeiss Microscopy, (Peabody, MA), and its outstanding performance for imaging, particularly for insulating samples,^{7, 8} makes it a compelling tool for many scientific areas such as materials research, life sciences, etc.

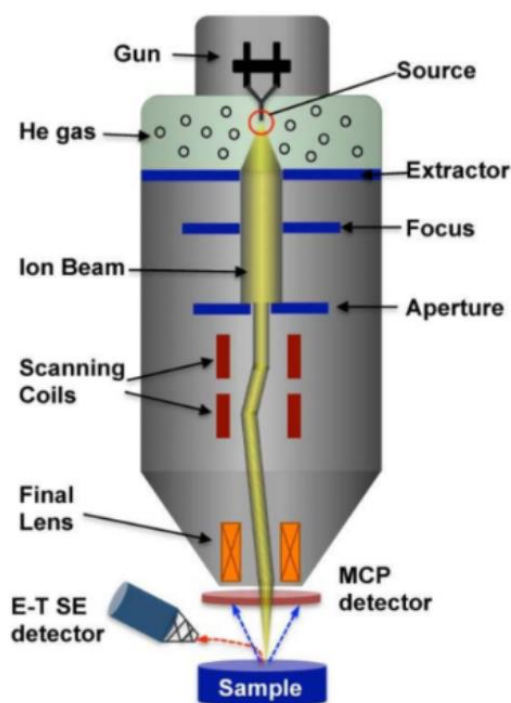


Figure 2.5 Schematic of Carl Zeiss ORION HIM system.⁹

Figure 2.5 shows the schematic of HIM system used in this thesis. The ion source in HIM consists of a very sharp monocrystalline metal needle ending with only three atoms (referred to as a trimer). The three-atom configuration allows greater stability and consequently longer operation times compared to a single atom. The instrument produces He and Ne ions with energies between 15-35

keV with a beam spot of ~ 0.5 nm (at 30 keV He) and a beam convergence angle of about 0.5 mrad, a factor of ten lower than in a typical scanning electron microscope (SEM).¹⁰ The needle is applied with a positive high voltage to generate a very high electric field (~ 4.4 V/Å) at the very sharp area of the trimer resulting in field ionization of the He atoms. The generated helium ions are then accelerated through the axially aligned hole in the extractor electrode. The helium beam is further aligned with apertures of different sizes, focused by lens and rastered on the sample. Once reaching the sample, the incident He ions mainly interact with electrons. Since the He mass is much larger than that of the electron, the ions do not deviate much from the initial trajectory creating significantly small interaction volume than for incident electrons which provides HIM with a good depth of focus. Secondary electrons are generated by the ionization events and some of them are ejected from the sample and then collected by the detector. It has been shown, experimentally and theoretically, that the number of secondary electrons generated from the He beam is significantly higher than generated by an SEM beam.¹¹ Amongst other factors, the angle of escaped secondary electrons determines its chance to reach the detector and further produce the imaging contrast. Combined with Less multiple scattering events than SEM, HIM can generate remarkable morphological images of surface with exceptionally clear images of complex 3D structures and much better resolution.

Reference

1. Nečas, D.; Klapetek, P., Gwyddion: an open-source software for SPM data analysis. *Open Physics* **2012**, 10 (1), 181-188.
2. Chusuei, C. C.; Goodman, D. W. J. E. o. p. s.; technology, X-ray photoelectron spectroscopy. **2002**, 17, 921-938.
3. Somorjai, G. A., *Chemistry in two dimensions: surfaces*. Cornell University Press: 1981.
4. Yamamoto, S.; Bluhm, H.; Andersson, K.; Ketteler, G.; Ogasawara, H.; Salmeron, M.; Nilsson, A., In situ x-ray photoelectron spectroscopy studies of water on metals and oxides at ambient conditions. *Journal of Physics: Condensed Matter* **2008**, 20 (18), 184025.
5. Kaya, S.; Ogasawara, H.; Näslund, L.-Å.; Forsell, J.-O.; Casalongue, H. S.; Miller, D. J.; Nilsson, A., Ambient-pressure photoelectron spectroscopy for heterogeneous catalysis and electrochemistry. *Catalysis today* **2013**, 205, 101-105.
6. Shiobara, E.; Mikami, S.; Yamada, K. In *Recent status of resist outgas testing for metal containing resists at EIDEC*, Extreme Ultraviolet (EUV) Lithography IX, International Society for Optics and Photonics: 2018; p 105830B.
7. Hill, R. R., FHM Faridur, Advances in helium ion microscopy. *Nuclear Instruments Methods in Physics Research Section A: Accelerators, Spectrometers, Detectors Associated Equipment* **2011**, 645 (1), 96-101.
8. Ward BW, N. J. A., Economou NP, Helium ion microscope: A new tool for nanoscale microscopy and metrology. *Journal of Vacuum Science Technology B: Microelectronics Nanometer Structures Processing, Measurement, Phenomena* **2006**, 24 (6), 2871-2874.
9. Bell, D. C.; Lemme, M. C.; Stern, L. A.; Williams, J. R.; Marcus, C. M. J. N., Precision cutting and patterning of graphene with helium ions. **2009**, 20 (45), 455301.
10. Hlawacek, G.; Götzhäuser, A., *Helium Ion Microscopy*. Springer: 2016.
11. Joy, D. C., *Helium Ion Microscopy: Principles and Applications*. Springer: 2013.

Chapter 3: The development of organotin resists and their radiation chemistry

3.1 Introduction

As noted above, our collaborators in the NSF Center for Sustainable materials Chemistry (CSMC), based at Oregon State University helped lead a multi-university program to develop new inorganic-based resist chemistries and processes. We examined a series of Sn-based precursors due in part to the high EUV absorption cross section of tin. Below I list three main clusters I examined, all in collaboration with our CSMC colleagues: $[(\text{BuSn})_{12}\text{O}_{14}(\text{OH})_6](\text{OH})_2$ (the “football” precursor), a commercial n-butyltin oxide hydroxide, n-BuSnOOH (“commercial” precursor), and a sodium-centered β -Keggin structure, $\text{NaO}_4(\text{BuSn})_{12}(\text{OH})_3(\text{O})_9(\text{OCH}_3)_{12}(\text{Sn}(\text{H}_2\text{O})_2)]$ (β - NaSn_{13} , “ β -keggin” precursor).^{1, 2} Films were deposited by spin-coating, and conditions such as the choice of solvent and concentration of precursor solution were optimized in order to achieve as flat and uniform a film as possible.

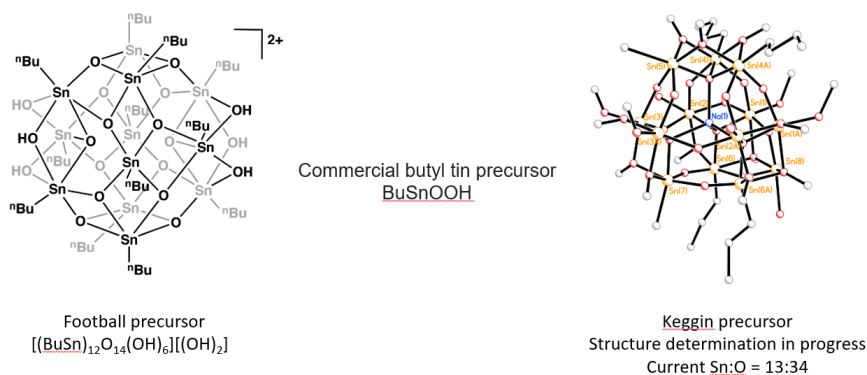


Figure 3.1 Three precursors in progress.

To understand the radiation chemistry, we used different radiation sources to explore the changes that occur in films before and after exposure (and processing). Unfortunately, the cost of a current generation EUV source is approximately \$100M USD, so exposure under realistic conditions was not practical for everyday studies. Instead we explored using other sources of photons, ions and electrons, as proxies for the 92eV photon of current EUV sources. XPS was used to monitor chemical bonding changes under photon exposure (although the x-ray energy used was over 10 times higher than the EUV photon energy). Ultraviolet light from a UPS source was also used due to its lower photon energy, about a quarter of the energy of EUV photons, so that it could serve as a good comparison. Ambient pressure XPS was used to explore possible effects of gas phase species present during realistic manufacturing processes. Eventually a radiation mechanism was proposed to explain the behavior of EUV photoresist candidates under photon exposure.

3.2 Cluster to thin film

We purified a series of different resist precursors and optimized their spin coating conditions to obtain low roughness and uniform films. As-deposited film chemical composition was determined to help understand the differences between the different clusters and to further elucidate possible radiation chemistry that was occurred upon exposure. The Keggin precursor was able to generate uniform films most easily in our work (see below) and we knew its chemical structure and best purification processes. As a result, we eventually chose the Keggin precursor for further analysis.

3.2.1 Thin film uniformity

Early in our studies we used AFM to compare the uniformity of films of three different precursors shown in

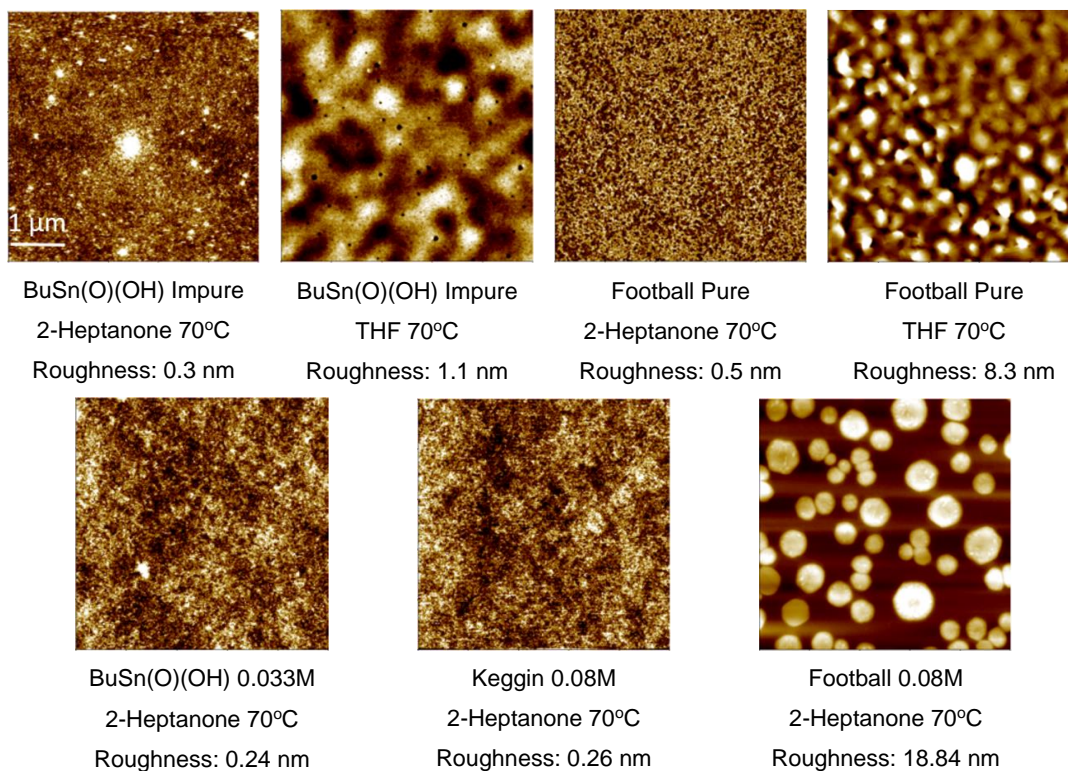


Figure 3.2. Solvents explored included 2-heptanone and THF. Both commercial and football precursor films have relatively low roughness using the 2-heptanone as the solvent. When deposited using higher concentration solutions, the football precursor film shows large features (and roughness) on the surface, possibly crystalline.

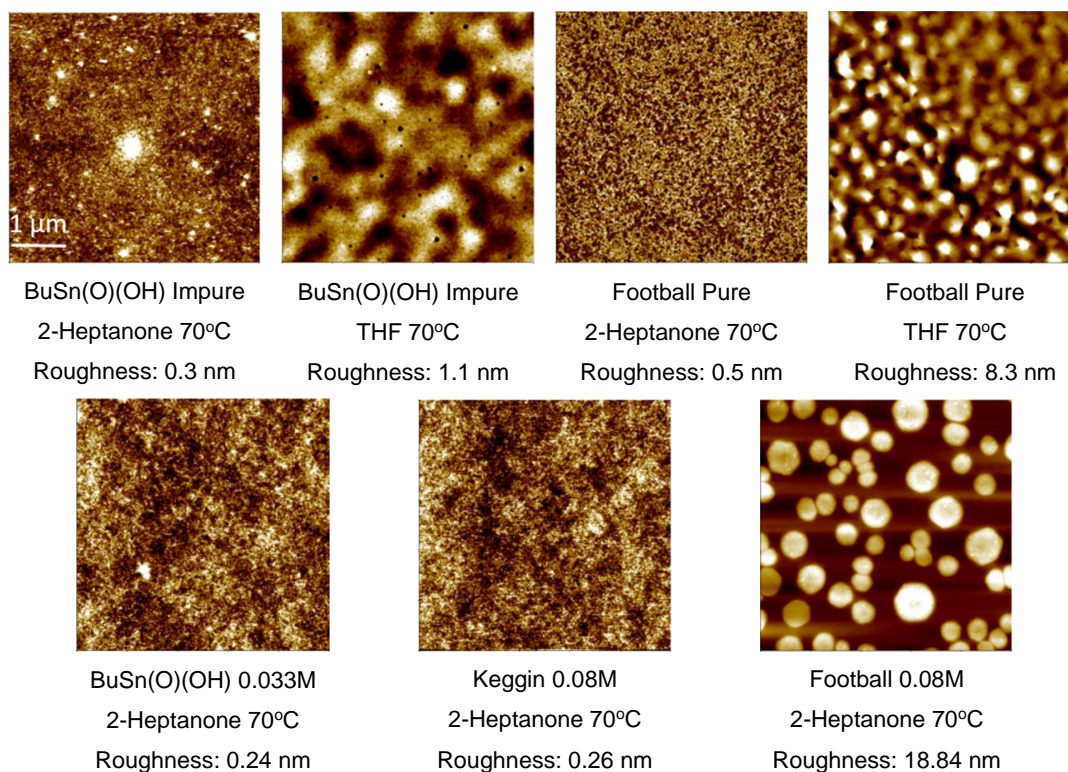


Figure 3.2 AFM images and measured roughness of tin-based precursor with different solvents and concentrations.

Based on the topographic AFM images, the concentration of precursor solutions showed a larger effect on thickness than the spin-coating uniformity. Thus, we can have control of the thickness at some level by changing the precursor concentration.

Recrystallization of the precursors can produce more pure clusters, so we compared keggin precursor film structure follow different numbers of recrystallization cycles. AFM was used to compare the uniformity for: once recrystallized on 70nm SiO₂, once recrystallized on 100nm SiO₂ and twice recrystallized on 100nm SiO₂. All of them showed similar roughness. Thus the recrystallization purification process did not affect Keggin cluster film uniformity.

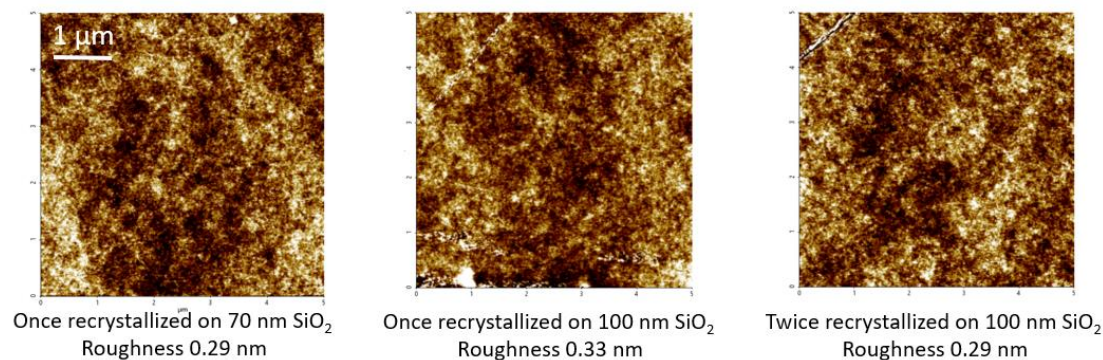


Figure 3.3 AFM images of films prepared under different conditions.

The thickness of each film was measured by ellipsometry and AFM step height. The results are consistent between these two methods. The football film structure showed a big variation in AFM step height measurements; I believe that this is most likely because of the generation of larger cluster crystallites, leading to a rougher surface. Both commercial and keggin film showed similar thickness of ~20 nm with small variation.

Table 3.1 Film thickness of [(BuSn)₁₂O₁₄(OH)₆][OH]₂ compound, commercial BuSnOOH and keggin Sn13 compound: Ellipsometry thickness & AFM thickness

Sample	Ellipsometry – Cauchy-modeled	AFM –Step-Height
	Thickness (nm)	Thickness (nm)
Football	27.3 ± 0.3	30 ± 10
Commercial	18.6 ± 0.2	17 ± 2
Keggin	23.00 ± 0.4	20 ± 2

RBS was used to further analyze film thickness and uniformity. Because the football film was very rough, it won't give a reliable result from RBS. We just measure the commercial and keggin film as in Figure 3.4. The signals from light

elements like carbon and oxygen are lost in the silicon substrate background yield and thus hard to determine quantitatively. We used the Sn density and known (from other studies) composition and phase to estimate the film thickness.

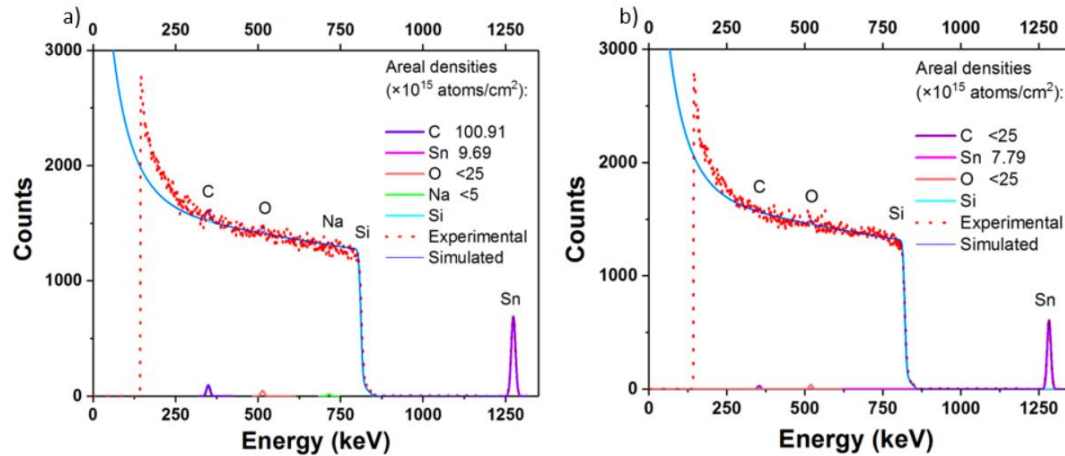


Figure 3.4 RBS spectra of a) Keggin film on HF etched silicon substrate and b) Commercial film on native oxide silicon substrate.

The radius of a cluster is 5 Å, the distance between clusters is 11 Å, and the number of nearest neighbors to a cluster is 0.53.¹ So one molecule in the solution would occupy roughly $\frac{4}{3}\pi(1.1)^3/(1 + 0.53) = 3.64 \text{ nm}^3$. There are thirteen Sn atoms per molecule. So the volume density of the clusters in solutions would be $13/3.64 \times 10^{21} = 3.57 \text{ atom/cm}^3$. The solvent is removed during soft bake and pump down in the RBS system prior the measurement, so films become thinner and denser than solutions. Thus the volume density of the clusters in films would

be more than 3.57 atom/cm^3 . In this case, the maximum thickness of Keggin film

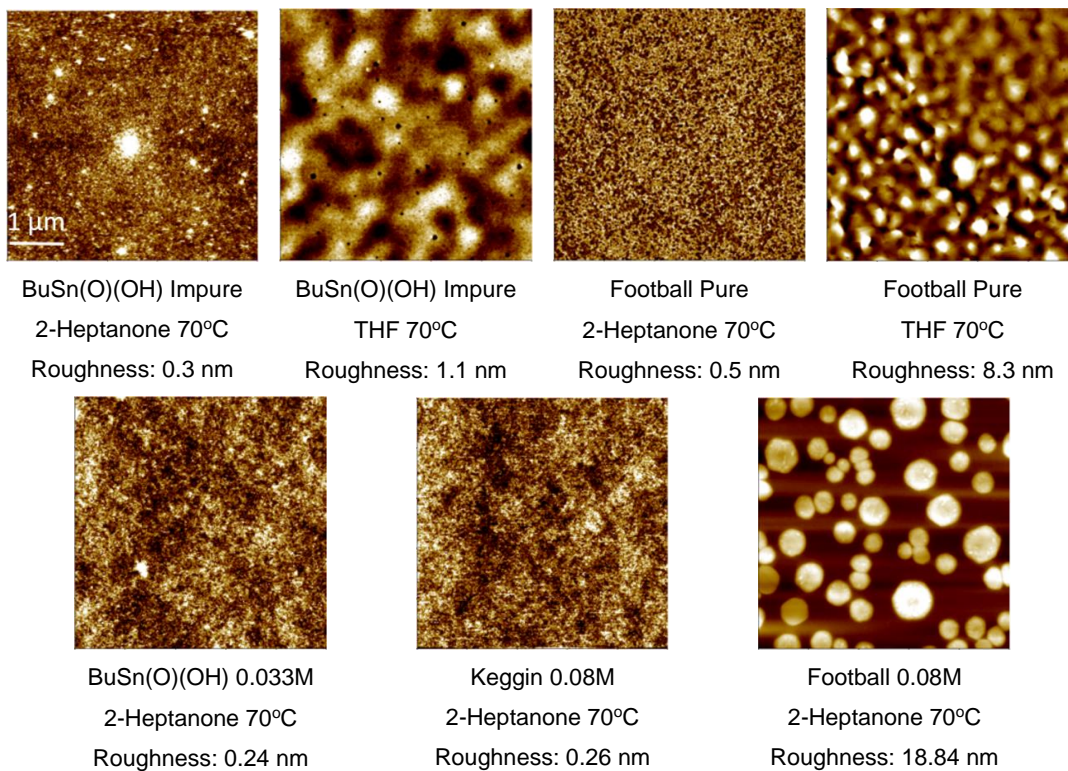


Figure 3.2) that we prepared is $9.69 \times 10^{15} / 3.57 \times 10^{21} = 27.1 \text{ nm}$. Because Keggin clusters are recrystallized from the commercial clusters, we assume in solution

they are sharing similar density. So the maximum thickness of commercial film

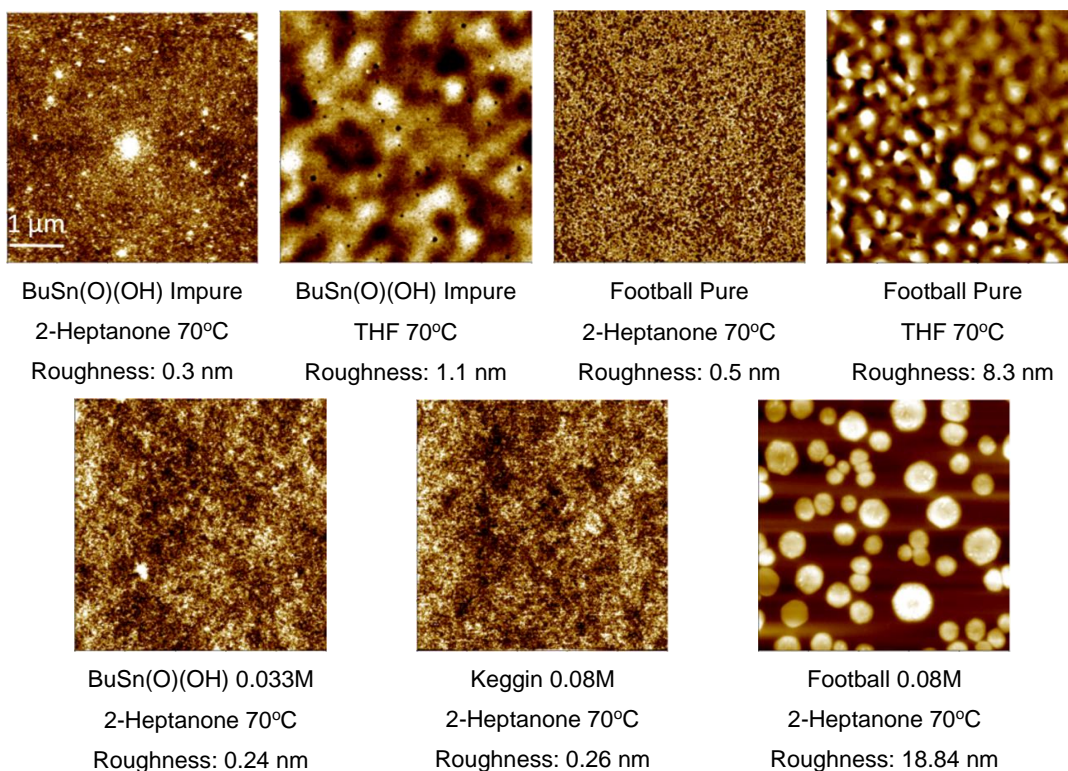


Figure 3.2) that we prepared was $7.79 \times 10^{15} / 3.57 \times 10^{21} = 21.8$ nm which was slightly thinner than Keggin film. In general, the thickness from RBS was consistent with the Ellipsometry and AFM step height measurements.

We also estimated the uniformity in the z direction using grazing-angle RBS as shown in Figure 3.6. We focused on the tin peak and used SIMNRA simulations of different models to fit the spectra. We changed the position of the detector to obtain data for an 80° exit angle.

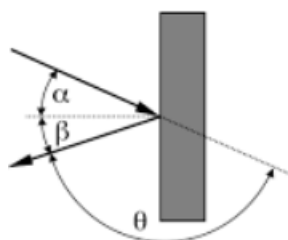


Figure 3.5 Scattering geometry of RBS with α as the incident angle, β as the exit angle and θ as the scattering angle.

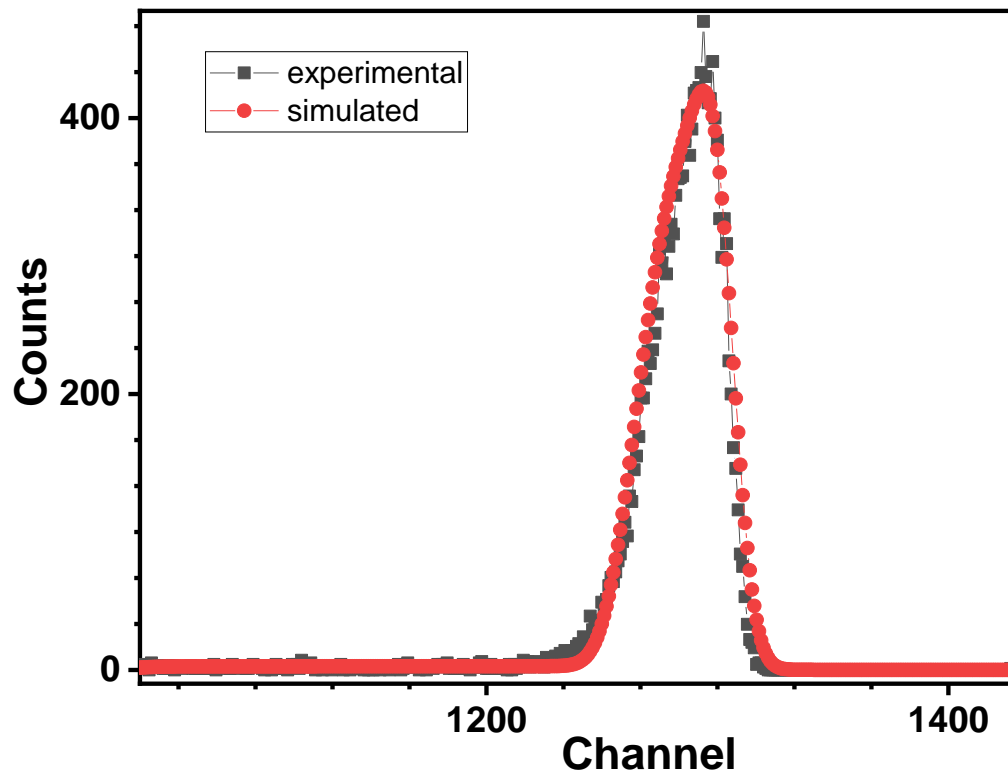


Figure 3.6 Grazing-angle RBS for keggin film on silicon. Black curve is the smoothed RBS data and red curve is simulated data.

By changing the roughness of the film we could not obtain a good agreement between the simulated and raw data. We added an extra layer of pure SnO_2 ($\text{Sn}:\text{O}=0.34:0.66$) at surface and changed the thickness to get a more reasonable fitting, as shown in Figure 3.6. This three-layer model contained $15\text{e}15$ atoms/ cm^2 of SnO_2 and $350\text{e}15$ atoms/ cm^2 of the keggin film on the silicon substrate. This simulation was based on admittedly strange conditions, but its

consistency with the data gives us a hint about the possible existence of high Sn-density layer at the film surface.

3.2.2 As-deposited film chemical component

We also used XPS to investigate the chemical bonding and elemental components at the film surface. Because organic carbon species have similar binding energy, we just use one single C peak to fit the C data and to obtain the total atomic percentage of C for comparison. Further analysis of the carbon bonding environment was done using FT-IR, TPD and TOF-SIMS by our collaborators.³ Based on their results, the film has C-H and C-O bonds which is consistent with the cluster structure. According to the oxygen XPS region, we show the O 1s spectra fit well with two peaks at $E_b = 530.5$ and 532.0 eV. These binding energies correspond to O in tin oxide and either methoxy or hydroxyl ligands, respectively.⁴⁻⁷ Adsorbed organic carbonates and water are also expected as contaminants. Unfortunately, the binding energies of these potential contaminants are similar to the values expected for methoxy or hydroxyl ligands, which makes it difficult to quantify the amount of contaminants.⁸ Therefore, in the discussions below the O 1s components will be primarily identified as tin oxide ($E_b = 530.5$ eV, O-Sn) and methoxy/hydroxyls ($E_b = 532.0$ eV, O-C/O-H).

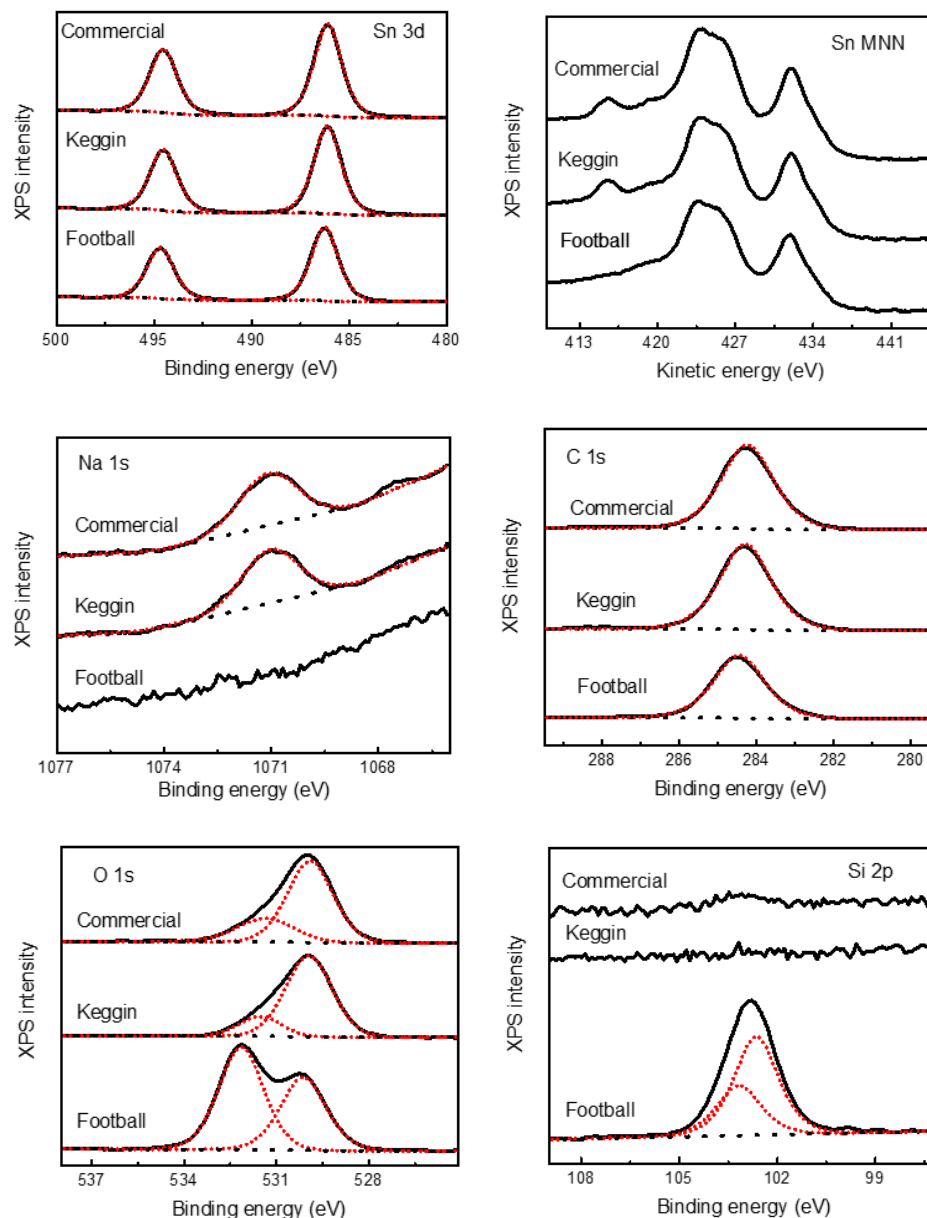


Figure 3.7. Sn 3d, Sn MNN, Na 1s, C 1s, O 1s, and Si 2p XPS spectra of commercial, kegginn and football Sn precursor films.

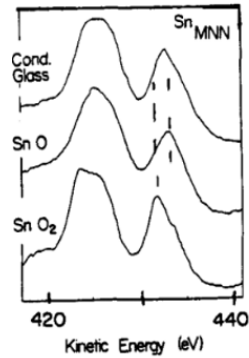
Based on our XPS results, there could be Na and Si at the surface in addition to the elements that form the precursors (Sn, C, O and H). As to the Na 1s XPS region, there is a clear peak at around 1071 eV for films of both commercial and kegginn compounds while nothing can be observed for the film deposited using

the football compound. Also the peak loss at around 415 eV (kinetic energy) of the Sn MNN region for the football film is just the Na 1s peak. The sodium should come from the impurities in commercial precursors and cannot be removed after recrystallization.¹ Only the synthesized football compound doesn't have sodium in the structure.

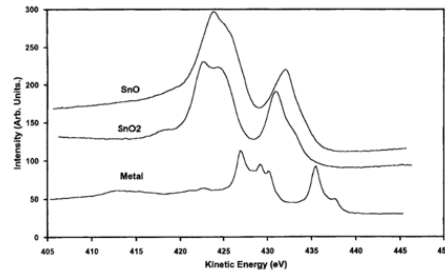
To further investigate the bonds that exist in our films, we examined the oxygen region. As to commercial and keggin films, the deconvolution of the peaks leads us to assume that we have Sn-O-Sn (~530.1 eV) type structures, combined with Sn-O species (486.31 eV) shown in the tin XPS region (Figure 3.7).⁹ The peak around 531.6 eV refers to C-O type structures.¹⁰ On the other hand, the football film shows an extra peak at higher binding energy (532.5 eV) which should come from native silicon oxide at the interface.¹¹ The silicon 2p region for the football structure generated film supports this by showing an obvious peak while the commercial and Keggin films do not show this behavior. The Si peak might result from photoemission yield from uncovered areas due to island/cluster formation as shown in the AFM images.

We show the Sn 3d spectra fit to two peaks at $E_b = 486.6$ and 495.0 eV, which correspond to Sn $3d_{5/2}$ and $3d_{3/2}$ spin-orbit split doublet. These binding energies are consistent with either Sn^{2+} or Sn^{4+} . Unfortunately, these two different common Sn oxidation states don't demonstrate much variation in their Sn3d peak positions. Thus we also looked at Sn Auger peaks using XPS, taking the commercial compound as an example. The Sn ($3d\ 5/2$, 486.31 eV) spectra indicates oxidized Sn species. The Sn $M_4N_{4,5}N_{4,5}$ peak was found at 432 eV (in

kinetic energy) and the shape of the spectrum agrees well with the reported Sn^{4+} species. The general shape of the Auger spectrum is quite similar to the reference one, as shown. The Sn $M_4N_{4,5}N_{4,5}$ Auger peak appears at lower kinetic energy than the SnO one.



(a)

Figure 4. Experimental Sn MNN Auger spectra for Sn, SnO and SnO_2 , respectively.

(b)

Figure 3.8 (a) The Sn MNN Auger peaks of SnO, SnO_2 and the conducting glass are shown.¹² b. Experimental Sn MNN Auger spectra for Sn, SnO and SnO_2 , respectively.¹³

We can apply a simple model to estimate the Auger parameter by the equation as shown below: ¹³

$$\alpha' = E_b(3d_{5/2}) + E_{kin}(M_4N_{4,5}N_{4,5})$$

Where $E_b(3d_{5/2})$ is the binding energy of Sn $3d_{5/2}$ and $E_{kin}(M_4N_{4,5}N_{4,5})$ is the kinetic energy of Sn $M_4N_{4,5}N_{4,5}$. The calculated Sn Auger parameter, 918.31 eV, falls into the range of Sn^{4+} species (918.3 eV-919.0 eV) and is significantly less than that of Sn^{2+} at 919.7 eV. Based on these two evidence, we conclude that Sn^{4+} species are in the film structure.

Table 3.2 Sn Auger parameter calculation for three films prepared from football, commercial, and kegging-based solutions.

	Sn auger kinetic energy (eV)	Sn 3d5/2 binding energy (eV)	Sn Auger Parameter (eV)
Football compound	431.9	486.46	918.36
Commercial compound	432	486.31	918.31
Keggin compound	432	486.29	918.29

We compared the tin and oxygen binding energies among all films prepared with different precursors in Table 3.3. They show the good consistency of the Sn3d5 region which tells us that the Sn likely exists in similar bonding configurations within all these films and its chemical state should be Sn^{4+} . Only the film that results from the football precursor has an extra higher binding energy oxygen peak. Since we can also observe silicon peak from the substrate, we believe that this higher energy peak results from native silicon oxide emission from the surface/interface.

Table 3.3 XPS binding energy (eV) comparison among films

	Commercial	<u>Keggin</u>	Football
Sn3d5 Scan A	486.31	486.29	486.46
O1s Scan A	530.1	530.16	530.27
O1s Scan B	531.57	531.78	531.47
O1s Scan C			532.47

We next calculated the elemental atomic percent ratio based on XPS intensity. For commercial and keggin films, the O:Sn ratio was less than 1.5 which is not consistent with the known atomic ratio (about 2) which suggested that film composition (and/or structure) may have be different from what is in the precursor. After spin-coating, there might be some cross-linking already due to the loss of the solvent which creates an extra dense layer at surface. This result are consistent with the model we obtained from RBS grazing-angle measurements.

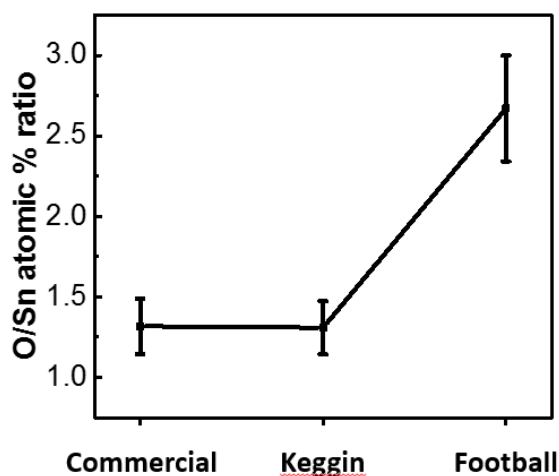


Figure 3.9 Atomic percent ratio of oxygen to tin for three precursor films.

3.3 Radiation chemistry

3.3.1 X-ray exposure

Radiation chemistry investigation by in situ XPS measurement before and after 1 hour X-ray (Al 1486.7 eV) exposure.

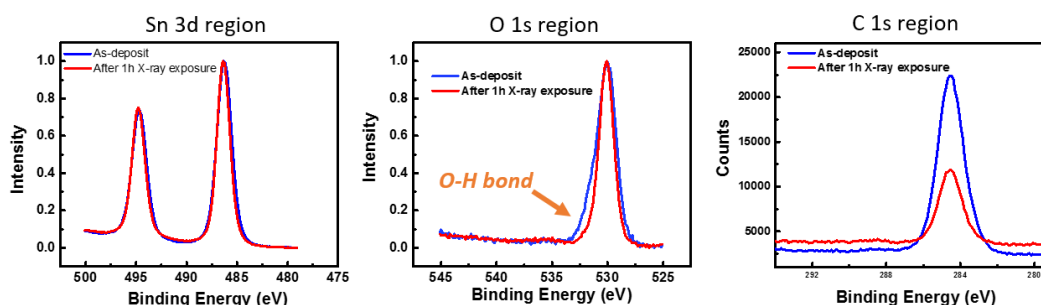


Figure 3.10 In situ XPS data comparison before and after exposure

Upon examining the Sn3d5 peak region, the as-deposit film doesn't change upon x-ray exposure. On the other hand, from the oxygen region, we observe an obvious decrease of the higher binding energy peak (531 eV) which correspond with the O-H bond. Also the butyl group which contains carbon may be lost during exposure.



Figure 3.11 XPS comparisons for exposed/unexposed areas are measured on the same sample after development. Grey spots on each sample are exposed

areas and resist films remain on the surface. Blue areas are unexposed which show thick SiO_2 color of the substrate.

We found that a solubility change occurred upon developing the $\beta\text{-NaSn}_{13}$ after extended X-ray exposures used to collect the data in Figure 3.10 (note that the X-ray exposures are performed in UHV). It is likely that sufficient X-ray flux was provided to cause radiation induced changes rapidly in the films, which ultimately results in the formation of an insoluble product.

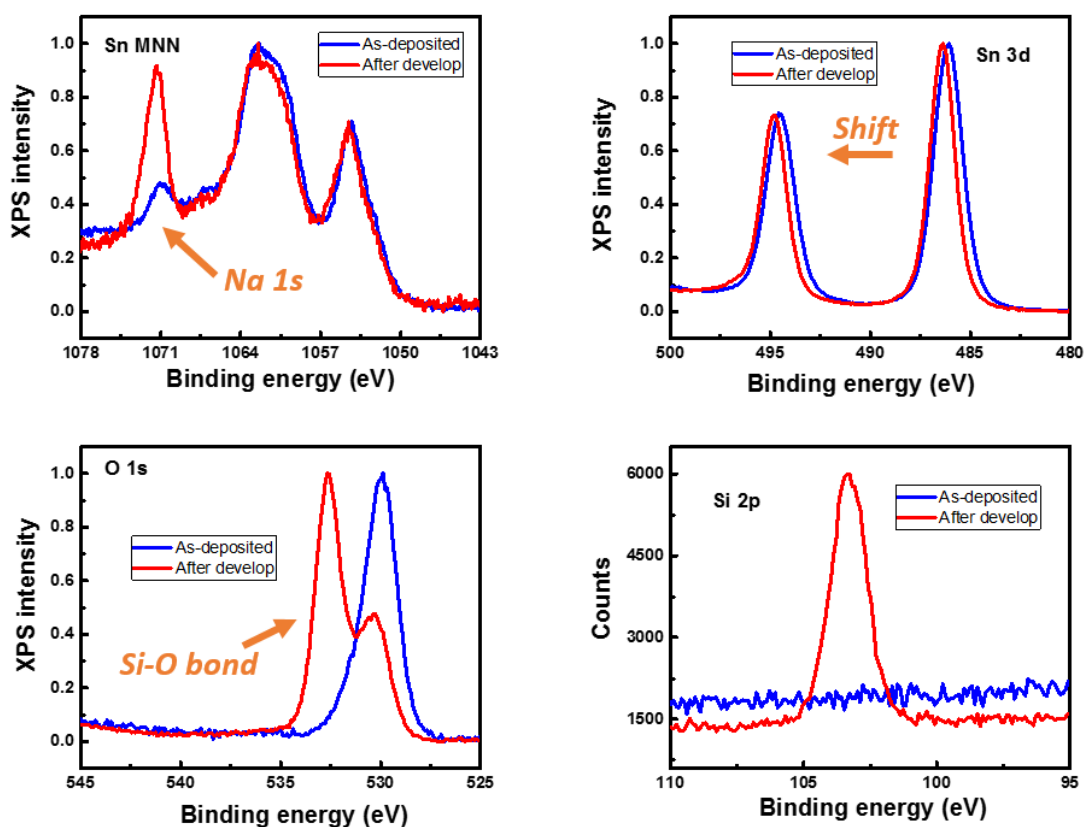


Figure 3.12 XPS data comparison before and after development

From the Sn MNN Auger region of the spectra, we can observe that the ratio of Na:Sn increased after development. This indicates that after this whole process,

sodium loss is less than tin loss, although we would prefer that the change would be the in the opposite direction. We need to remove the sodium by optimizing the precursor or changing the precursor preparation procedure.

The Sn 3d photoemission peak shifted a little to higher binding energy implying more electro-withdrawing species bonding to tin. This is consistent with the C-O bond loss during exposure. Oxygen with binding energy about 532.5 eV can be observed which refers to the SiO₂ bond. This might be due to the film thickness shrinkage after development. Even some of the film thickness remained, the photon flux of the XPS is still not enough to uniformly switch the solubility of the entire film.

We also compared the quantity changes of each component as shown below.

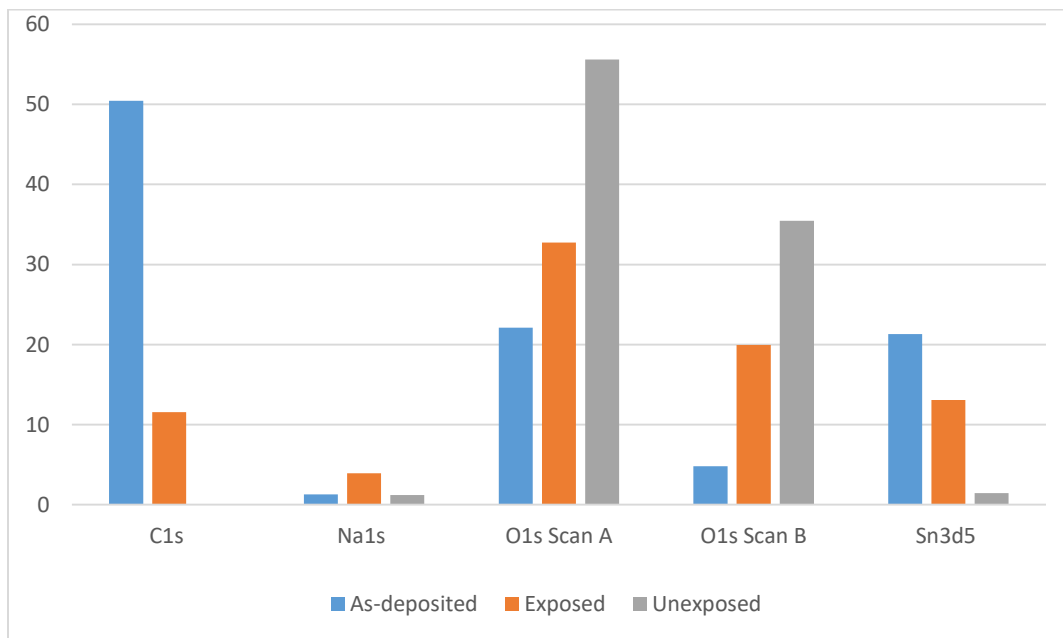


Figure 3.13 Atomic percentage comparison before and after development

The carbon photoemission peak disappears completely in the unexposed area after development; this means that the develop time is sufficient. However, some metal oxide residue remains. This could be due to the very high sensitivity of the film or strong bonding between the film and the substrate. Further analysis is presented in the next chapter.

3.3.2 UV exposure

The valence band electronic structure helps provide additional information about film chemical composition and structure. The results can be used to support different models of surface chemistry. Valence orbitals have cross-sections that are strongly dependent on photon energy. In our system, oxygen-based orbitals dominate the UPS valence band spectra while tin ones dominate the XPS valence band spectra. By comparing differences between XPS and UPS valence band spectra, additional evidence about structure can be determined. With the UPS photon source (in Figure 3.14 we just showed the He 2 α which is the energy of our interest), the cross section of the photons with the oxygen 2p orbital is about 100 times higher than with the tin 5s orbital. However with the XPS photon source (Al K α 1486 eV), the situation becomes the opposite.

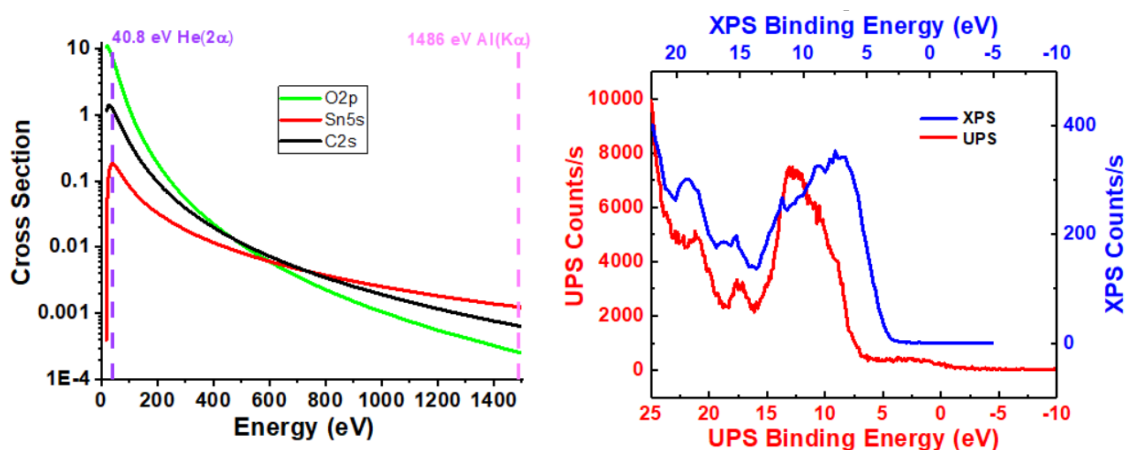


Figure 3.14 (a) Atomic calculation of photoionization cross-sections. (b) UPS and XPS valence band structure.

Our XPS valence spectra has some features showing a SnO₂-like structure. This result supports our suggestion that the final product would have clusters connected by a Sn-O-Sn framework.

We used a UPS photon source (predominantly He 2α 40.8eV) as one proxy to mimic the irradiation conditions under realistic EUV exposure (92eV photons). In Figure 3.15, the difference spectral changes imply that the film becomes oxidized with increasing photon exposure. No structure that resembles Stannoxane, which has similar bonds to our precursor but has 5-coordinated Sn, is apparent. This confirm that the valence band structure is highly dependent on electron configuration.

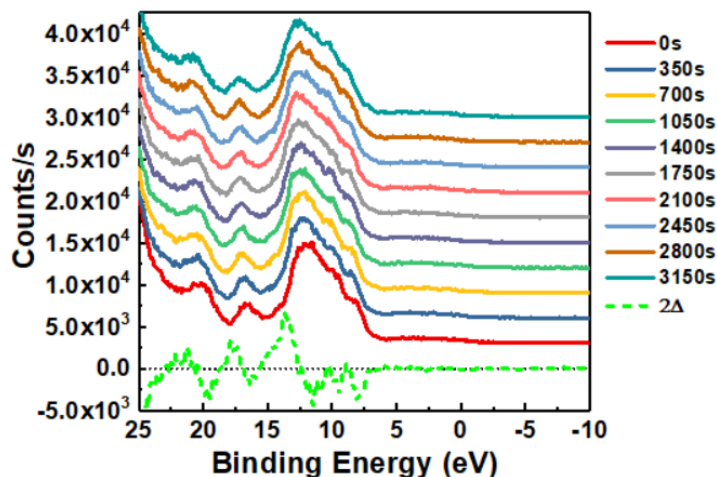


Figure 3.15 UPS valence band measurement on Keggin film with different exposing time.

3.3.3 Ambient pressure XPS (APXPS)¹⁴

To further evaluate radiation-induced chemistries we have obtained APXPS data for $h\nu = 472, 510, 530,$ and 626 eV and for UHV, $P_{O_2} = 0.01$, and $P_{O_2} = 1$ Torr. The goal of adding oxygen during exposure is to determine if oxygen absorbed in the film can result upon radiation exposure in the formation of reactive oxygen intermediates that can increase the rate of butyl ligand loss from the resists.^{15, 16} Based on mechanisms where the loss of the butyl group is necessary to form an insoluble film, the incorporation of oxygen may potentially increase the sensitivity of the EUV photoresists.¹⁷ We also consider the role that the total electron yield (TEY) has on the radiation chemistries in the β -NaSn₁₃ films. For the four photon energies used in the APXPS experiments, we can evaluate the TEY and the primary atomic origin of the electrons. At $h\nu = 472$ eV, which is below both the Sn M_{4,5} and O K edges, we have the lowest total absorption leading to a low TEY. At $h\nu = 510$ eV, which is just above the Sn M_{4,5} edge, we have increased the TEY.

At $h\nu = 530$ eV, which is on the O K edge, we have further increased the TEY. At $h\nu = 626$ eV, which is above both the Sn M_{4,5} and O K edges, we have the highest TEY. Compared to the TEY at $h\nu = 472$ eV we find that the TEY for $h\nu = 510, 530$, and 626 eV increase by factors of 1.6, 2.1, and 3.5, respectively.

In Figure 3.16 (a-c) we show C 1s, O 1s, and Sn 3d spectra, respectively, obtained at $h\nu = 626$ eV in UHV and $P_{O_2} = 1$ Torr. The spectra are stacked for clarity and are normalized using the procedure described above. The signal to noise ratio in the spectra decreases with increasing O₂ pressure due to the additional inelastic attenuation of electrons at higher gas pressures.

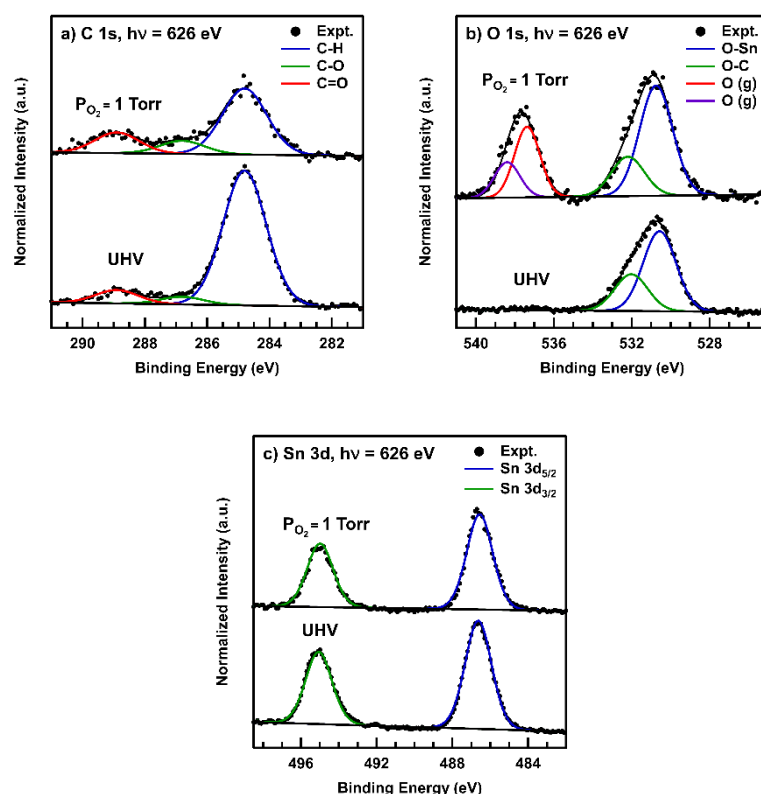


Figure 3.16 APXPS obtained for β -NaSn₁₃ in both UHV and $P_{O_2} = 1$ Torr using $h\nu = 626$ eV. (a) C 1s, (b) O 1s, and (c) Sn 3d core levels.

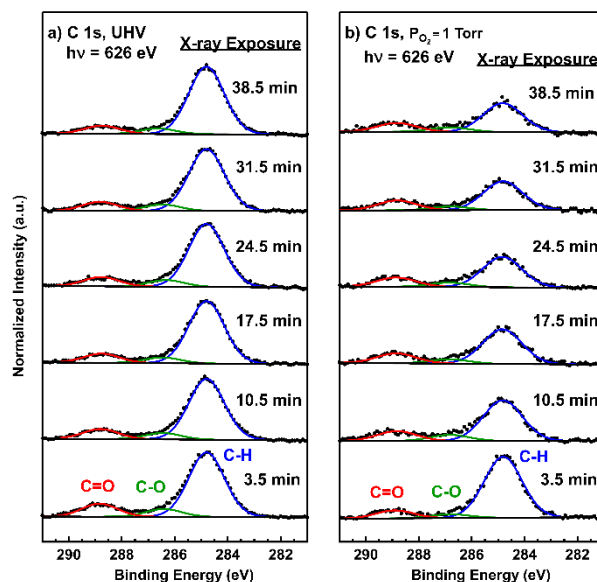
In Figure 3.16 (a) we show the C 1s spectra fit with three peaks at $E_b = 284.8$, 286.8, and 288.9 eV. These binding energies correspond to C-H, C-O, and C=O, respectively.¹⁸ The most intense peaks at $E_b = 284.8$ and 286.8 eV can be correlated to the twelve butyl and methoxy ligands, respectively, that are coordinated to the β -NaSn₁₃ cluster. The peak at $E_b = 288.9$ eV is likely due to contamination from exposure to the atmosphere.

In Figure 3.16 (b), we show the O 1s spectra fit with two peaks which correspond to tin oxide and either methoxy or hydroxyl ligands, respectively, as we discussed before. The O 1s spectra obtained at $P_{O_2} = 1$ Torr also has peaks at $E_b = 537.8$ and 538.8 eV which correspond to the gas phase O₂ doublet.

In Figure 3.16 (c), we show the Sn 3d spectra fit to two peaks which correspond to the Sn 3d_{5/2} and 3d_{3/2} spin-orbit split doublet; the spectrum is consistent with the molecular formula and structure of the β -NaSn₁₃ cluster.

To assess changes in the β -NaSn₁₃ films under different ambient conditions, following increasing exposure times, and for different photon energies, we have fit the C 1s and O 1s spectra using the procedure described above. Figure 3.17 shows APXPS spectra obtained with $h\nu = 626$ eV. Figure 3.17 (a,b) show the C 1s spectra obtained at UHV and $P_{O_2} = 1$ Torr, respectively, while Figure 3.17 (c,d) show the O 1s spectra obtained at UHV and $P_{O_2} = 1$ Torr, respectively. The X-ray exposure time is indicted in the figures and corresponds to the time at the midpoint of the spectrum. The C1s and O 1s spectra labeled 3.5 and 4.5 minutes, respectively, were obtained immediately after the sample was moved to

a new location. The other spectra were obtained at the indicated times. We found that the C 1s spectra obtained in UHV (Figure 3.17a) do not change significantly even after a 38.5 min radiation exposure. However, the C 1s spectra obtained in $P_{O_2} = 1$ Torr (Figure 3.17b) significantly decreased in intensity for the C-H component, while the C-O and C=O components stayed approximately the same as the initial spectrum. As shown in Figure 3.17 (c,d), only minor changes were observed for the O 1s spectra whether the data were obtained in UHV or under a pressure of $P_{O_2} = 1$ Torr or for longer exposure times.



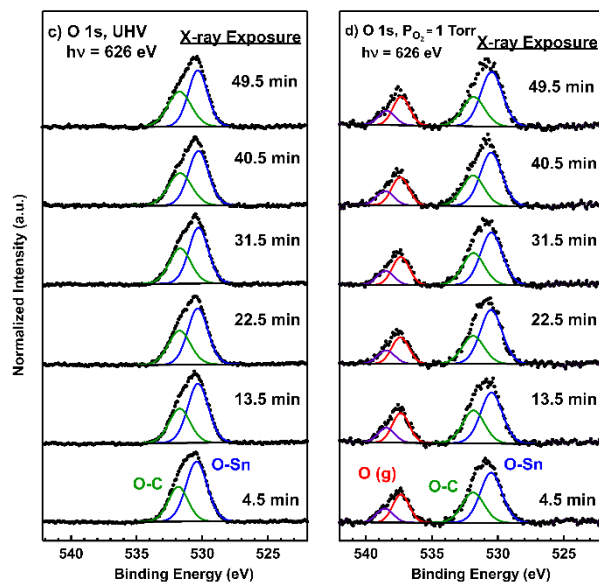


Figure 3.17 APXPS data obtained for different X-ray exposure times for C 1s in (a) UHV and (b) $P_{O_2} = 1$ Torr, and O 1s in (c) UHV and (d) $P_{O_2} = 1$ Torr.

To better quantify the changes in the spectra shown in Figure 3.17, we have plotted peak intensity ratios with respect to X-ray exposure time. In Figure 3.18 (a-c) we show the intensity ratio of the C-H component for each spectrum divided by the C-H component from the initial spectrum with respect to X-ray exposure time. Plotting the data in this manner highlights the changes in intensity during the X-ray exposure. In Figure 3.18a, we show the C-H intensity ratio versus X-ray exposure time for four different photon energies in UHV. For these data, very little change in the C-H intensity ratio was observed, with a maximum decrease of 10% compared to the original C-H intensity ratio. In Figure 3.18 (b), we show changes in the C-H intensity ratio versus X-ray exposure time for four different photon energies at $P_{O_2} = 0.01$ Torr. We find that there was a significant decrease in the C-H intensity ratio compared to the UHV data, and that the decrease has a

photon energy dependence. The maximum decrease in the C-H intensity ratio was 37% compared to the original C-H intensity ratio. In Figure 3.18(c), we show changes in the C-H intensity ratio versus X-ray exposure time for four different photon energies at $P_{O_2} = 1$ Torr. An even higher decrease in C-H intensity ratio (~ 0.52) was observed at this pressure. Again, the rate of decrease in the C-H intensity ratio has a photon energy dependence.

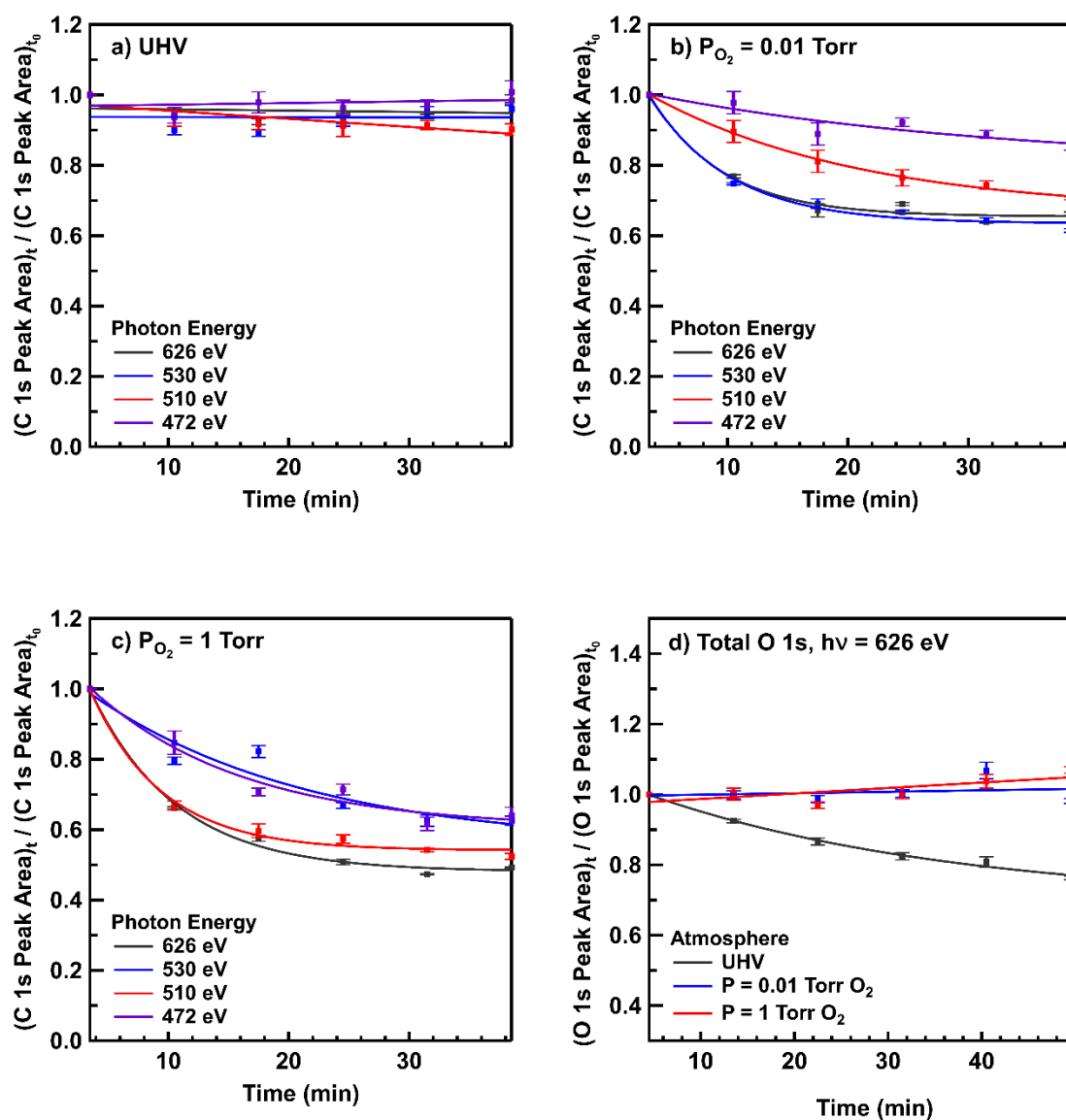


Figure 3.18 X-ray induced changes in peak intensity ratios: C-H component of the C 1s spectra obtained in (a) UHV, (b) $P_{O_2} = 0.01$ Torr, (c) $P_{O_2} = 1$ Torr, and (d) Total O 1s spectra at $h\nu = 626$ eV for indicated oxygen pressures. The indicated curves in the figure (b,c) are fits to equation 1, while the lines in figure (a) are fits to a linear function. In figure (d) the UHV data are fit to equation 1, while the ambient oxygen data are fits to a linear function.

The data imply that main path for the reduction in the C 1s intensity ratio is through homolytic cleavage of the C-Sn bond leading to the loss of butyl ligands from the cluster.^{19, 20} Assuming the observed loss in C 1s intensity correlates to the desorption of butyl ligands, we can apply a photon stimulated desorption (PSD) model to the data. For PSD, an exponential model has been used to fit the observed changes in intensities. For this analysis, the coverage of the radiation-sensitive ligand with respect to photon exposure time can be fit using equation 1:

$$I(t) = I_0 \exp[-\sigma \phi t] + I_\infty \quad (1)$$

where $I(t)$ is the peak intensity of the radiation sensitive ligand at time t , σ is the desorption cross section, ϕ is the photon flux, I_∞ is the peak intensity of the radiation sensitive ligand at $t = \infty$, and I_0 is the peak intensity of the radiation sensitive ligand at $t = 0$. At $t = 0$, equation 1 simplifies to $I_0 = I(t = 0) + I_\infty$, and can be normalized by dividing by $(I_0 + I_\infty)$ to obtain equation 2:

$$y(t) = A \exp[-\sigma \phi t] + y_\infty \quad (2)$$

where $y(t)$ is the peak intensity ratio of the radiation sensitive ligand at time t , σ is the effective desorption cross section in cm^2 , φ is the photon flux (photons/ cm^2/s), y_∞ is the peak intensity ratio at $t = \infty$, and $A = 1 - y_\infty$. This model allows for a quantitative comparison of the decrease in the C 1s signal for each experimental condition, which we correlate to the loss of the butyl ligands. The lines shown in Figure 3.18(b,c) are based on the results of equation 2. By fitting the data to an exponential model and dividing the constant in the exponential term by the photon flux, σ can be calculated. This cross section represents the total amount of C-H removed with each incident photon. The absorption of incident X-rays results in the emission of photoelectrons (the initial direct excitation process), Auger electrons, secondary electrons, and thermal excited electrons. This cross section we extracted is effective for absorption of the incident X-rays by any atom in the cluster, not just a specific atom. However, by varying the photon energy we can enhance the relative X-ray absorption for specific elements. For $P_{O_2} = 0.01$ and 1 Torr, we find that σ ranges from 8×10^{-18} to $4 \times 10^{-17} \text{ cm}^2$ where the lowest value was found for $h\nu = 472 \text{ eV}$ at $P_{O_2} = 0.01$ Torr and the highest value was found for $h\nu = 510 \text{ eV}$ at $P_{O_2} = 1$ Torr. Exponential fits were only used for fitting the C-H intensity ratio in $P_{O_2} = 0.01$ and 1 Torr. A linear model was used to fit the C-H intensity ratio in UHV and is included in Figure 3.18(a) to provide a visual representation of the relative changes.

As mentioned above, we have found that the C-H intensity ratio depends on both the ambient conditions and the photon energy. This suggests that both of these factors influence the rate of butyl ligand desorption from the $\beta\text{-NaSn}_{13}$ resists. We

believe that ambient O_2 is adsorbed in the β - $NaSn_{13}$ resists and that reactive oxygen species form during inelastic scattering of the initially emitted and secondary electrons. For the electron kinetic energy range for these electrons (< 90 eV) molecular oxygen has high cross sections for electronic excitations, ionization and dissociation, which can lead to the formation of reactive oxygen species.²¹ In our studies, the O_2 ambient provides two potential reaction pathways: the electrons emitted from the β - $NaSn_{13}$ resists can interact with O_2 adsorbed in the film, resulting in the formation of reactive oxygen species that preferentially interact with the butyl ligands; or the gas phase O_2 can absorb the X-rays, leading to electron emission in the gas phase, which would simultaneously reduce the X-ray flux at the β - $NaSn_{13}$ resist and create extra electrons. An increase in the number of emitted electrons or the presence of reactive oxygen species is expected to result in a larger loss of butyl ligands from the β - $NaSn_{13}$ resist. To assess the total number of emitted electrons at a given photon energy, we used the TEY XAS data below.

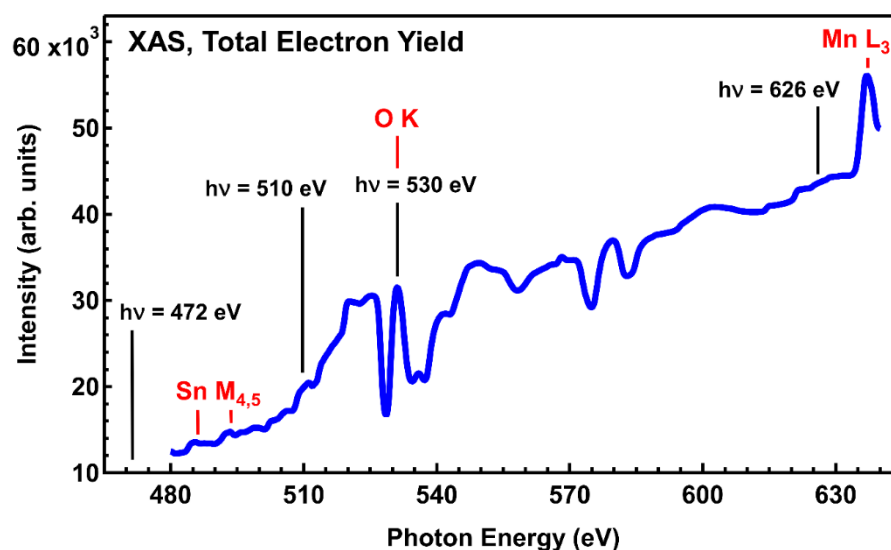


Figure 3.19 TEY XAS obtained from a β -NaSn₁₃ film.

In Table 3.4 we provide normalized TEY for β -NaSn₁₃ films at each photon energy using the TEY at $h\nu = 472$ eV. The data indicates that both $h\nu = 530$ and 626 eV have much higher TEY than either $h\nu = 472$ and 510 eV. For $P_{O_2} = 0.01$ Torr we find that $h\nu = 530$ and 626 eV have the largest C-H loss, and these photon energies correspond to the highest TEY in Table 3.4. However, for $P_{O_2} = 1$ Torr we find that $h\nu = 626$ eV still has the largest C-H loss, but $h\nu = 510$ eV has a larger C-H loss compared to $h\nu = 530$ eV. This may be due to an increase in the absorption of the photons by gas phase O₂ at the O K edge ($h\nu = 530$ eV). The expected X-ray attenuation was calculated at each photon energy compared to UHV by our collaborators, and these results are also provided in Table 3.4.²² They suggest that the X-ray attenuation at the different oxygen partial pressures should result in only a minor variation in the X-ray flux at the sample.

Table 3.4 Ratio of TEY from β -NaSn₁₃ resists normalized to $h\nu = 472$ eV. Ratio of X-ray attenuation for different photon energies and oxygen partial pressures normalized to UHV. Photoabsorption cross section values obtained from Henke, et al.

h ν (eV)	UHV Normalized TEY Intensities	Attenuation of X-rays Normalized to UHV	
		0.01 Torr	1 Torr
472	1.0000	1.0000	0.9973

510	1.5934	1.0000	0.9978
530	2.1454	1.0000	0.9980
626	3.4893	0.9997	0.9745

To evaluate the effect that radiation exposure time has on the oxygen species in the β -NaSn₁₃ clusters we have performed an analysis similar to what was done for the C 1s data. We have calculated an O 1s intensity ratio by dividing the intensity of each O 1s spectrum by the intensity of the initial O 1s spectrum after the indicated X-ray exposure time. In Figure 3.18 Figure 3.18 X-ray induced changes in peak intensity ratios: C-H component of the C 1s spectra obtained in (a) UHV, (b) $P_{O_2} = 0.01$ Torr, (c) $P_{O_2} = 1$ Torr, and (d) Total O 1s spectra at $h\nu = 626$ eV for indicated oxygen pressures. The indicated curves in the figure (b,c) are fits to equation 1, while the lines in figure (a) are fits to a linear function. In figure (d) the UHV data are fit to equation 1, while the ambient oxygen data are fits to a linear function.(d), we show the O 1s intensity ratio obtained using $h\nu = 626$ eV for β -NaSn₁₃ resists in UHV and at $P_{O_2} = 0.01$ and 1 Torr for different X-ray exposure times. The O 1s intensity ratio obtained in UHV decreased for longer X-ray exposure times, while the O 1s intensity ratio obtained in $P_{O_2} = 0.01$ and 1 Torr slightly increased for longer X-ray exposure times. We found that the O 1s intensity ratio obtained in UHV decreased by ~ 0.23 , while the O 1s intensity ratio obtained in $P_{O_2} = 0.01$ and 1 Torr increased by ~ 0.05 . The same PSD model described above was used to fit the O 1s data obtained in UHV and is indicated by the solid black line. A linear model was used to fit the O 1s data obtained in $P_{O_2} = 0.01$ and 1 Torr and these are indicated by the solid blue and red lines, respectively.

To gain further insight into how the chemical composition of the β -NaSn₁₃ films change we have determined the atomic percent (At.%) before and after X-ray exposures. In Figure 3.20 we show At.% for spectra obtained after a 42 minute X-ray exposure with $h\nu = 626$ eV. It should be noted that similar results were obtained for $h\nu = 472, 510$ and 530 eV. These results indicate only negligible changes for Sn At.% in UHV or as a function of P_{O_2} . This is expected since the likely Sn species are not volatile at room temperature. Furthermore, there was a significant reduction in the C At.% for increasing P_{O_2} compared to radiation exposure in UHV, which is due primarily to the reduction in the C-H component. As already mentioned above, a reduction in C-H component suggests the desorption of butyl ligands from the β -NaSn₁₃ films. Both the C-O and C=O components are found to increase with P_{O_2} compared to the UHV case, which indicates that some butyl ligands are oxidized during X-ray exposure in the presence of O₂, and these species remain in the film. There was only a negligible increase in the total O atomic concentrations for increasing P_{O_2} compared to UHV. We found that the O-Sn component increased when going from $P_{O_2} = 0.01$ to 1 Torr and that there was an increase in O-C/O-H at $P_{O_2} = 0.01$ Torr and a decrease at $P_{O_2} = 1$ Torr. The ratio of O-Sn:O-C/O-H also increases for higher P_{O_2} . When $P_{O_2} = 1$ Torr, the conversion to SnO₂ is maximized and the O-C/O-H component makes up a much smaller portion of the total O 1s intensity. These results suggest we are increasing the rate at which β -NaSn₁₃ converts to SnO₂ through exposure to a higher ambient pressure of O₂. Furthermore, there is an increase in oxygenates on the surface which provides another route to Sn

oxidation. These species could possibly act as intermediates during the reaction, which is why they make up a larger component of the film in the lower O_2 ambient pressure.

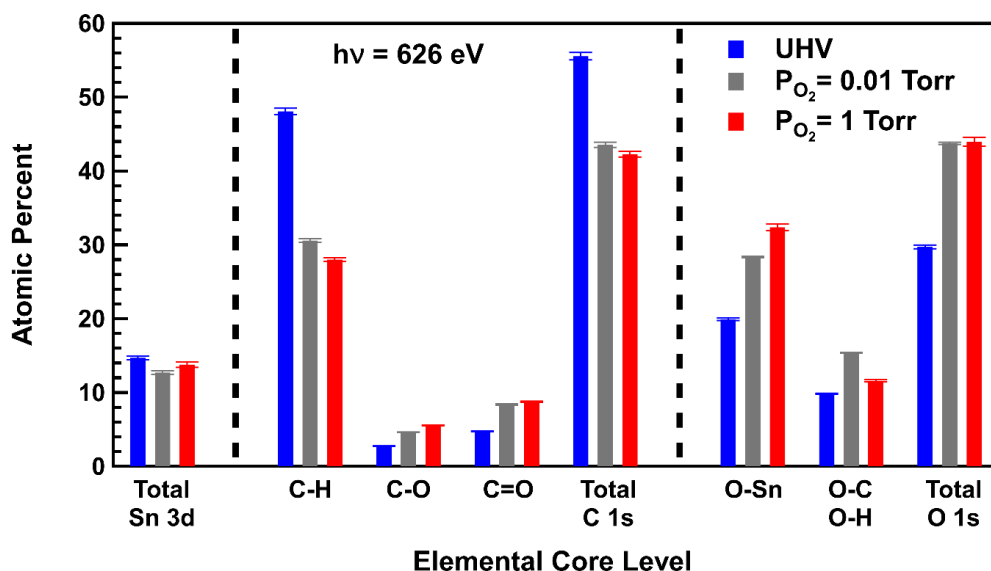


Figure 3.20 Atomic percent calculations showing the compositional changes for C 1s, O 1s, and Sn 3d core levels and their respective chemical states after sequential C 1s scans (42 min of exposure) at $h\nu = 626$ eV.

We find that removal of less than half of the butyl groups from the β -NaSn₁₃ cluster results in a change in solubility.²³ It is expected that further removal of butyl ligands or oxidation of Sn occurs during the development process which includes a 170 °C anneal in air and soaking in 2-heptanone. Further investigation of the composition following both the anneal and developer soak are necessary to obtain a complete understanding of the solubility transition mechanism. By investigating ambient gasses with different oxidative strength, we can determine

how the related species could be integrated into the resist to improve EUV sensitivity.

We have demonstrated that the addition of oxygen during β -NaSn₁₃ radiation exposure enhances the rate at which the cluster desorbs butyl groups. The addition of O₂ during EUV lithography may reduce the necessary dose to achieve the solubility transition, and thereby reduce the time required to pattern a wafer. This also likely holds true for other polyoxometallic nanocluster resists, where the chemical mechanism relies on creating secondary and thermal electrons that result in homolytic bond cleavage through inelastic scattering. Further studies are still required to determine the mechanisms that take place through each step of the EUV lithography process. For our APXPS studies, the photon dose used ($\sim 1 \times 10^{19}$ photons/cm²) is likely several orders of magnitude higher than the dose required to achieve the solubility transition. Performing similar experiments with a lower photon flux and at appropriate EUV radiation energies should provide further information on the distinct chemical changes occurring during EUV exposures.

3.3.4 Possible radiation reaction pathways

Table 3.5 Bonding energy comparison within the Keggin cluster structure.

Bond	D (KJ/mol)	R (pm)	eV
H-O	459	96	4.757216
H-C	411	109	4.259729

would attack tin in another cluster and force a butyl group to leave. Then a Sn-O-Sn bond could form, lowering cluster solubility. The lower one shows the reaction driven by breaking of the weak Sn-C bond. It has the lowest dissociative energy in the cluster, around 2 eV. The partially occupied tin would enhance the chance of condensation reaction by losing a water molecule.

Figure 3.22 ¹⁴ provides a visual representation of mechanisms that occur in the β -NaSn₁₃ resist when exposed to radiation under different ambient conditions. A portion of the β -NaSn₁₃ cluster is shown Figure 3.22(a), and shows one Sn ion bound to structural oxygen and methoxy/hydroxyl groups. Figure 3.22(a, b) illustrate that two different reaction pathways can occur during EUV exposure in UHV and $P_{O_2} = 1$ Torr, respectively. When the clusters absorb EUV radiation both photo- and Auger electrons are emitted from the atoms in the cluster. Inelastic scattering of these electrons leads to formation of both low energy secondary and thermal electrons. These electrons have enough kinetic energy to drive reactions that further modify the cluster chemistries. During this process, ambient oxygen molecules also interact with the emitted electrons leading to an increase in the number of reactive oxygen species that are formed. The C-Sn bond is the weakest bond in the cluster and butyl ligands undergo homolytic cleavage as shown in Figure 3.22(d) due to inelastic scattering of the electrons. In UHV, the only oxygen available to oxidize the Sn is from within the cluster. This process requires additional energy to break the bond between the hydrogen or methyl group and oxygen. The resulting O ion may form a double bond in order to restore charge neutrality. In the presence of oxygen, three additional reaction

pathways are possible. In Figure 3.22(e), the reactive oxygen species can enhance the removal of methoxy/hydroxyl ligands which leads to an increase in the rate of conversion to SnO_2 . In Figure 3.22(f), the reactive oxygen species can react directly with Sn, which results in oxidation without a change in coordination. In Figure 3.22(g), reactive oxygen species can react with two Sn groups in adjacent clusters leading to Sn-O-Sn linking.

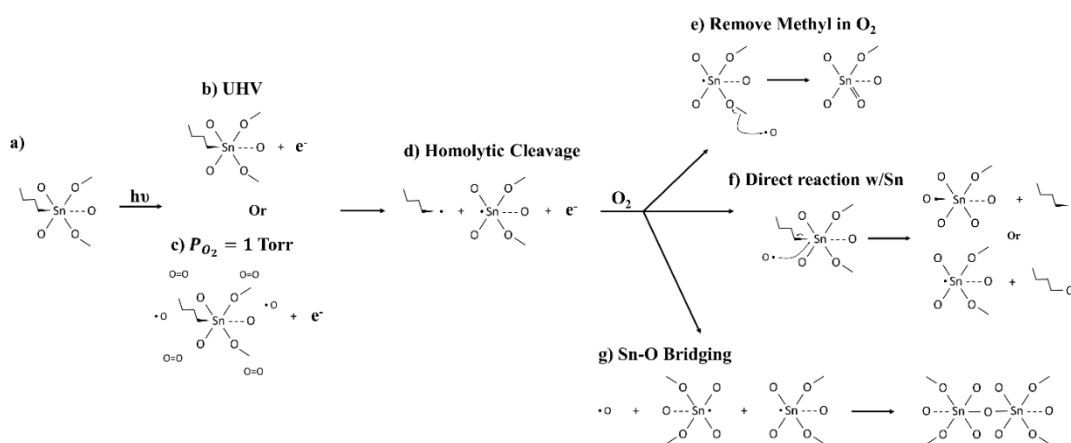


Figure 3.22 Proposed mechanism showing the conversion from $\beta\text{-NaSn}_{13}$ to SnO_2 . Photons are absorbed leading to photoemission (a), followed by electron scattering and generation of secondary electrons (b and c). The homolytic cleavage of butyl ligands (d) is enhanced in the presence of oxygen and provides a more efficient route to SnO_2 (e, f, and g).

Reference

1. Saha, S.; Park, D. H.; Hutchison, D. C.; Olsen, M. R.; Zakharov, L. N.; Marsh, D.; Goberna - Ferrón, S.; Frederick, R. T.; Diulus, J. T.; Kenane, N. J. A. C., Alkyltin Keggin Clusters Templated by Sodium. **2017**, 129 (34), 10274-10278.
2. Eychenne-Baron, C.; Ribot, F.; Sanchez, C. J. J. o. o. c., New synthesis of the nanobuilding block $\{(BuSn)_{12}O_{14}(OH)_6\}^{2+}$ and exchange properties of $\{(BuSn)_{12}O_{14}(OH)_6\}(O_3SC_6H_4CH_3)_2$. **1998**, 567 (1-2), 137-142.
3. Amador, J. M., Metal-oxo Clusters as Novel Photolithographic Materials: How Understanding the Chemistry of $HfSO_x$ Informs Next-Generation Patterning Systems. **2017**.
4. Tanaka, K.; Matsuzaki, S.; Toyoshima, I., Photodecomposition of adsorbed methoxy species by UV light and formaldehyde adsorption on silicon (111) studied by XPS and UPS. *The Journal of Physical Chemistry* **1993**, 97 (21), 5673-5677.
5. Frederick, R. T.; Diulus, J. T.; Lyubinetsky, I.; Hutchison, D. C.; Olsen, M. R.; Nyman, M.; Herman, G. S. In *Surface characterization of tin-based inorganic EUV resists*, Advances in Patterning Materials and Processes XXXV, International Society for Optics and Photonics: 2018; p 1058607.
6. Lin, A. W.; Armstrong, N. R.; Kuwana, T., X-ray photoelectron/Auger electron spectroscopic studies of tin and indium metal foils and oxides. *Analytical Chemistry* **1977**, 49 (8), 1228-1235.
7. Rehr, J. J.; Albers, R. C., Theoretical approaches to x-ray absorption fine structure. *Reviews of modern physics* **2000**, 72 (3), 621.
8. Kaya, S.; Ogasawara, H.; Näslund, L.-Å.; Forsell, J.-O.; Casalongue, H. S.; Miller, D. J.; Nilsson, A., Ambient-pressure photoelectron spectroscopy for heterogeneous catalysis and electrochemistry. *Catalysis today* **2013**, 205, 101-105.
9. Kwoka, M.; Czempik, G.; Szuber, J., X-ray photoemission spectroscopy study of the surface chemistry of laser-assisted chemical vapour deposition SnO_x thin films after exposure to hydrogen. *acta physica slovacica* **2005**, 55 (3), 331-339.
10. Petoral Jr, R. M.; Uvdal, K., XPS and NEXAFS study of tyrosine-terminated propanethiol assembled on gold. *Journal of electron spectroscopy and related phenomena* **2003**, 128 (2-3), 159-164.
11. Bancroft, G.; Nesbitt, H.; Ho, R.; Shaw, D.; Tse, J.; Biesinger, M., Toward a comprehensive understanding of solid-state core-level XPS linewidths: Experimental and theoretical studies on the Si 2 p and O 1 s linewidths in silicates. *Physical review B* **2009**, 80 (7), 075405.
12. Süzer, S., Electron spectroscopic investigation of polymers and glasses. *J Pure applied chemistry* **1997**, 69 (1), 163-168.
13. Kövér, L.; Kovács, Z.; Sanjinés, R.; Moretti, G.; Cserny, I.; Margaritondo, G.; Pálinkás, J.; Adachi, H., Electronic structure of tin oxides:

- High - resolution study of XPS and Auger spectra. *J Surface interface analysis* **1995**, 23 (7 - 8), 461-466.
14. Diulus, J. T.; Frederick, R. T.; Li, M.; Hutchison, D. C.; Olsen, M. R.; Lyubinetsky, I.; Árnadóttir, L.; Garfunkel, E. L.; Nyman, M.; Ogasawara, H. J. A. a. m.; interfaces, Ambient-Pressure X-ray Photoelectron Spectroscopy Characterization of Radiation-Induced Chemistries of Organotin Clusters. **2018**, 11 (2), 2526-2534.
 15. Haitjema, J.; Zhang, Y.; Ottosson, N.; Brouwer, A. M., Photoreactions of tin oxo cages, model EUV photoresists. *Journal of Photopolymer Science and Technology* **2017**, 30 (1), 99-102.
 16. Frederick, R. T.; Diulus, J. T.; Hutchison, D. C.; Nyman, M.; Herman, G. S., Effect of Oxygen on Thermal and Radiation-Induced Chemistries in a Model Organotin Photoresist. *ACS applied materials & interfaces* **2019**, 11 (4), 4514-4522.
 17. Shuttleworth, D., Preparation of metal-polymer dispersions by plasma techniques. An ESCA investigation. *The Journal of Physical Chemistry* **1980**, 84 (12), 1629-1634.
 18. Yildirim, O.; Buitrago, E.; Hoefnagels, R.; Meeuwissen, M.; Wuister, S.; Rispens, G.; van Oosten, A.; Derks, P.; Finders, J.; Vockenhuber, M. In *Improvements in resist performance towards EUV HVM*, Extreme Ultraviolet (EUV) Lithography VIII, International Society for Optics and Photonics: 2017; p 101430Q.
 19. Cardineau, B.; Del Re, R.; Marnell, M.; Al-Mashat, H.; Vockenhuber, M.; Ekinci, Y.; Sarma, C.; Freedman, D. A.; Brainard, R. L., Photolithographic properties of tin-oxo clusters using extreme ultraviolet light (13.5 nm). *Microelectronic Engineering* **2014**, 127, 44-50.
 20. Frederick, R. T.; Saha, S.; Diulus, J. T.; Luo, F.; Amador, J. M.; Li, M.; Park, D.-H.; Garfunkel, E. L.; Keszler, D. A.; Herman, G. S., Thermal and radiation chemistry of butyltin oxo hydroxo: A model inorganic photoresist. *Microelectronic Engineering* **2019**, 205, 26-31.
 21. Kövér, L.; Moretti, G.; Kovács, Z.; Sanjinés, R.; Cserny, I.; Margaritondo, G.; Pálinkás, J.; Adachi, H., High resolution photoemission and Auger parameter studies of electronic structure of tin oxides. *Journal of Vacuum Science & Technology A: Vacuum, Surfaces, and Films* **1995**, 13 (3), 1382-1388.
 22. Hinsberg, W. D.; Meyers, S. In *A numeric model for the imaging mechanism of metal oxide EUV resists*, Advances in Patterning Materials and Processes XXXIV, International Society for Optics and Photonics: 2017; p 1014604.
 23. Yeh, J.; Lindau, I., Atomic subshell photoionization cross sections and asymmetry parameters: $1 \leq Z \leq 103$. *Atomic data and nuclear data tables* **1985**, 32 (1), 1-155.

Chapter 4: Patterning properties of organotin resist

4.1 Introduction

Materials with HAR (high aspect ratio) features have very broad and significant applications, including FinFETs, diffractive optics, battery anodes and sensors.¹⁻³ The lithography step is often at the heart of the process. Especially for transistors and related nano-electronics components, dense critical three-dimensional patterns are required for low cost and high performance (as anticipated by Moore's law). After decades of efforts by industrial and academic researchers, EUVL is ready to apply in high-volume manufacturing semiconductor processing.⁴ Some issues related to EUVL hardware are still to be resolved such appropriate source power, pellicles and mask defects. In addition, the optimal photoresist material(s) for EUVL remains a major focus for material scientists; with organic and inorganic-based materials still competing as this thesis goes to press. The proper material requires optimization of several basic parameters: sensitivity, critical dimension and the etching selectivity. Metal-based photoresists usually have better resistivity to either wet or dry etching. Also the EUV absorption cross sections of metals are higher than that of carbon or oxygen in organic resists. Hafnium, antimony and tin are three popular metallic components of nano-scale clusters with high absorption cross sections that have been studied as photoresist materials.^{5, 6} In this chapter we report on the use of Helium Ion Beam Lithography (HIBL) to prescreen EUV resists prior to their

evaluation in the EUV scanner. Helium ions as a proxy for photons have certain benefits; they scatter less than electrons, and produce fewer energetic recoil-atoms when compared to heavy ion irradiation. The negligible proximity effect of HIBL also has the potential to give very high lateral resolution.⁷ A comparison between EUV and 30 keV helium ion exposure was reported earlier showing highly similar trends in dose response. One single 30 keV helium ion can be as effective as 150 EUV photons in terms of secondary electron generation. Hence the HIBL has important advantages for critical dimension patterning and can serve as a stringent test of resist performance.⁸

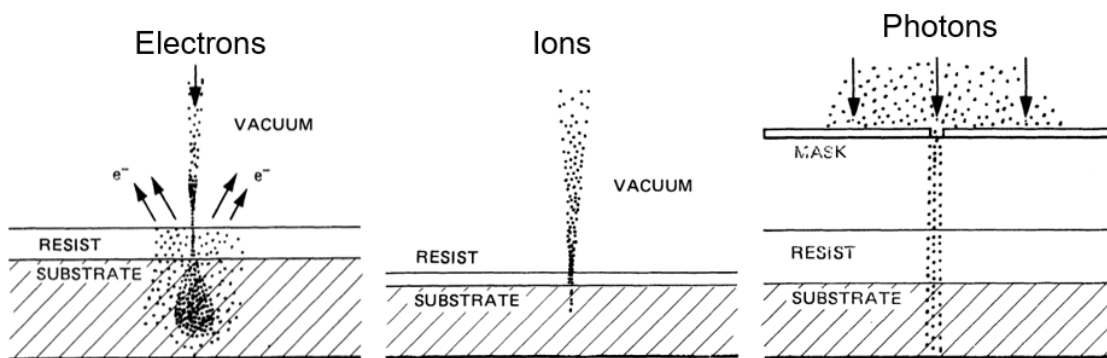


Figure 4.1 Incident particle options for use in micro- or nano-structure fabrication.⁹

Table 4.1 Ion and photon beams both share the potential for high resolution and similar secondary electron generation process while HIM is more accessible than a commercial EUV scanner (because of cost).

Incident beam	Electron	Ion	Photon
Lateral resolution	-	+	+

Penetration depth	+	-	+++
SE yield	+	+	+
HVM	-	-	+++

In order to obtain critical dimension features without pattern collapse and other detrimental issues, resist films of order 20 nm or even less are preferred.¹⁰ With thin films, the energy and secondary electrons from the substrates generated by the incident ion, electron or photon beam might also play a role in the lithography process; this is a secondary process that has only been studied to a limited extent to date. One simulation of EUV exposures shows a significant difference between copper and silicon substrates,¹¹ related to higher absorbed energy in copper based materials resulting in additional chemical interactions in the resist.

A β -NaSn₁₃ resist with oxo-hydroxo bonds was reported to show potential for radiation-induced condensation as a photoresist 错误!未找到引用源。¹² We now describe below the patterning properties of the β -NaSn₁₃ resist when combined with etching resistance tests using HIBL. Monte Carlo simulations were also performed to explain the thickness and substrate dependence in the lithography.

A Carl Zeiss ORION PLUS HIM system was used for patterning and imaging. The Orion produces a 30KeV He⁺ beam with beam spot sizes as small as 0.5 nm. The ion current to the sample was kept below 1 pA. Pixel (lateral sampling) spacing was set to 1 nm. The nominal exposure line width was set from 1 nm to 20 nm with 100 nm spacing in order to determine the best critical dimensions

under given lithography conditions. Following the helium ion exposure, a post exposure bake was applied at 175 °C for 5 mins. Then the films were developed in 2-heptanone for 1 min and blow dried with compressed nitrogen.

4.2 Best patterning performance achieved

This part of thesis is composed in part of published results¹³. Our work with $[\text{NaO}_4(\text{BuSn})_{12}(\text{OH})_3(\text{O})_9(\text{OCH}_3)_{12}(\text{Sn}(\text{H}_2\text{O})_2)]$ followed a slightly modified procedure compared to that in the literature.¹⁴ BuSnOOH (Sigma-Aldrich) was suspended in methanol (Sigma-Aldrich) at a concentration of 0.08 g/mL. The solution was sonicated to ensure maximum dissolution of the soluble material, and then centrifuged to remove the insoluble material. The supernatant was transferred to a closed glass container and allowed to sit undisturbed at room temperature. Within one day, crystals would grow and were isolated from the walls of the container. The supernatant was removed under reduced pressure to collect solid precursor crystals. Precursor solutions were prepared in two ways to provide films with different thickness. For thicker films 20 mg/mL $\beta\text{-NaSn}_{13}$ solution with 2-heptanone was used as the solvent, while for thinner films the concentration was 5 mg $\beta\text{-NaSn}_{13}$ per 1.5 mL toluene. The films were sonicated for 5 min for complete dissolution. All samples were made fresh prior to film deposition.

Prior to the $\beta\text{-NaSn}_{13}$ deposition, the Si wafers were cleaned by consecutive sonication in acetone, isopropanol and deionized water (18.2 MΩ). Next, the non-oxidized Si wafers (with native oxides) were treated with a 49% HF solution to create a hydrogen terminated surface without oxides. The precursor solutions

were filtered by 0.45 μm PTFE (Polytetrafluoroethylene) filters and then deposited by spin coating (in a Laurell Technologies spincoater) at 3000 rpm for 30 s with an acceleration rate of 3000 rpm/s, and finally soft baked at 70 $^{\circ}\text{C}$ for 3 mins. For thinner films, HMDS (hexamethyldisilazane) was used to enhance adhesion of the photoresist to the surfaces by spin dry with 3000 rpm for 30 s. After cooling in air, the films were ready for patterning and characterization.

4.2.1 Sensitivity

Using a high resolution helium ion beam has several positive features for nanolithography including very high lateral resolution ($<10\text{nm}$), precisely tunable dose, and very high scattering cross section. It was used for our demonstration of HIBL of our Keggin films. We used 20 nm thick films to investigate the etching selectivity and pattern stability of the resist. An array of $2\times 2\ \mu\text{m}^2$ square patterns was made by the 30 keV helium ion beam with different doses. AFM measured the remaining film thickness yielding the $\beta\text{-NaSn}_{13}$ resist contrast curve in Figure 4.3. D_{100} (the dose at which the developed features start to have 100% of the as-deposit resist thickness) is about $10\ \mu\text{C}/\text{cm}^2$, comparable to the sensitivity of modern (organic) photoresists. We also successfully achieved a good contrast

$$\gamma = \frac{1}{\log_{10} \frac{D_{100}}{D_0}} \sim 2. \text{ Sn-resist sensitivity is comparable to the other best EUV}$$

photoresists (CAR, HfX, etc.).¹⁵

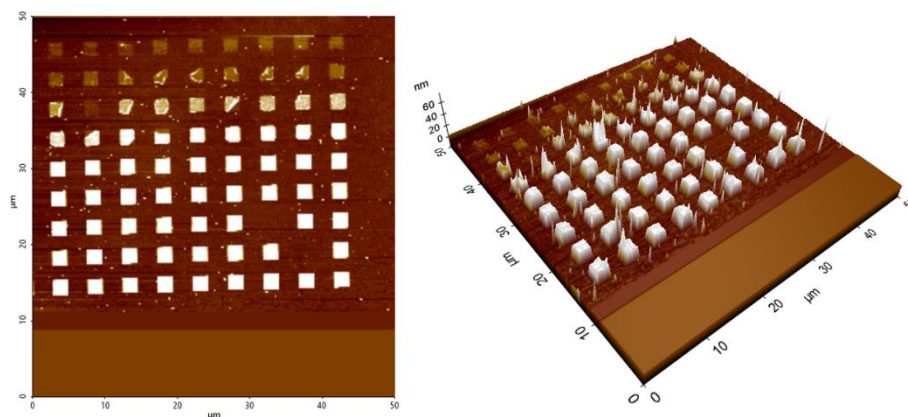


Figure 4.2 AFM image of patterned keggins film with dose from 1~16 $\mu\text{C}/\text{cm}^2$.

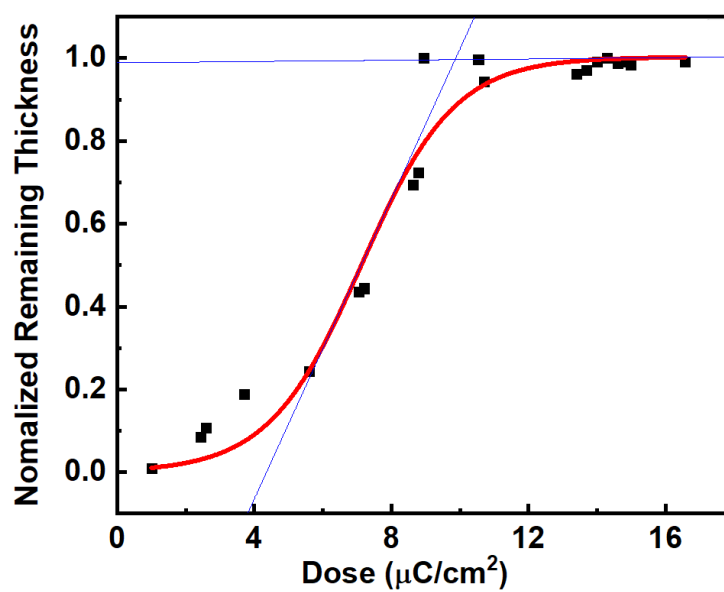
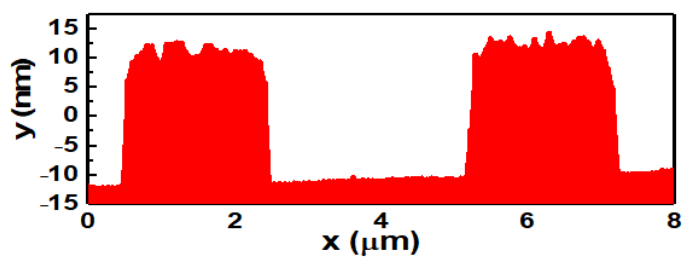


Figure 4.3 Contrast curve of $\beta\text{-NaSn}_{13}$ resist with 30 keV HIBL,



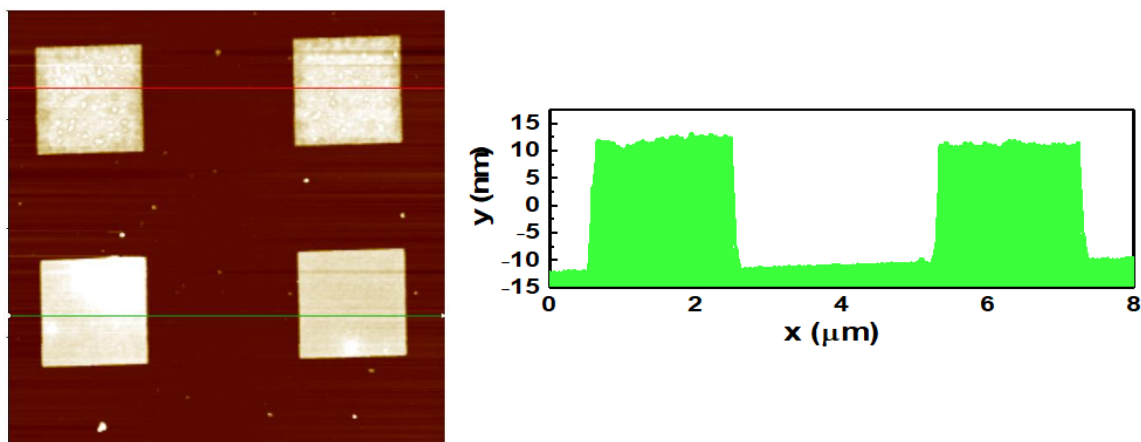


Figure 4.4 AFM line profiles of exposed area with dose at 8.9 and 10.5 $\mu\text{C}/\text{cm}^2$.

With dose at 8.9 $\mu\text{C}/\text{cm}^2$, the exposed film thickness is almost the same as as-deposited film (~ 20 nm). However the roughness is much higher than that with dose at 10.5 $\mu\text{C}/\text{cm}^2$. The non-uniform condensation reaction with insufficient dose might contribute to the roughness. So next step, it would be interesting to investigate the film evolving during the development to understand how the developer etches the film and how the pattern property would change.

4.2.2 Critical dimension and LER

The line edge roughness (LER) and critical dimension (CD) were calculated from high-resolution, top-down secondary electron images of sets of three patterned lines acquired using the Scanning Helium Ion Microscope (SHIM – the same tool used for lithography, but now using in an imaging mode) and following the methods recommended by the ITRS.¹⁶ Images were loaded to the image processing software ImageJ and were smoothed and adjusted for optimal contrast to help determine the line edge structure. Each line was extracted with boxes that include its edges completely. The software we used performs a

Canny-Deriche filter for edge detection. A parameter controls the extent of smoothing of the raw data. The less smoothing we apply, the more accuracy we can detect. However, smoothing can help with easier edge detection. Then we use a non-maximal suppression to get thin edges and another software plugin to perform a hysteresis thresholding for edge detection. We manually adjusted the filtering to get most connected and thinnest edges within the threshold edges. A histogram profile was generated for choosing edges to calculate the average width, width standard deviation, and edge position standard deviation. LER was calculated as three times the standard deviation in the line edge position (average from top and bottom line edges), and the CD is the line width.

We used the Helium ion beam to pattern the photoresist film and obtained AFM images (as noted below). The square patterns received a dose in the range of $1\sim 20\mu\text{C}/\text{cm}^2$. We compared γ -Keggin photoresist on thermal oxide and HF etched silicon substrates. It turns out that the adhesion force between the photoresist film and HF etched silicon is stronger than that between the resist and a thermal oxide substrate. β -Keggin on thermal oxide shows better sensitivity than γ -Keggin. When the dose is as low as $1\mu\text{C}/\text{cm}^2$, the β -Keggin film was almost fully exposed.

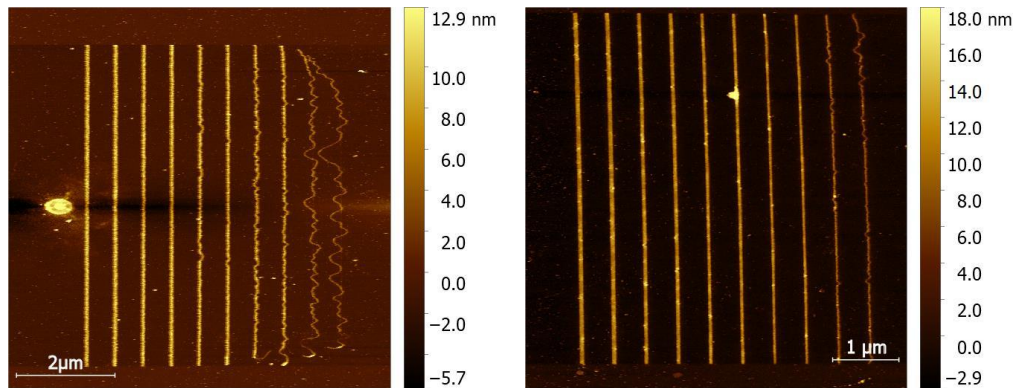


Figure 4.5 Patterned samples: lines (10~50nm Dose: $10\mu\text{C}/\text{cm}^2$)

As to the line patterns, when we zoom in on the image, we found there was a very thin straight line underneath the curvy line. This indicates that the pattern likely has breaks vertically inside the resist film. It could be due to stronger bonding at the interface formed after exposure while the condensation within the film was insufficient to make the resist retain after development. This indicates that we may need to apply a higher dose for line patterns than the square patterns.

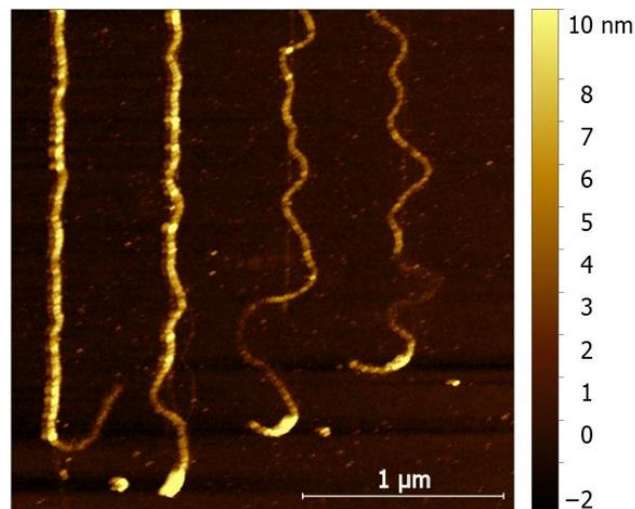


Figure 4.6 Zoom in image of line patterns shows exposed material under wiggling lines.

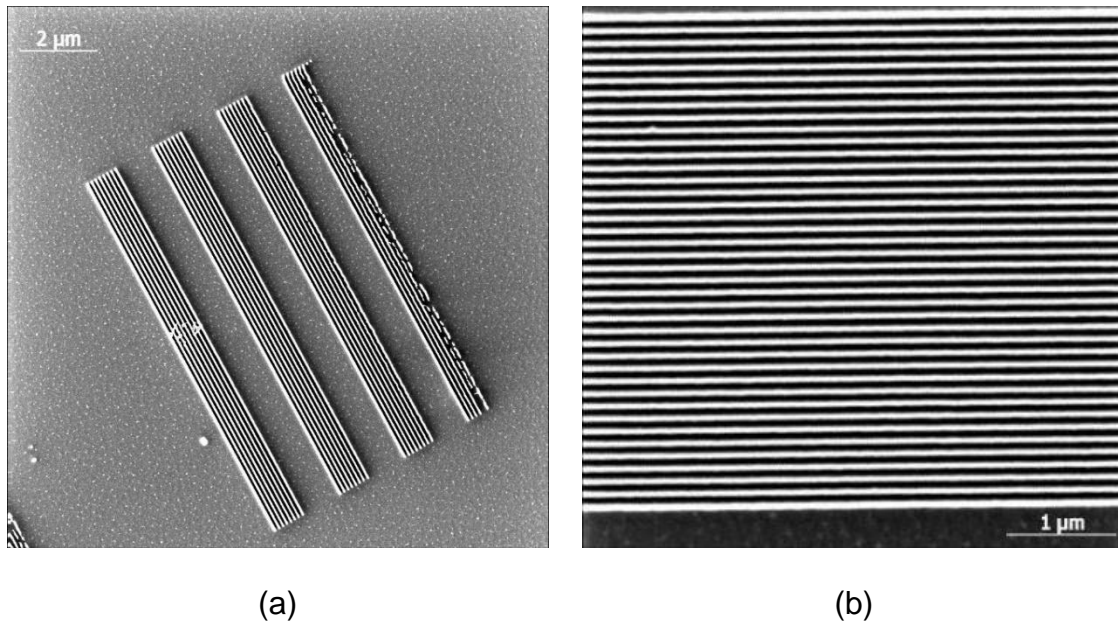


Figure 4.7 Line patterns. (a) Dose scaling of 5, 10, 15 and 20 $\mu\text{C}/\text{cm}^2$ from right to left; (b) 20 nm half pitch dense line patterns.

A higher dose was required to make the straight and solid lines shown in Figure 4.7(a). With a dose of 10 $\mu\text{C}/\text{cm}^2$, we observed discontinuities and wiggles while with a dose of 20 $\mu\text{C}/\text{cm}^2$, photoresist bridging occurred. Only a dose of 15 $\mu\text{C}/\text{cm}^2$ (under our conditions) gave us line patterns without defects. The difference in doses needed for making square and line patterns shows that lateral crosslinking may enhance the sensitivity of the resist. Choosing the proper dose for various patterning sizes and structures might help optimize processing time as well as patterning performance. 20 nm half pitch dense line patterns were achieved after our exposure optimization as shown in Figure 4.7(b).

The radius of a cluster is 5 Å according to both simulation and scattering data, the distance between clusters is 11 Å, and the number of nearest neighbors to a cluster is 0.53.¹⁴ So one molecule in the solution would occupy roughly $\frac{4}{3}\pi(1.1)^3/(1 + 0.53) = 3.64 \text{ nm}^3$. We also note that $15 \mu\text{C}/\text{cm}^2$ corresponds to about 1 ion/nm² which is roughly 1 ion per cluster. The incident ion energy loss per Ångström depth into the film due to ionization should be independent of the resist thickness for very thin films. In thicker line patterns, one ion per resist cluster may be enough to trigger and complete the local condensation chemistry. In thinner films, the total amount of clusters in the vertical direction should be less than that for thicker films. As the ion penetrates the resist film, it might miss some clusters and transfer insufficient energy to the cluster. As a result, fewer secondary electrons might be generated and the number of polymerized clusters will not be enough to maintain pattern shape and continuity.

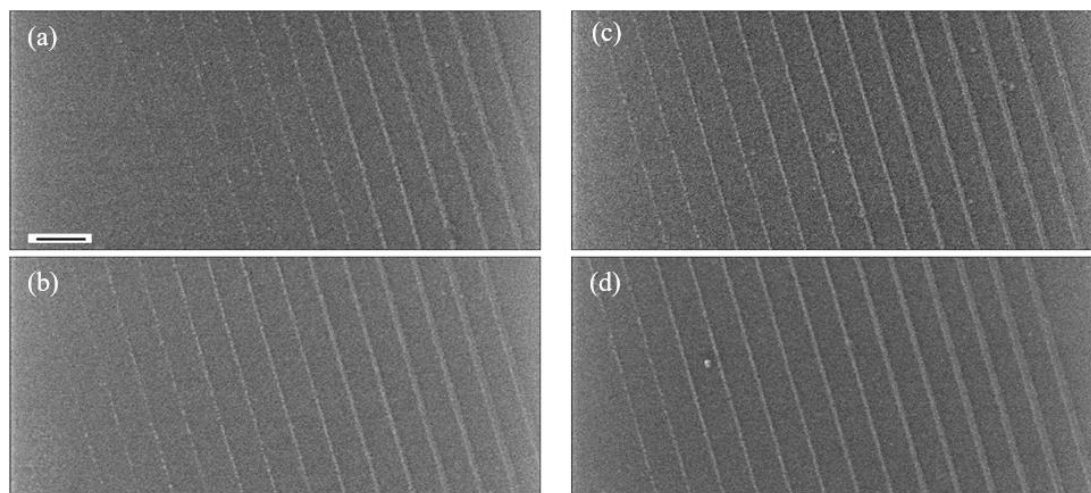


Figure 4.8 (a), (b), (c) and (d) HIM images of line patterns exposed with doses of respectively 10, 15, 20, and $25 \mu\text{C}/\text{cm}^2$. The scale bar is 200 nm for all images.

The nominal line widths are 1, 2, 3, 4, 5, 10, 15, and 20 nm from left to right. A pair of each lines are shown.

We studied 10 nm thick films to investigate the critical dimensions and sensitivity compared to 20 nm thick films. The best critical dimension patterns in Figure 4.9 indicate an average line width as 8.8 nm and LER of 2.1 nm with 10 nm films while with 20 nm films the best average line width was 20.2 nm with LER as 4.2 nm.

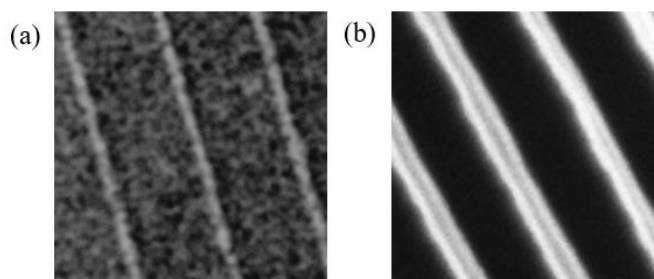


Figure 4.9 (a) and (b) are SHIM images of line patterns used to calculate CD and LER for 10 nm and 20 nm thick film individually.

4.3 Etching selectivity

This part of thesis is composed in part of published results¹³. With β -NaSn₁₃ as photoresist, silicon was etched anisotropically using an Oxford Plasmalab 100 inductively coupled plasma (ICP) etcher in 15 mTorr O₂/SF₆ plasma with flow rates of 15 sccm/40 sccm, respectively. The cryogenic process was maintained at -100 °C with 15 W of RF power for 10 s. High aspect ratio walls were etched in silicon to a depth of 300 nm at an etch rate 30 nm/s. AFM line profiles were measured to obtain the actual etch depth with exposure dose variations as

shown in Figure 4.10. The photoresist mask can protect the substrate completely when it was exposed with enough He ion doses (at least $8\mu\text{C}/\text{cm}^2$).

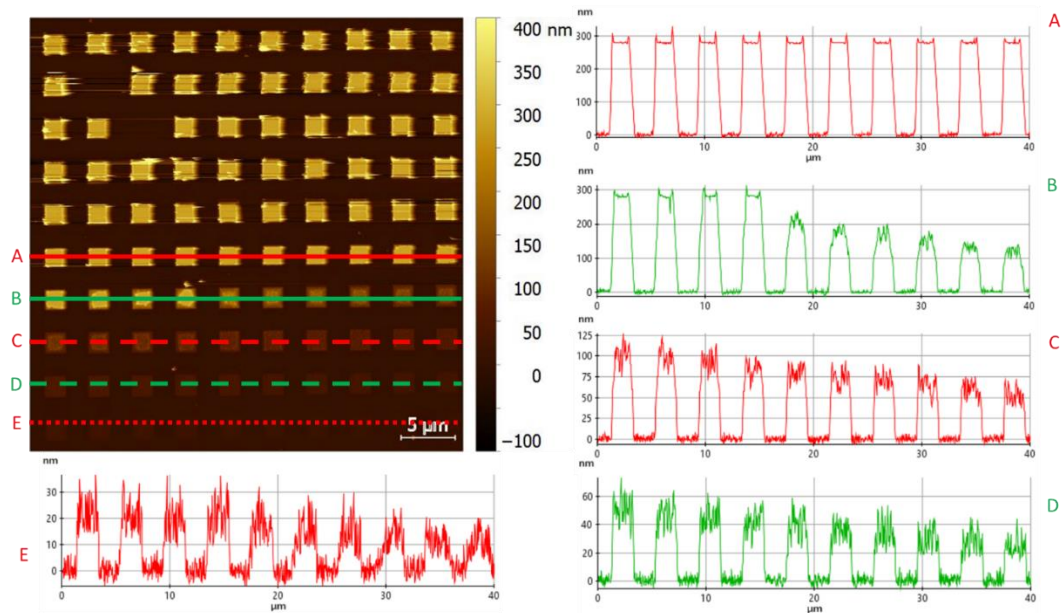


Figure 4.10 Line profiles after dry etching.

SHIM images were acquired to confirm the pattern quality as the helium ion probe is effectively sharper than the AFM tip. Sharp, square-patterned shapes remain after dry etching. Selectivity and etching conditions were appropriate for $2\mu\text{m}$ features in this case.

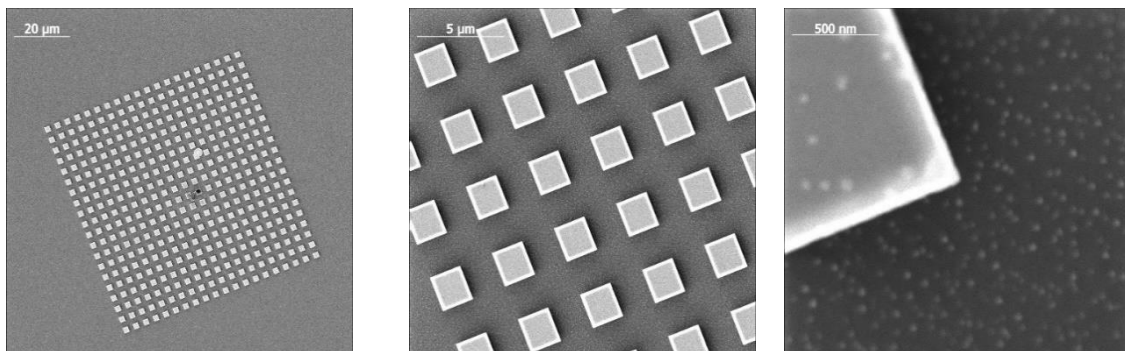


Figure 4.11 Square patterns for etching rate control.

Figure 4.12 shows SHIM images for side views (40° angle) of 20 nm wide and 300 nm tall line patterns exposed on the same sample as the square patterns. These images show features with an aspect ratio of 15:1. Although the side wall was roughened due to the less-than-optimal etching process, we observe no bridging or other defects. The silicon beneath the resist mask was etched laterally to a small extent which would give even narrower trenches after removal of the resist. About 80% of the resist width was maintained with this anisotropic etching, higher aspect ratios with smaller feature sizes should be possible with further etching.

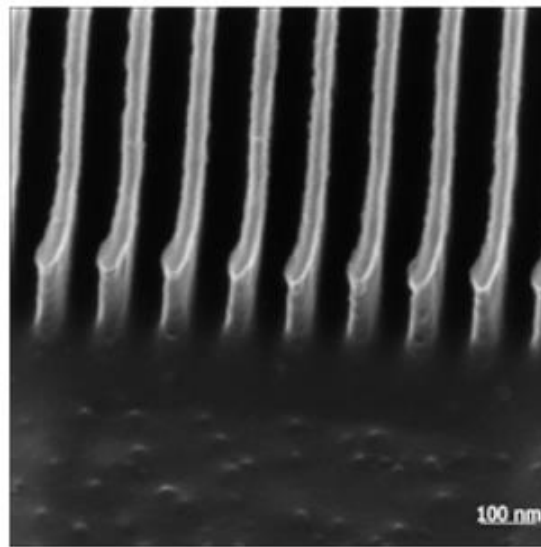


Figure 4.12 40° tilted angle HIM image of etched dense line patterns.

4.4 Interfacial bonding and substrate effects

4.4.1 Implications of interface bonding effects

This part of thesis is composed in part of published results¹⁷. As we have shown, HIBL is an alternative (to EUVL) patterning technique capable of producing sub-10 nm features with high density and resolution.¹⁸⁻²² To realize an optimal

substrate-resist pair for lithography, interfacial interactions between the resist and substrate should be understood, and the pair should show excellent lithographic applicability (i.e. smooth and dense patterns). We used HIBL to pattern lines in Sn Keggin structure resists on Si-OH, Si-H, and SAM-terminated surfaces to explore interface effects. The samples are prepared by our collaborator from Chabal's group in the University of Texas at Dallas. Double-side-polished, float-zone grown Si (111) wafers (lightly n doped, $\rho \sim 20\text{-}60 \text{ } \Omega \text{ cm}$) were used. All samples were first sonicated in dichloromethane, acetone, and methanol for 5 min in each solvent. After degreasing, the sample was thoroughly rinsed with deionized (DI) water before being treated in a piranha solution (1:3 $\text{H}_2\text{O}_2/\text{H}_2\text{SO}_4$ mixture at $80 \text{ } ^\circ\text{C}$) for 30 mins to produce an OH-terminated oxide surface (Si-OH). The sample was rinsed again with DI water and blown dry with nitrogen (N_2) before further processing. For Si-OH samples, no further processing was conducted before spin coating. To create atomically-flat, H-terminated Si (111) surfaces (Si-H), the piranha cleaned sample was first placed in 49% hydrofluoric acid (HF) for 30s and then in ammonium fluoride (NH_4F) for 2.5 min, followed by rinsing the sample with copious amounts of DI water.²³ The grafting of ethyl undecylenate (SAM) to the Si-H surface was done according to a previously reported procedure.²⁴

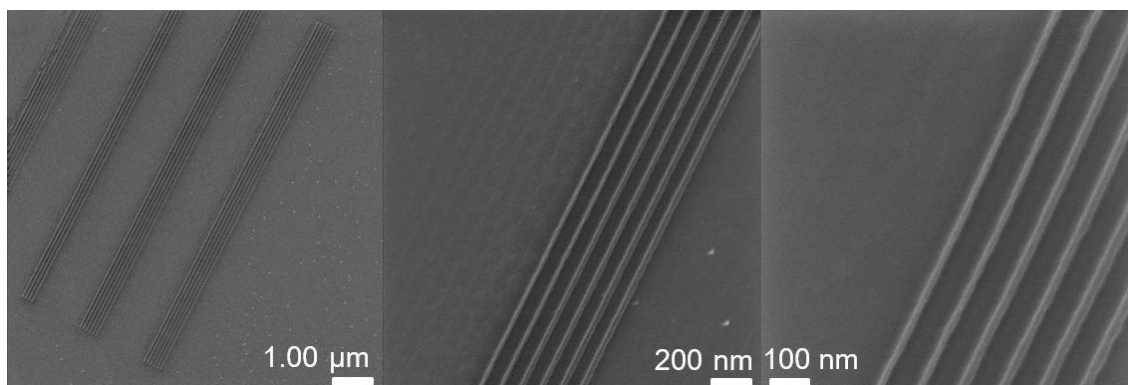


Figure 4.13 Images of Patterned lines of Keggin on Si-OH.

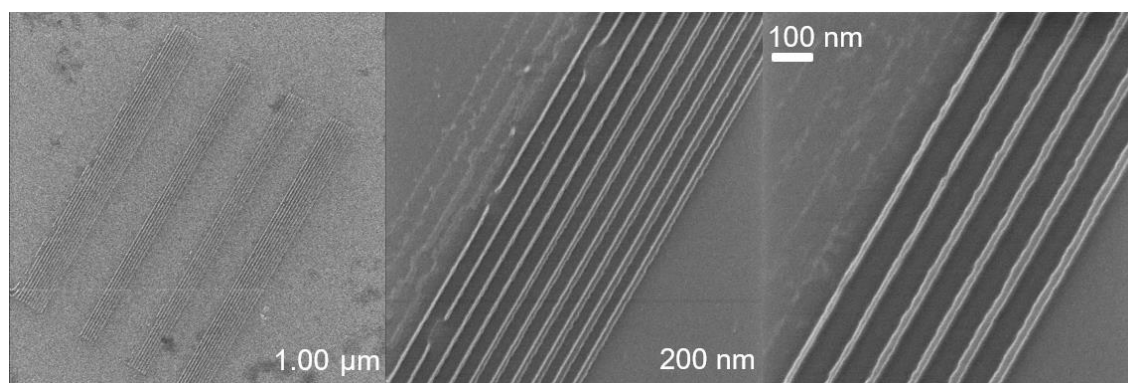


Figure 4.14 Images of Patterned lines of Keggin on Si-H.

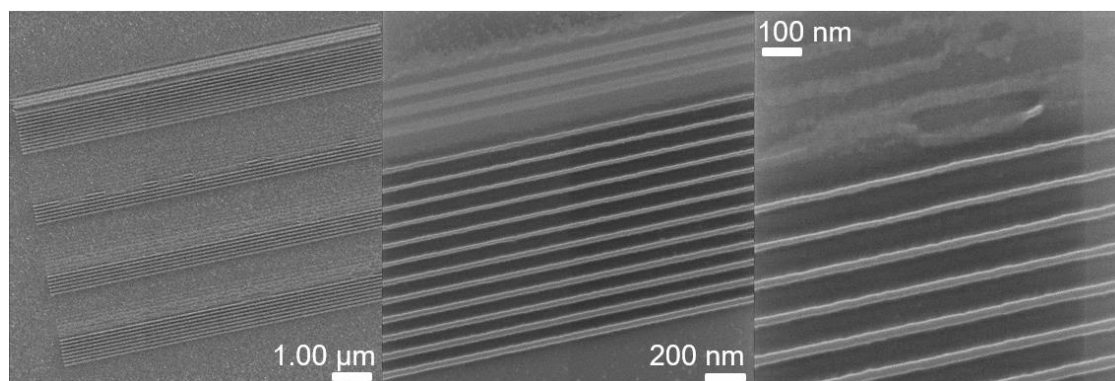


Figure 4.15 Images of Patterned lines of Keggin on SAM.

Pictures above are He-ion patterned lines using the keggin resist on Si-OH (Figure 4.13), Si-H (Figure 4.14) and ethyl undecylenate (Figure 4.15) terminated surfaces.

	Si-OH	Si-H	Si-SAM
CD(nm)	28.9	20	20
LER(nm)	13.1	8.1	6.8

Table 4.2 CD and LER for line patterns of keggin on Si-OH and Si-H and Si-SAM.

The average line widths and roughness values presented in Table 4.2 show that better patterning (i.e. thinner and smoother lines) are achieved when the surface-resist interface contains fewer chemical bonds. For Si-OH surfaces, an average line width of 29 ± 13 nm is obtained, with considerable roughness, which is worse than on Si-H and SAM terminated surfaces. For Si-H and SAM terminated surfaces, average linewidths of 20 ± 8 nm and 20.5 ± 7 nm are achieved, respectively. These results are quite similar, and demonstrate that for this resist, fewer interfacial chemical bonds are beneficial for creating thinner features with smoother edges as discussed below.¹⁷

For -OH terminated surfaces, the hydroxide group can react with the tin-oxo group forming a strong Si-O-Sn bond which may makes the crosslinking within the second layer of resist film weaker. If true, the thinner lines will not remain bound to the substrate after development. For -H terminated surfaces, the FT-IR

done by our collaborators at University of Texas Dallas showed 23% loss of hydrogen at the interface after development which contributes to an inhomogeneous interface with Si-H, Si-O and Si-O-Sn bonds. As a result, some of the line patterns may become discontinuous (as observed). For the SAM terminated surface, although it is still not sufficient to completely passivate the interface bonding between the substrate and the resist under irradiation (resulting in some residue on the surface after development), the Van de Waals forces remain sufficient to hold the resist after the hydrogen donor is consumed. We believe that this is related to the more straight and continuous line patterns we observe, which tells us that uniform weak bonding at the interface may help to preserve resist structure during the development process.

4.4.2 Implications of extra secondary electron emission from substrates

To explore the effect of substrate composition on resist patterning, we also prepared thinner Keggins films (~10 nm) with HMDS as the adhesion layer on Si, SiO₂ and Au substrates. Three types of substrates were: single-side polished n-type As-doped Si (100) wafers (resistance 0.001-0.005 ohm-cm) with native oxides, single-side polished p-type As-doped Si<100> wafers (resistance 1-10 ohm-cm) with 300 nm thermal oxides and metal coated glass slides (with 10 nm gold and a ~20 angstroms titanium adhesion layer used to bind the gold to the alumina silicate glass microscope slide). A set of line patterns with a dose of 15 $\mu\text{C}/\text{cm}^2$ were made on these three samples. The resulting AFM images are shown in Figure 4.16. Note that although the Au substrate is very rough, we are

only concerning with the resist line size, lateral position and accuracy, not substrate roughness in the vertical direction.

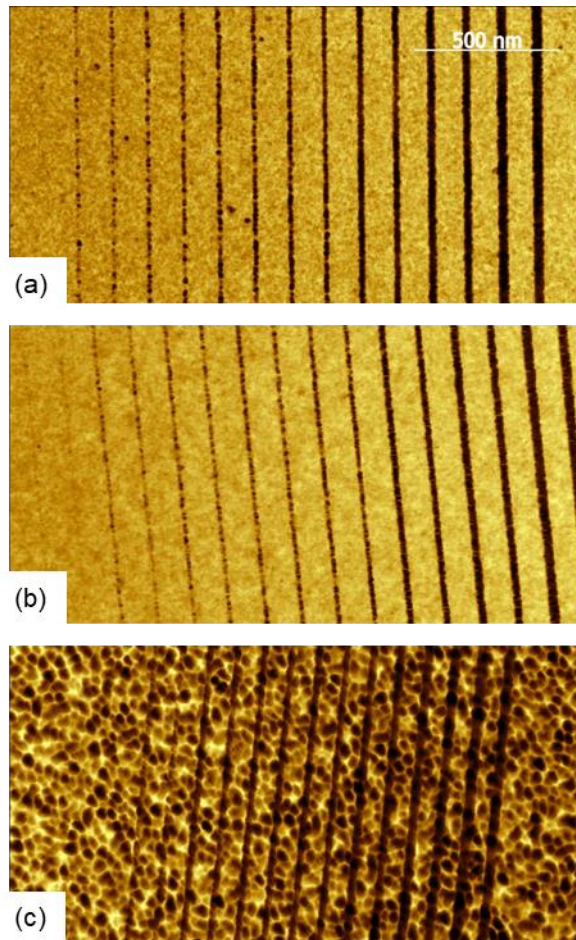


Figure 4.16 AFM invert mapping images (a), (b) and (c) of line patterns exposed to $15 \mu\text{C}/\text{cm}^2$ on Si, SiO_2 and Au coated glass substrate. The scale bar is 500 nm for all images. The nominal line widths are 1, 2, 3, 4, 5, 10, 15, and 20 nm from left to right. A pair of each lines are shown.

Two lines with 1 nm as the nominal width were almost invisible. Eight lines with 2, 3, 4, 5 nm as the nominal width were used to compare the patterning limitation at a given dose. Based on the AFM images and their line profiles, the heights of

lines of interest on Si and Au substrates are around 5 nm, comparable to wider lines that have been fully exposed. As to the lines on SiO₂ substrate, the heights of lines with 2 and 3 nm nominal width are less than 3 nm. It would seem that their condensation was not complete and it might not be able to serve as a good mask in manufacturing. In addition, the lines on Si with 2 and 3 nm nominal width are not as continuous as lines on Au were which may also introduce defects in the Si case. Only the lines on Au appear relatively straight and with higher continuity. This result indicates that the substrates can actually play an important role in manipulating patterning properties.

By treating the three substrates with the same process (applied HDMS as adhesion layer after cleaning), we can focus on particles (secondary electrons) emitted from the substrate surface which may have sufficient energy to trigger resist condensation. There are studies using Monte Carlo simulations to calculate the ion induced secondary electron yield that can escape from the surface. The simulation results using 40 keV helium ions by Huh, were quite similar to our experimental conditions.²⁴ One sees that Au has about 8 times the secondary electron yield relative to Si. This could enhance the sensitivity of the resist significantly if such secondary electrons scatter back into the resist film, transfer energy and induce chemical changes in the film.

We also explored the trajectories of helium ions and ionization in three samples using TRIM simulation software. The trajectories, shown in Figure 4.17(a) for the three substrates, indicate similar lateral dimensions and total amount of ionization in the resist films. The only difference concerns the 10-20 nm region

where gold generates more ion backscattering and therefore more energy deposition in the gold layer. The energy loss as a function of target depth is plotted in Figure 4.17(b). With similar energy loss in the photoresist, the ionization in the three substrates show huge differences. SiO_2 has even smaller ionization efficiency than the resist film itself. On the contrary, Au shows more than twice the electronic energy loss than the resist. Much more energy was deposited within the 20 nm depth range.

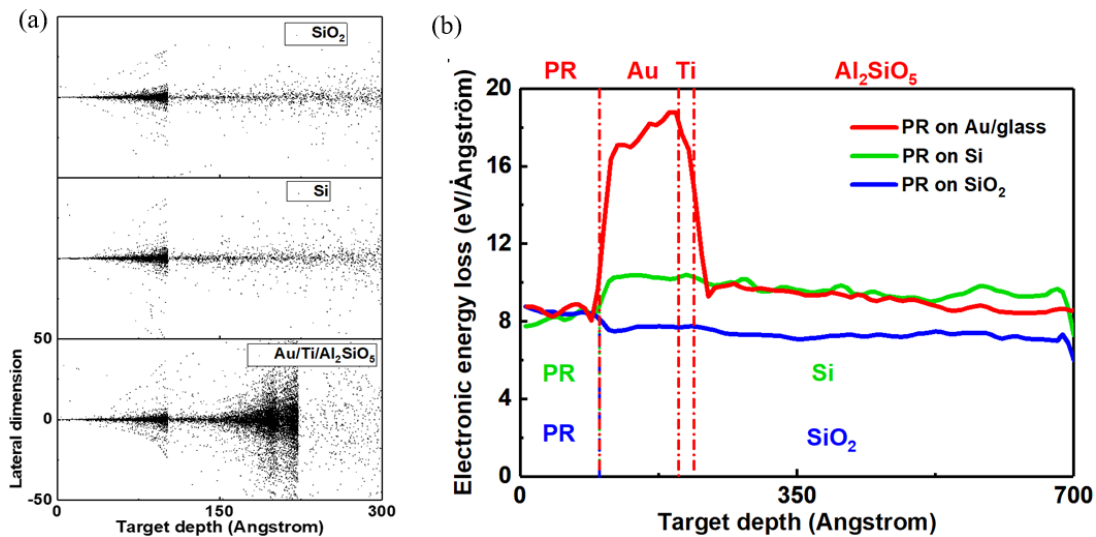


Figure 4.17 Monte Carlo simulation of (a) ion trajectories and (b) energy loss due to ionization in three samples with β - NaSn_{13} photoresist (PR) on gold coated glass, silicon and silicon oxide substrates.

Ultraviolet photoelectron spectroscopy (UPS) uses photons emitted by a helium plasma with characteristic UV emission lines (the most intense being $\text{He}1\alpha$ at 21.2 eV and $\text{He}2\alpha$ at 40.8 eV). Although having a relatively low flux, the UV source in UPS can be used to mimic the EUV exposure process (similar energy \sim 92 eV). The UPS spectrometer monitors emitted photoelectrons and as such can

help determine chemical changes in photoresist films via a measurement of the electronic valence band at the outer surface of a film.

Based on the line patterns written by HIBL, the gold substrate gives the finest and most continuous lines, less than 10 nm wide. Figure 4.18(a) shows the valence band change for 10 nm β -NaSn₁₃ resist on a gold substrate with increasing exposure time. The as-deposited β -NaSn₁₃ resist film consists of clusters with a sodium templated Sn-O-Sn core surrounded by butyl groups. Others have studied the valence band structure for Sn-O-Sn bond in crystalline SnO₂ which typically possesses three peaks ranging from 4 to 8 eV of decreasing intensities.²⁵ In our spectra, the two peaks found at high binding energy (~8 eV and ~11 eV) for the unreacted resist, are likely to correspond to Sn-O-Sn bonds, and appear shifted toward higher energies due to the organic environment surrounding these Sn-O-Sn sites. We also observed a significant shoulder at 6.3 eV which gradually increased with longer exposure as shown below, as well as a broadening of the major peak at 8 eV. We interpret these modifications of the valence band upon UV exposure as the formation of Sn-O-Sn bonds within a more metal oxide-like environment. Indeed, secondary electrons excited by incident photons can provide energy for the -OH and the organic group cleavage, forming a SnO₂-like framework to connect each cluster. We can thus use the normalized intensity of the increasing shoulder at 6.3 eV to evaluate the effective sensitivity of the resist on the three different substrates and plot the results in Figure 4.18(b). Due to the low flux in UPS, the chemical changes should be fitted into the arising curvy edge of the contrast curve in

Figure 4.3. We can observe a big difference in the increasing rate between the Au coated substrate and Si/SiO₂ substrate. When we use a linear fit to estimate the total resist reaction rate, the slope on the SiO₂, Si and Au substrates are measured to be 9.2, 9.8 and 11.7 respectively. Therefore, the Au substrate can provide almost 20% higher reaction rate which increases the effective resist sensitivity in comparison to SiO₂ and Si.

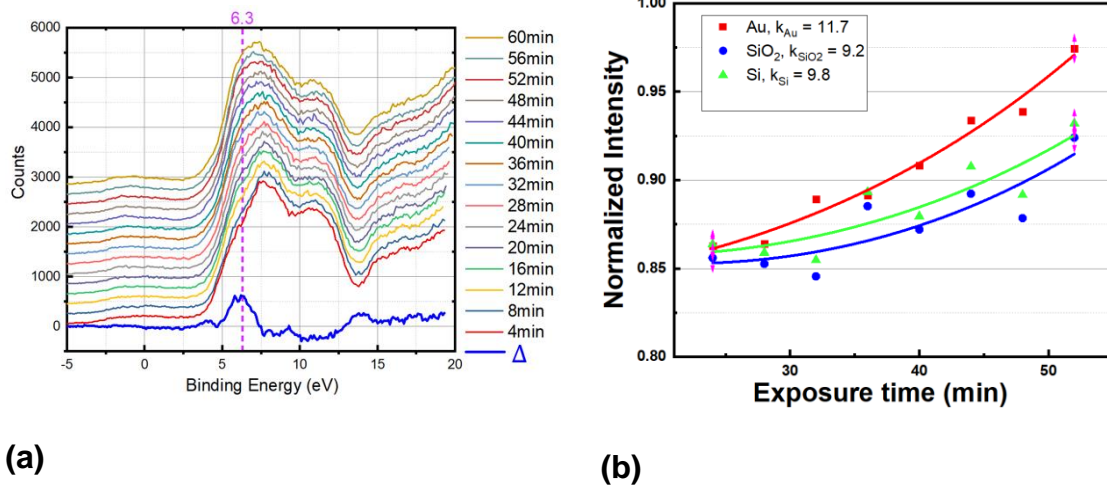


Figure 4.18 (a) Valence band spectra of β-NaSn₁₃ resist on gold substrate with increasing irradiation time. (b) Linear fitting of intensity change at 6.3 eV with β-NaSn₁₃ resist on three substrates.

In conclusion, although it is impossible to use Au as a practical substrate in devices, based on our results, it appears very worthwhile to design an underlayer with elements that have high secondary electron yield. Given the mean free path of electrons, the increased yield would mainly occur at the bottom of the resist, so it would probably add extra back exposure to the resist and help with a uniform change inside the film vertically.

Reference

1. Morton, K. J.; Nieberg, G.; Bai, S.; Chou, S. Y., Wafer-scale patterning of sub-40 nm diameter and high aspect ratio (> 50: 1) silicon pillar arrays by nanoimprint and etching. *Nanotechnology* **2008**, 19 (34), 345301.
2. Aguilar-Morales, A. I.; Alamri, S.; Lasagni, A. F., Micro-fabrication of high aspect ratio periodic structures on stainless steel by picosecond direct laser interference patterning. *Journal of Materials Processing Technology* **2018**, 252, 313-321.
3. Ozel, T.; Zhang, B. A.; Gao, R.; Day, R. W.; Lieber, C. M.; Nocera, D. G., Electrochemical deposition of conformal and functional layers on high aspect ratio silicon micro/nanowires. *Nano letters* **2017**, 17 (7), 4502-4507.
4. Moore, S. K., EUV lithography finally ready for fabs. *IEEE Spectrum* **2018**, 55 (1), 46-48.
5. Oleksak, R. P.; Ruther, R. E.; Luo, F.; Fairley, K. C.; Decker, S. R.; Stickle, W. F.; Johnson, D. W.; Garfunkel, E. L.; Herman, G. S.; Keszler, D. A., Chemical and structural investigation of high-resolution patterning with HfSOx . *ACS applied materials & interfaces* **2014**, 6 (4), 2917-2921.
6. Li, L.; Liu, X.; Pal, S.; Wang, S.; Ober, C. K.; Giannelis, E. P., Extreme ultraviolet resist materials for sub-7 nm patterning. *Chemical Society Reviews* **2017**, 46 (16), 4855-4866.
7. Luo, F.; Manichev, V.; Li, M.; Mitchson, G.; Yakshinskiy, B.; Gustafsson, T.; Johnson, D.; Garfunkel, E. In *Helium ion beam lithography (HIBL) using HfSOx as the resist*, Advances in Patterning Materials and Processes XXXIII, International Society for Optics and Photonics: 2016; p 977928.
8. Maas, D.; van Veldhoven, E.; van Langen-Suurling, A.; Alkemade, P. F.; Wuister, S.; Hoefnagels, R.; Verspaget, C.; Meessen, J.; Fliervoet, T. In *Evaluation of EUV resist performance below 20nm CD using helium ion lithography*, Extreme Ultraviolet (EUV) Lithography V, International Society for Optics and Photonics: 2014; p 90482Z.
9. Brodie, I.; Muray, J. J., *The physics of microfabrication*. Springer Science & Business Media: 2013.
10. Buitrago, E.; Fallica, R.; Fan, D.; Kulmala, T. S.; Vockenhuber, M.; Ekinci, Y., SnOx high-efficiency EUV interference lithography gratings towards the ultimate resolution in photolithography. *Microelectronic Engineering* **2016**, 155, 44-49.
11. Wiseheart, L.; Narasimhan, A.; Grzeskowiak, S.; Neisser, M.; Ocola, L. E.; Denbeaux, G.; Brainard, R. L. In *Energy deposition and charging in EUV lithography: Monte Carlo studies*, Extreme Ultraviolet (EUV) Lithography VII, International Society for Optics and Photonics: 2016; p 97762O.
12. Saha, S.; Park, D. H.; Hutchison, D. C.; Olsen, M. R.; Zakharov, L. N.; Marsh, D.; Goberna-Ferrón, S.; Frederick, R. T.; Diulus, J. T.; Kenane, N., Alkyltin Keggin Clusters Templated by Sodium. *Angewandte Chemie* **2017**, 129 (34), 10274-10278.

13. Li, M.; Manichev, V.; Yu, F.; Hutchison, D.; Nyman, M.; Gustafsson, T.; Feldman, L. C.; Garfunkel, E. L. In *Novel Sn-based photoresist for high aspect ratio patterning*, Advances in Patterning Materials and Processes XXXV, International Society for Optics and Photonics: 2018; p 105860K.
14. Saha, S.; Park, D. H.; Hutchison, D. C.; Olsen, M. R.; Zakharov, L. N.; Marsh, D.; Goberna-Ferrón, S.; Frederick, R. T.; Diulus, J. T.; Kenane, N. J. A. C., Alkyltin Keggin Clusters Templated by Sodium. **2017**, 129 (34), 10274-10278.
15. De Simone, D.; Vanelderen, P.; Vandenberghe, G., Photo Material Readiness at the Eve of EUVL HVM. *Journal of photopolymer science and technology* **2017**, 30 (5), 613-617.
16. ITRS, Metrology. **2009**.
17. Aaron Dangerfield, M. L., Danielle Hutchinson, May Nyman, Eric L. Garfunkel, Yves J. Chabal, Interfacial Evolution and Patterning Performance of a Novel Tin-OXO EUV Resist Film. **In preparation**.
18. Cattoni, A.; Mailly, D.; Dalstein, O.; Faustini, M.; Seniutinas, G.; Rösner, B.; David, C., Sub-10nm electron and helium ion beam lithography using a recently developed alumina resist. *Microelectronic Engineering* **2018**, 193, 18-22.
19. Shi, X.; Prewett, P.; Huq, E.; Bagnall, D. M.; Robinson, A. P. G.; Boden, S. A., Helium ion beam lithography on fullerene molecular resists for sub-10nm patterning. *Microelectronic Engineering* **2016**, 155, 74-78.
20. Shi, X.; Boden, S. A., Chapter 17 - Scanning helium ion beam lithography. In *Frontiers of Nanoscience*, Robinson, A.; Lawson, R., Eds. Elsevier: 2016; Vol. 11, pp 563-594.
21. Luo, F.; Manichev, V.; Li, M.; Mitchson, G.; Yakshinskiy, B.; Gustafsson, T.; Johnson, D.; Garfunkel, E. In *Helium ion beam lithography (HIBL) using HafSOx as the resist*, SPIE Advanced Lithography, SPIE: 2016; p 9.
22. Baglin, J. E. E., Ion beam nanoscale fabrication and lithography—A review. *Applied Surface Science* **2012**, 258 (9), 4103-4111.
23. Kwon, J.; Saly, M.; Halls, M. D.; Kanjolia, R. K.; Chabal, Y. J., Substrate Selectivity of (tBu-Allyl)Co(CO)₃ during Thermal Atomic Layer Deposition of Cobalt. *Chemistry of Materials* **2012**, 24 (6), 1025-1030.
24. Caillard, L.; Seitz, O.; Campbell, P. M.; Doherty, R. P.; Lamic-Humblot, A.-F.; Lacaze, E.; Chabal, Y. J.; Pluchery, O., Gold Nanoparticles on Oxide-Free Silicon–Molecule Interface for Single Electron Transport. *Langmuir* **2013**, 29 (16), 5066-5073.

Chapter 5: Josephson Junction

5.1 Introduction

Developing a fabrication process capable of producing a large number of Josephson junctions uniformly and reproducibly is crucial for using any superconductor materials, including the iron-pnictide superconductors and MgB_2 . In the case of the iron-based superconductors, studying the Josephson effect could also provide a phase-sensitive measurement to reveal the symmetry of the superconducting order parameter, a fundamental question about the pnictide superconductors still not fully understood¹. One application of the Josephson effect is in electrical metrology. A conventional Josephson Voltage Standard (JVS) has been a better alternative to a Weston cell with improved accuracy of dc voltage measurement. These devices all require series arrays consisting of thousands of identical Josephson junctions with sufficiently low parameter spreads of the junctions, i.e. critical current and normal resistance. Besides specific applications, junction series arrays are a useful tool for measuring the parameter spread of Josephson junctions. The current state of the art Nb junction technology contains over 65,000 junctions^{2, 3}, impossible to measure individually to determine the junction parameter spread. The parameter spread obtained from measuring series arrays permits a quick evaluation, which can facilitate further improvement of junction production.

To fabricate Ba122 and MgB_2 Josephson junctions with a focused He^+ ion beam, one needs to understand the irradiation effects on both the normal-state and

superconducting properties of these superconductors. This information has not been reported to date. The most relevant reports are on 200-keV proton irradiation of Ba122 films⁴ and on 2-MeV $^4\text{He}^{++}$ ion irradiation of MgB₂ films⁵. A focused ion beam was not used in these reports. In both works, although the transition temperature T_c was found to decrease upon irradiation, complete suppression of superconductivity was not reported. In this paper, we report on the modification of the normal-state resistivity and superconducting transition temperature of Co-doped Ba122 and MgB₂ thin films by 30-keV focused He⁺ ion beam irradiation. In both cases, complete suppression of T_c was observed. The systematic changes in T_c and resistivity provide guidelines for using a focused He⁺ ion beam to fabricate planar Ba122 and MgB₂ Josephson junctions.

5.2 Large area

This part of thesis is composed in part of published results⁶. Epitaxial thin films of optimally doped Ba122 were grown by pulsed laser deposition (PLD) on $5 \times 5 \text{ mm}^2$ (001) (La,Sr)(Al,Ta)O₃ (LSAT) substrates at 730°C⁷. The film thickness was 50 nm, and the films exhibited zero-resistance at $T_c \sim 19 \text{ K}$. A 20-nm protective Au layer was deposited *in-situ* on the film at 200°C. MgB₂ films were grown using hybrid physical-chemical deposition (HPCVD)⁸ on $6 \times 6 \text{ mm}^2$ (0001) SiC substrates to a thickness of 40 nm. The as-grown films were immediately transferred to a DC magnetron sputtering chamber where a bilayer of Cr/Au (5 nm/300 nm) was sputtered on the films for protection during processing. Standard UV lithography and Ar ion milling were used to pattern a 4 or 5 μm -wide bridge on the films. Subsequently, a 300 nm-thick Au film was sputter-coated on

the contact pads, and the Au (Cr/Au) on top of the Ba122 (MgB₂) bridge was removed by Ar ion milling. The entire sample was passivated with a 7 nm SiO₂ (by RF magnetron sputtering) in Ba122 and 7 nm MgO (by reactive DC magnetron sputtering of Mg target in an Ar/O₂ mixture) in MgB₂ (see table I).

Table 5.1 Characteristics of the Co-doped Ba122 and MgB₂ thin films used in this study.

	Substrate	Growth technique	Critical temperature	Film thickness	Passivation layer	Passivation thickness
Co-doped Ba122	LSAT (001)	PLD	~ 19 K	50 nm	SiO ₂	7 nm
MgB ₂	SiC (0001)	HPCVD	~ 39 K	40 nm	MgO	7 nm

Focused He⁺ ion beam irradiation was conducted at room temperature using a Zeiss Orion Plus helium ion microscope with a 30-keV He⁺ beam with a 0.5 nm spot size. The beam is perpendicular to the plane of the film; thus the possibility of channeling through the crystal cannot be excluded. Transport of ions in matter (TRIM) computer codes⁹ were used to simulate the interactions of the He⁺ ions in the film/substrate geometry. Figure 5.1(a) shows the resulting distribution of 30-keV He⁺ ion range in a 7 nm SiO₂/50 nm Ba122/LSAT substrate sample. The thickness of the Ba122 film was chosen to be much smaller than the range of the He⁺ ions, which therefore completely penetrate the film into the substrate (The

same consideration was taken into account in choosing the thickness of MgB_2 film).

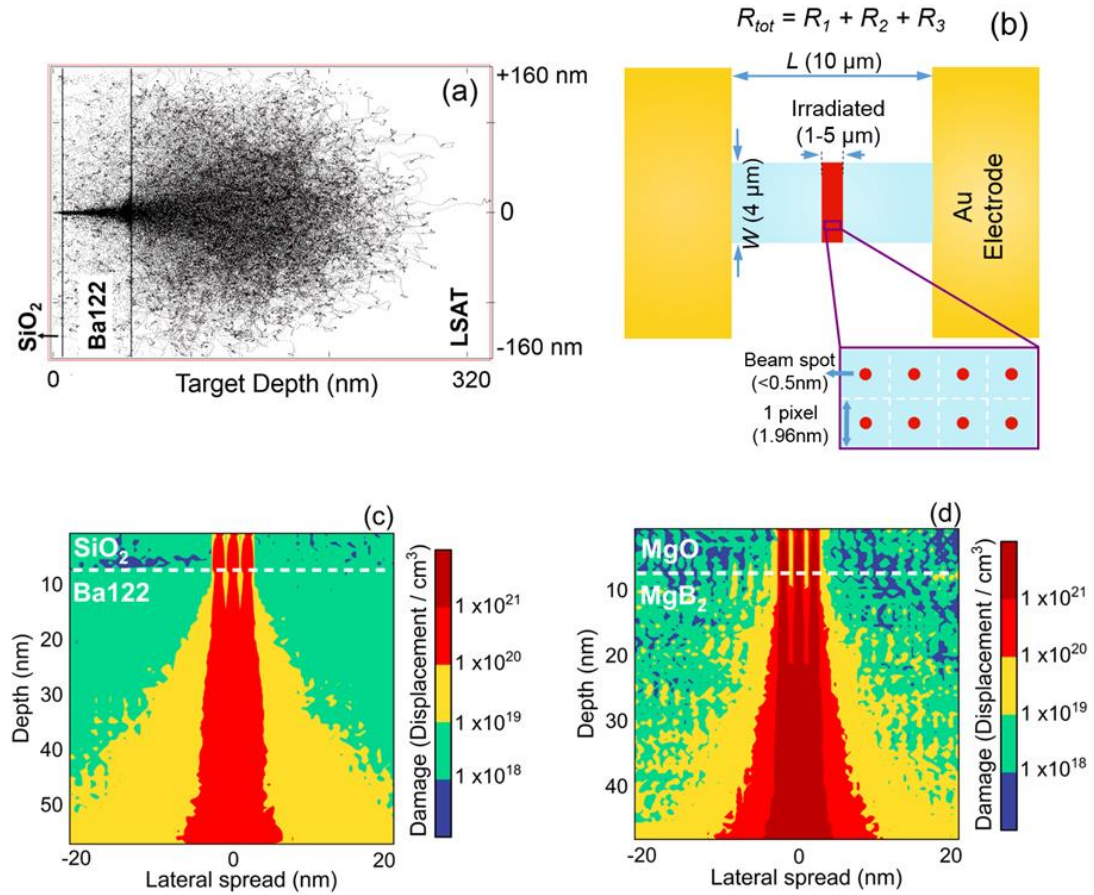


Figure 5.1 (a) TRIM simulation of the range of 30-keV He^+ ions in a 7 nm SiO_2 /50 nm Ba122 /LSAT substrate sample. (b) Schematic of the sample with a 4 μm \times 10 μm bridge. The blue area represents the pristine film. Figure 1. The focused He^+ ion beam was rastered over the red rectangle. The blowup of the irradiated area shows the raster pattern of the focused He^+ ion beam. The white dashed lines are guide to eye, showing a pixel size of 1.96 nm \times 1.96 nm at the 100 nm FOV (c) TRIM simulation of the damage density profile for three adjacent single tracks of He^+ in the SiO_2 / Ba122 sample at $5 \times 10^{14}/\text{cm}^2$ (d) TRIM simulation of the

damage density profile for three adjacent single tracks of He^+ in the MgO/MgB_2 sample at $8 \times 10^{15}/\text{cm}^2$.

For the purpose of measuring the irradiation effects on T_c and normal-state resistance, we rastered the He beam to irradiate multiple tracks over a length of 1 μm or 5 μm in a 10 μm -long bridge. The geometry of the bridge and the irradiated area are illustrated in Figure 5.1 (b). The blowup of an irradiated area shows that, at a 100- μm field of view (FOV), the pixel size is 1.96 nm \times 1.96 nm, larger than the beam spot. He^+ ion beam moved from the center of one pixel to the next, delivering the needed dose at each center spot. Figure 5.1(c) and 1(d) shows the simulated damage profile of three adjacent tracks caused by the He^+ ion irradiation in three beam spots, with 1.96 nm pixel spacing, penetrating into the $\text{SiO}_2/\text{Ba122}$ and MgO/MgB_2 film, respectively. Although the lateral spreading of the damage regions quickly exceeds the beam spot size after the ions enter the film, overlapping over the entire irradiated area, the damage is not laterally uniform in the top part of the samples.

To characterize the damages caused by the helium ion beam in the MgB_2 thin film, transmission electron microscope (TEM) measurement was performed using a JEOL JEM2100 microscope operated at 200 kV. The sample was a 10 nm MgO passivation layer/25 nm-thick MgB_2 film with a patterned 4 μm \times 10 μm bridge, across which 4 single-pixel-width lines were irradiated with the focused helium ion beam at 4 different doses - 8×10^{15} , 2×10^{16} , 6×10^{16} , and 5×10^{17} / cm^2 . To avoid cross-line dosing between adjacent lines ¹⁰ the lines were

separated by 1 μm distance. The cross-sectional TEM sample was prepared using a Dual Beam Focused Ion Beam - SEM (FEI Strata DB235).

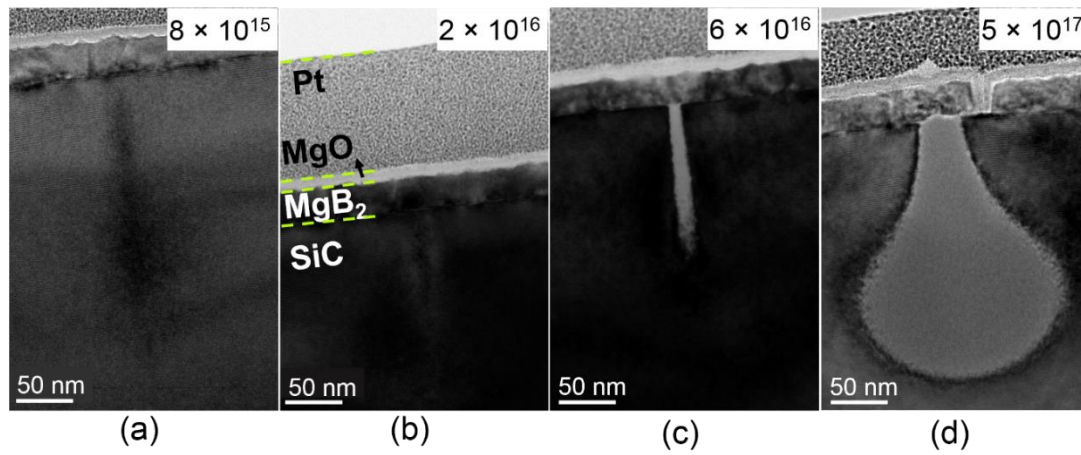


Figure 5.2 Complete series of TEM BF micrographs of thin film of (10 nm MgO/25 nm MgB₂/on SiC substrate) irradiated by a 30 keV He⁺ ion beam with increasing doses. The dose values on each micrograph are in ions/cm².

Figure 5.2(a-d) show cross-sectional TEM bright field (BF) images of irradiated regions of four beam spots with the doses of 8×10^{15} , 2×10^{16} , 6×10^{16} , and 5×10^{17} /cm², respectively. While the damage is not visible in the MgB₂ film, it can be more easily observed in the SiC substrate. At the two lowest doses, different contrasts in the irradiated regions in the substrate can be seen [see Figure 5.2 (a) and 2(b)]. At the dose of 6×10^{16} /cm², an amorphized region in the substrate is clearly visible [see Figure 5.2 (c)]. For the dose of 5×10^{17} /cm², the amorphous region in the substrate grows through the depth of the sample as well as laterally, as the damage produced by the periphery of the ion beam also reaches the damage threshold to be visible [see Figure 5.2(d)]. From the Hi-Resolution TEM (HRTEM) images in Figure 5.3, we find that the diameter of the amorphous

region at the MgB_2/SiC interface is ~ 10 nm for $6 \times 10^{16}/\text{cm}^2$ and ~ 30 nm for $5 \times 10^{17}/\text{cm}^2$.

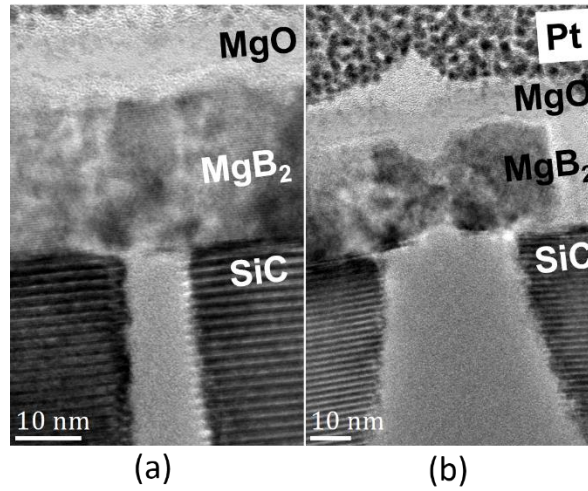


Figure 5.3 High resolution TEM micrographs of the thin film of (10 nm MgO/25 nm MgB_2 /on SiC substrate) irradiated with a helium ion dose of (a) $6 \times 10^{16}/\text{cm}^2$, (b) $5 \times 10^{17}/\text{cm}^2$.

The amorphized region in the substrate observed in figure 2(d) is qualitatively consistent with the TRIM simulation. A quantitative one-to-one correspondence to the region where superconductivity is completely suppressed by ion irradiation is difficult to extract from these data, as the damage may be annealed during the electron microscope measurement. We have observed the annealing effect in the low-dose samples. Nevertheless, we can conclude from the results that the region damaged by the He ion irradiation spreads much wider than the focused beam size when the ions travel deep into the film. The TRIM results in figures 1(c) and 1(d) provide a good guideline when we consider the irradiation effects on transport and superconducting properties of the superconductor films.

We show that superconductivity is suppressed and the normal-state resistivity is increased upon focused He^+ ion beam irradiation. The critical dose for the complete suppression of superconductivity is $\sim 5 \times 10^{14}/\text{cm}^2$ for Ba122 and $\sim 8 \times 10^{15}/\text{cm}^2$ for MgB_2 corresponding to large vacancy concentrations in the films. It should be noted that the irradiation-induced disorder spread out beyond the focused ion spot size in the depth of the film as shown in figure 1(c,d). Thus, in fabricating a Josephson junction with a focused He^+ ion beam, one should minimize the thickness of the film so that the damaged area remains narrow enough for the interference of the order parameter to take place. Nonetheless, the expansion assures that no part of the film remains unirradiated in between single tracks. Also, the specific values of the irradiation doses here are for the multiple-track irradiation and expected to differ from those in the single-track irradiation. Nevertheless, the results are useful to guide the development of a focused He^+ ion beam technology for fabricating iron pnictide and MgB_2 planar Josephson junctions.

5.3 Array junction

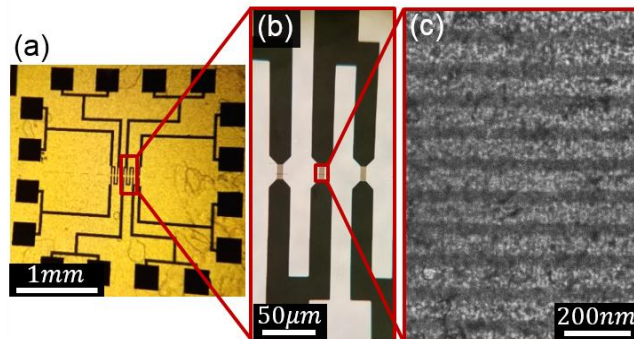


Figure 5.4 (a) Optical image of the array pattern. Large bonding pads attached to a centered meandering micro-strips. (b) Three branches of the meander are

enlarged. Dark color lines are Au covered MgB₂. The tapered down bridges are SiO₂ covered MgB₂. (c) Zoomed view of single tracks of He⁺ irradiation at 100 nm inter-spacing on a 5 x 15 μm^2 bridge imaged in HIM.

This part of thesis is composed in part of published results¹¹. Junction and series junction arrays were fabricated using 25 nm thick MgB₂ thin films grown by hybrid physical-chemical deposition (HPCVD) on SiC substrates⁸. To protect the surface of the MgB₂ thin film from degradation during fabrication, a bilayer of Cr/Au (5 nm/20 nm) was deposited by DC magnetron sputtering on top of the film. 15 $\mu\text{m} \times 5 \mu\text{m}$ bridges and electrical bonding pads connecting to them were patterned by standard UV lithography and argon ion milling (see Figure 5.4). A second lithography and ion milling were carried out to remove the Cr/Au bilayer on top of the bridges. A 4 nm SiO₂ thin film was then deposited on the entire sample by RF magnetron sputtering for protection against moisture. The sample was then loaded *ex-situ* into the chamber of a Zeiss Orion plus helium ion microscope. A single pixel line of 30 keV beam (the highest energy commonly available with the system with nominal beam diameter < 0.5 nm and pitch = 1 nm) was used to directly write Josephson junctions into the plane of the thin film at room temperature. TRIM (Transport of ions in matter) software program¹² was used to simulate the He ion beam interaction with the target material. The total thickness of the MgB₂ + SiO₂ protection layer (25+4 nm) was chosen to be substantially smaller than the projected range (PR) of the 30 keV He⁺ ions in the target (> 150 nm). In Figure 5.5(a), damage density (displacement per volume, color scale) is shown within the sample suggesting that at displacement level ~ 1

$\times 10^{20} / \text{cm}^3$, the width of the damaged region, is ~ 7.5 nm at the MgB_2/SiC interface and ~ 1 nm at $\text{SiO}_2/\text{MgB}_2$ interface. This lateral spread allows for observing the Josephson effect in the MgB_2 planar junctions. Figure 5.5 (b) shows the damage profile for top and bottom interfaces of MgB_2 film, indicating that the lateral spread of the damage characterized by the full width at half maximum (FWHM) is about doubled by the time ions reach the bottom of the film. Single Josephson junctions and 9 series arrays with various number (10, 30, 50, 60) of JJs were written on different bridges using single pixel lines of He^+ beam with a dose of $2.7 \times 10^{16} \text{ ions/cm}^2$ and 100 nm inter-junction spacing (Figure 5.4). Here we discuss the results on 50 and 60 JJ arrays representing the typical of the whole series. We also present the result of a single junction for comparison purposes.

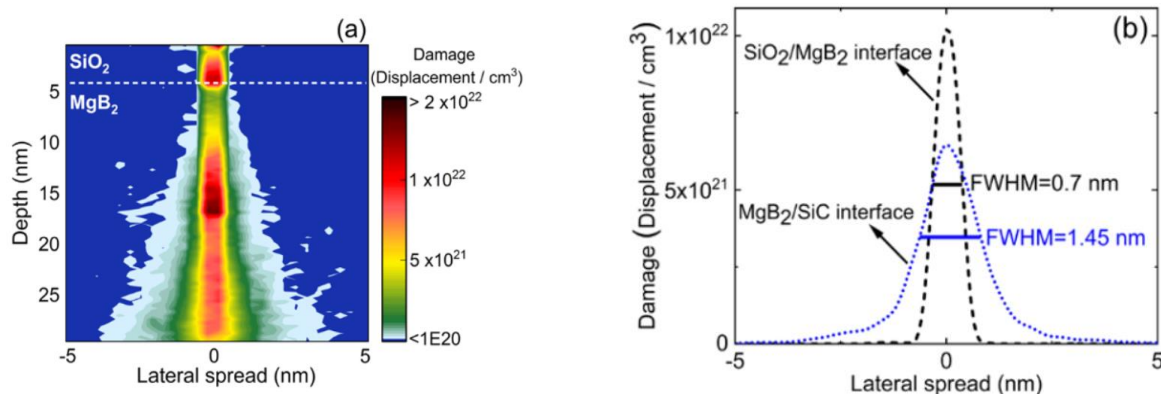


Figure 5.5(a) TRIM simulation of damage density in $\text{SiO}_2/\text{MgB}_2$ (4+25nm) film deposited on SiC substrate when irradiated with $2.7 \times 10^{16} / \text{cm}^2$ He ions. (b) Black dashed line represents damage profile at $\text{SiO}_2/\text{MgB}_2$ interface with the area under the curve $\sim 7.5 \times 10^{22}$. Blue dotted line represents damage profile at MgB_2/SiC interface with the area under the curve $\sim 1.2 \times 10^{23}$.

Uniformity of junction parameters within the arrays was sufficient for achieving phase-lock into an applied microwave signal and flat giant Shapiro steps were observed. The spread in critical current of a 60-Josephson junction array was estimated to be less than 3.5%, indicating excellent lateral homogeneity of the barrier. It was significantly better than reported in MgB₂ junctions fabricated by other techniques. The normal resistance of the array scaled proportionally to the number of junctions in the array. These results demonstrate the potential of the focused He⁺ ion beam irradiation technique in MgB₂ Josephson multi-junction circuit applications such as quantum voltage standards.

Reference

1. Hirschfeld, P.; Korshunov, M.; Mazin, I., Gap symmetry and structure of Fe-based superconductors. *Reports on Progress in Physics* **2011**, 74 (12), 124508.
2. Nagasawa, S.; Hinode, K.; Satoh, T.; Hidaka, M.; Akaike, H.; Fujimaki, A.; Yoshikawa, N.; Takagi, K.; Takagi, N., Nb 9-layer fabrication process for superconducting large-scale SFQ circuits and its process evaluation. *IEICE Transactions on Electronics* **2014**, 97 (3), 132-140.
3. Herr, Q. P.; Osborne, J.; Stoutimore, M. J.; Hearne, H.; Selig, R.; Vogel, J.; Min, E.; Talanov, V. V.; Herr, A. Y., Reproducible operating margins on a 72 800-device digital superconducting chip. *Superconductor Science and Technology* **2015**, 28 (12), 124003.
4. Schilling, M. B.; Baumgartner, A.; Gorshunov, B.; Zhukova, E.; Dravin, V.; Mitsen, K.; Efremov, D.; Dolgov, O.; Iida, K.; Dressel, M., Tracing the s_{\pm} symmetry in iron pnictides by controlled disorder. *Physical Review B* **2016**, 93 (17), 174515.
5. Gandikota, R.; Singh, R.; Kim, J.; Wilkens, B.; Newman, N.; Rowell, J.; Pogrebnyakov, A.; Xi, X.; Redwing, J.; Xu, S., Effect of damage by 2 MeV He ions on the normal and superconducting properties of magnesium diboride. *Applied Physics Letters* **2005**, 86 (1), 012508.
6. Kasaei, L.; Manichev, V.; Li, M.; Feldman, L. C.; Gustafsson, T.; Collantes, Y.; Hellstrom, E. E.; Demir, M.; Acharya, N.; Bhattarai, P., Normal-state and superconducting properties of co-doped BaFe₂As₂ and MgB₂ thin films after focused helium ion beam irradiation. *Superconductor Science and Technology* **2019**.
7. Lei, Q.; Golalikhani, M.; Yang, D.; Withanage, W.; Rafti, A.; Qiu, J.; Hambe, M.; Bauer, E.; Ronning, F.; Jia, Q., Structural and transport properties of epitaxial Ba(Fe_{1-x}Co_x)₂As₂ thin films on various substrates. *Superconductor Science and Technology* **2014**, 27 (11), 115010.
8. Xi, X. X., MgB₂ thin films. *Superconductor Science and Technology* **2009**, 22 (4), 043001.
9. Ziegler, J. F.; Biersack, J.; Littmark, U., The stopping and range of ions in matter, Vol. 1. 1, *Pergamon Press, New York* **1985**.
10. Kieslich, A.; Reithmaier, J.; Forchel, A., Minimum feature sizes and ion beam profile for a focused ion beam system with post - objective lens retarding and acceleration mode. *Journal of Vacuum Science & Technology B: Microelectronics and Nanometer Structures Processing, Measurement, and Phenomena* **1994**, 12 (6), 3518-3522.
11. Kasaei, L.; Melbourne, T.; Li, M.; Manichev, V.; Qin, F.; Hijazi, H.; Feldman, L. C.; Gustafsson, T.; Davidson, B. A.; Xi, X., Reduced Critical Current Spread in Planar MgB₂ Josephson Junction Array Made by Focused Helium Ion Beam. *IEEE Transactions on Applied Superconductivity* **2019**, 29 (5), 1-6.

12. Ziegler, J. F.; Ziegler, M. D.; Biersack, J. P., *SRIM: the stopping and range of ions in matter*. Cadence Design Systems: 2008.

Chapter 6: Conclusion

This dissertation discussed the strategy to prescreen EUV photoresists as well as the advantage of using focused helium ion beam for the nanofabrication. Multiple surface/interface techniques were used to provide comprehensive analysis of thin film physical and chemical properties such as Atomic Force Microscope (AFM), X-ray Photoelectron Spectroscopy (XPS), Ultraviolet Photoelectron spectroscopy (UPS), Rutherford Backscattering Spectroscopy (RBS) and Helium Ion Microscope (HIM). The irradiation mechanism study provides better understanding of possible active species that could contribute to solubility changes of novel metal-containing resists. It provides a direction of developing this resist platform and estimating patterning performance accordingly. Sub-10 nm resolution with only 2.1 nm line edge roughness line patterns were achieved with focused helium ion beam single exposure. The investigation of interface bondings and substrates effect gives a hint about how to manipulate resist film stacking structures to achieve better RLS performance. Focused helium ion beam was further used to fabrication novel planar Josephson Junctions and achieve large array devices with significantly better consistency than other nanofabrication techniques. Ion displacement events were simulated to explain the correlation between ion doses and junction creation.